2020

A State Estimation Framework for Fatigue Monitoring and Prognosis of Minimally Instrumented Structural and Biomechanical Systems

Benjamin LeBlanc
University of Vermont

A STATE ESTIMATION FRAMEWORK FOR FATIGUE MONITORING AND
PROGNOSIS OF MINIMALLY INSTRUMENTED STRUCTURAL AND
BIOMECHANICAL SYSTEMS

A Dissertation Presented

by

Benjamin P LeBlanc

to

The Faculty of the Graduate College

of

The University of Vermont

In Partial Fulfillment of the Requirements
for the Degree of Doctor of Philosophy
Specializing in Civil & Environmental Engineering

May, 2020

Defense Date: February 21st, 2020
Dissertation Examination Committee:

Eric M. Hernandez, Ph.D., Advisor
Chris Danforth, Ph.D., Chairperson
Ting Tan, Ph.D.
Ehsan Ghazanfari, Ph.D.
Niccolo Fiorentino, Ph.D.
Cynthia J. Forehand, Ph.D., Dean of Graduate College

ABSTRACT

Fatigue damage is the continuous degradation of a material, primarily due to the formation of microcracks and resulting from the repeated application of stress cycles. Traditionally a fatigue analysis was performed during the structural design stage of a machine or structure; however, more recently there has been increased interest in the monitoring and prognosis of fatigue damage in existing and operating structures. In monitoring, the structure already exists and its mechanical properties can be estimated by processing sensor measurements and non-destructive testing. The traditional approach to fatigue monitoring is to carry out a visual inspection, find macroscopic cracks and then predict their growth. This was often carried out by finding changes in dynamic properties of the system, i.e. changes in modal frequencies, mode shapes, and modal damping. Yet in many cases, by the time the cracks grow to a point where they are detectable, the load bearing capacity of the structure has been greatly reduced. Therefore, a preferable approach is to track fatigue damage on the whole structure prior to the appearance of macroscopic cracks. This would allow for higher levels of reliability, larger lead times and reduced risk. Although no exact figures are available, it is estimated that upwards of 50% of mechanical failures in metallic structures can be attributed to fatigue. Structural health monitoring has been extensively studied for structural systems but hasn't been applied to biomechanical systems where biomechanical failure is consistent with the process of mechanical fatigue.

The objective of this dissertation is to show that state estimation algorithms, i.e. the Kalman filter, can be successfully formulated to estimate fatigue damage in near-real time for structural and biomechanical systems. The Kalman filter combines dynamic response measurements at minimal spatial locations with a structural model to estimate the response of the dynamical system at all model degrees-of-freedom. The estimates of the dynamic response of the instrumented structural systems are subsequently used for fatigue damage diagnosis and prognosis in combination with an empirical S-N curve. By quantifying the uncertainty in both the state estimate and S-N curve, the fatigue damage index becomes bounded based on a user-defined allowable probability of failure.

The main contributions of this dissertation are summarized as follows: i) Development of a fatigue monitoring framework for structural and biomechanical systems; ii) Experimental validation of service life fatigue monitoring in near-real time for statically determinant structures; iii) Uncertainty quantification and propagation of system response and fatigue damage estimates using Kalman filters.

CITATIONS

Material from this dissertation has been published in the following form:

- LeBlanc, B. and Hernandez, EM.. (2017). Fatigue usage monitoring in wind turbines using sparse vibration measurements. Structural Health Monitoring 2017.

Material from this dissertation has been submitted for publication to the *Journal of Structural Control and Health Monitoring* on November 2019 in the following form:

- LeBlanc, B. and Hernandez, EM.. (2019). Fatigue life prognosis using minimum global response measurements: experimental validation.

Material from this dissertation has been submitted for publication to the *Journal of Biomechanics* on December 2019 in the following form:

- LeBlanc, B. Hernandez, EM. McGinnis, RS. Gurchiek, RD.. (2019). Estimating ground reaction force within a mechanical fatigue framework: an application for high mileage runners.

DEDICATION

To my parents,

Phil & Cathy LeBlanc

TABLE OF CONTENTS

LIST OF FIGURES

LIST OF TABLES

CHAPTER 1

INTRODUCTION

1.1 BACKGROUND AND MOTIVATION

Fatigue is the degradation of a structure due to the repeated application of cyclic stresses, even if the applied stress is below the material's yield strength. It has been estimated that 50% of mechanical failures can be attributed in one way or another to fatigue [Stephens et al.; 2000]. Fatigue failures are not only confined to structural systems but also biological systems, such as with stress fractures and overuse injuries in runners. Studies have shown that eight out of ten runners will get injured each year [van Gent et al.; 2007]. Although fatigue is hard to predict, monitoring can help reduce uncertainty.

A major challenge for the civil engineering community is the aging infrastructure of the United States. Engineered systems will gradually deteriorate due to operational stresses if they are not properly managed and maintained. Therefore it is essential to monitor the performance and estimate the remaining useful life of current civil infrastructure. Traditionally, visual inspections were performed by trained inspectors

to assess the current condition of the structure. However, this process has been proven inefficient due to the subjective nature of inspections that often fail to quantify unseen damage within the structure or those located in hard to reach places [Inaudi & Deblois; 2009]. It has been estimated that upgrading the existing fatigue critical infrastructure would cost $1.6 trillion in part due to a significant portion of the infrastructure exceeding its intended service life [USDOH; 2010].

Structural health monitoring (SHM) has been extensively studied for the past four decades in order to identify the extent of damage in civil, mechanical and aerospace engineered structures. The main focus of this interdisciplinary research has been to develop and implement sensing technologies and data processing methods in order to assess the condition and/or find damage in structural systems. This could include civil infrastructure, aircraft, wind turbines, mechanical machines, and biomechanical systems. In this context damage is defined as a change in material and/or geometric properties that adversely affect the performance of the system [Farrar & Worden; 2007]. Systems are typically instrumented with an array of sensors that capture the dynamic global response during operation. The SHM framework then assesses the current state of the system by extracting damage sensitive features from the observed dynamic response measurements.

Throughout the lifetime of a system, the operational environment will naturally age and degrade the structure. Continuous monitoring during the structures lifetime allows for increased knowledge of the state of the system during this degradation process ensuring that the system is able to perform its intended function. When an extreme event occurs, for example an earthquake, SHM can be used to quickly assess the damage and potential hazard in near real time prior to or in combination

with a visual inspection. Therefore structural damage may be due to gradual wear or discrete events which are classified by high-cycle or low-cycle fatigue [Inman et al.; 2005]. High-cycle fatigue is characterized by high frequency low amplitude stress cycles, such as with ground reaction forces while running or bridges subject to traffic loads. Low-cycle fatigue is characterized by low frequency high amplitude stress cycles, such as with earthquake ground motions that tend to nonlinear geometric deformations.

The concept of monitoring the health of a structure is not a new idea, as early as the 19th century the term fatigue had been coined. After the Versailles train crash in 1842, tapping of train wheels became common practice to qualitatively determine fatigue damage [Schutz; 1996]. In the ensuing decades structural monitoring became focused on response systems to extreme events. Only recently has there been a shift to long-term SHM especially with catastrophic failures such as the I-35W Bridge collapse in Minneapolis, MN the need for continuous fatigue monitoring had become apparent [Hao; 2010].

Figure 1.1: Fatigue failures (a) I-35 bridge collapse, (b) a wind turbine collapse

Vibration based monitoring is a passive method that uses a network of sensors to measure the dynamic response of a system. The resolution of this method is based on the number and layout of the sensor array on the structure. Sensors can include accelerometers, strain gages, fiber optic sensors, etc. The foundation for vibration-based damage detection is that small changes in the physical properties, (mass, damping, and stiffness) can cause measurable changes in the dynamic properties of the system, for example changes in natural frequencies, modal damping, and mode shapes [Doebling et al.; 1998]. Oftentimes these methods provide a general overview of damage within the structure yet require knowledge of potential damage locations.

This work is motivated in part by the need to quantify damage and its uncertainty in near real time when no physical damage is apparent. At the onset of a crack there is a localized decrease in the stiffness of the structure that will create changes in the dynamic response measurements. Yet, oftentimes when a crack coalesces and propagates the change in dynamic properties is indiscernible until the crack is visible or grows to a critical size. By the time the change is seen, the strength of the structure has already been greatly reduced. Therefore global vibration measurements should be used to reconstruct the stress fields throughout the entire structure and monitor the fatigue damage from an early stage prior to macroscopic cracks appearing to achieve near-real time monitoring and prognosis of fatigue damage.

1.2 RESEARCH OBJECTIVES

The objective of this work is to show that optimal linear filtering can be applied to structures subject to non-Gaussian excitation for fatigue monitoring in near-real
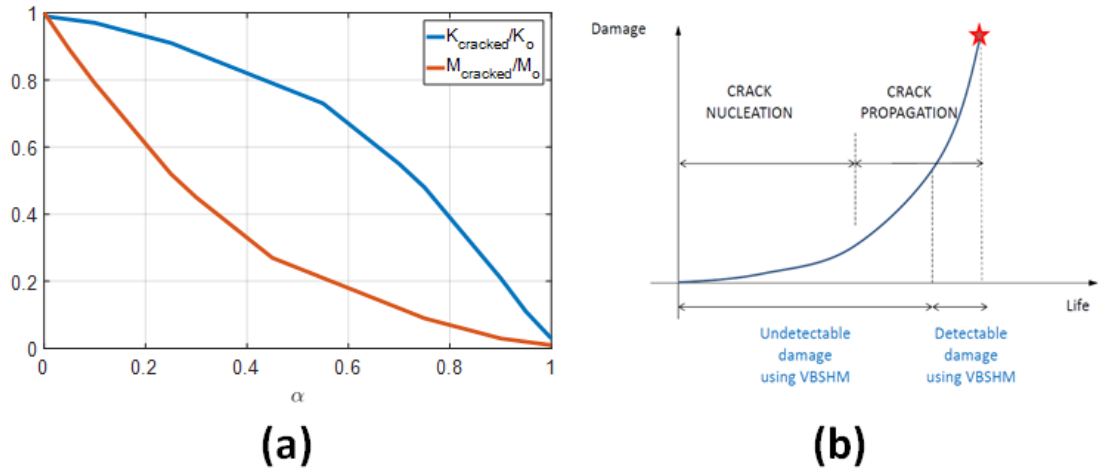
Figure 1.2: Dynamic properties vs. Remaining Strength

time. The Kalman filter combines structural models with limited global measurements to obtain the probabilistic estimate of the response throughout the structure. A mechanistic approach is explored to quantify structural fatigue damage during the serviceable life of structures subject to non-Gaussian excitation. For this purpose the estimate of the response and its uncertainty is fused with probabilistic damage models, i.e probabilistic S-N curves, for fatigue monitoring applications to provide a generalized framework for damage accumulation.

In this dissertation the Kalman filter for linear state estimation is verified and validated using simulated and experimental results for damage accumulation. For this purpose, the estimated states are compared to corresponding simulated or measured quantities, and the accuracy and efficiency of the results are quantified to generate a fatigue monitoring framework. The framework is then considered for three uncorrelated systems subject to non-Gaussian processes.

1.3 Dissertation Contributions

The main contributions of this dissertation are the following:

- *Development of a state estimation mechanistic fatigue usage framework.* A framework for fatigue usage monitoring and prognosis is developed. The purpose of this dissertation is to determine if it is possible to estimate fatigue damage in near real time for structural systems with unknown excitation within the same structural health monitoring framework. Then to determine the accuracy of the estimates of the dynamic response of a structural system when fundamental conditions are relaxed, i.e the excitation is a Gaussian process. Four fundamental steps are necessary in order to carry out fatigue monitoring: (1) statistical knowledge of the loads, (2) detailed stress analysis (3) statistical model for the variation of material properties and (4) damage accumulation framework.

- *Uncertainty quantification and propagation for fatigue usage estimates.* The accumulation of fatigue damage is a random process. Typically the fatigue material properties can be expressed as a random variable while the applied loading on the structure is a stochastic process. Uncertainty is introduced into the damage index from the the estimated stresses determined by the state estimation algorithm and the empirical fatigue material properties. The objective of this dissertation is to characterize the variation in the damage index in order to quantify confidence in the fatigue state at any time for any structure in order to determine a generalized stopping criteria.

- *Experimental validation of developed fatigue usage framework.* Application in a small-scale experiment: A Kalman filter is used to estimate local stress fields based on global acceleration measurements. From the estimated stress, the evolution of mechanical fatigue can be monitored by using a rainflow cycle counting algorithm and an empirical S-N curve to estimate a damage index and its uncertainty using Miner's rule. The methodology is tested using aluminum cantilever beams with a reduced cross section near the base support to facilitate crack initialization and propagation. The damage index is tracked in near-real time and a stopping criteria is determined. To the best knowledge of the author this is the first experiment that tracks fatigue damage and its uncertainty using global measurements until failure.

1.4 Dissertation Overview

The dissertation is organized as follows:

- *Chapter 2: Fundamentals.* An introduction to the general theory necessary to understand the content in the remainder of the dissertation. This chapter covers the fundamental principles for system theory including state space representation, fatigue theory and structural health monitoring with a focus on fatigue usage to generate a fatigue monitoring framework for structural and biomechanical systems. Provided is a literature review of how researchers have approached the fatigue monitoring problem, dating back to the 19th century, and how knowledge has progressed for fatigue usage monitoring in various systems.

- *Chapter 3: Fatigue usage monitoring in 5MW simulated wind turbine using sparse vibration measurements: comparative study.* In this chapter a comparative study for stress estimation for a simulated wind turbine is provided. With the high infrastructure costs of wind turbine systems, it is necessary to have a SHM system to track fatigue throughout the serviceable life to prevent structural failures. By optimally placing sensors global dynamic response can be estimated which can then be used in a fatigue damage monitoring framework. The global dynamic response is estimated by a model-based-observer, a Kalman filter, and a modal interpolation method. The comparison is carried out on the National Renewable Energy Laboratory's (NREL) 5MW reference turbine subjected to turbulent wind within NREL's high-fidelity FAST software for 20 simulated test cases.

- *Chapter 4: Fatigue life prognosis using minimum global response measurements: experimental validation.* In this chapter a probabilistic methodology for fatigue prognosis using global response measurements is provided and experimentally validated. A Kalman filter is employed to estimate local stress fields based on global acceleration measurements. The time history of the estimated stress fields are combined with fatigue damage models to compute the estimated fatigue damage and its uncertainty in near-real time. Aluminum cantilever beams with a reduced cross-section near the base support to facilitate crack initialization are excited with a sequence of base motions. Each beam was tested until failure while the algorithm simultaneously predicted the extent of damage and its uncertainty in near real time.

- *Chapter 5: Estimating ground reaction force within a mechanical fatigue frame-*

work: an application for high mileage runners. In this chapter the fundamental framework to estimate ground reaction forces in runners using minimal global response measurements is provided. This research bridges the disciplines of system theory and biomechanics by framing the problem within a mechanical fatigue framework. By modeling a human as a structure the previously derived probabilistic methodology for fatigue prognosis can be applied to biological structures. 14 participants ran on an instrumented treadmill at various user-defined speeds with an accelerometer placed at the sacrum. A dual Kalman filter is formulated to estimate the unknown excitation, while an unscented Kalman filter estimates the augmented state vector using the estimated excitation in order to determine the corresponding ground reaction force at each step. From the estimated ground reaction force, the evolution of mechanical fatigue can be monitored.

- *Chapter 6: Conclusions and future work.* Provides an overview of the breadth of research covered in the dissertation and possible areas for further research.

REFERENCES

[Doebling et al.; 1998] Doebling, S. Farrar, C. Prime, MB. (1998). A summary review of vibration-based damage identification methods. *Shock and Vibration Digest.* 30(2):91-105.

[Farrar & Worden; 2007] Farrar, CR. Worden, K. (2007). An introduction to structural health monitoring. *Philos Trans A Math Phys Eng Sci.* 365(1851):303-315.

[Hao; 2010] Hao, S. (2010). I-35W bridge collapse. *Journal of Bridge Engineering.* 15(5):608-614.

[Inaudi & Deblois; 2009] Inaudi, D. Deblois, R. (2009). Overview of 40 bridge structural health monitoring projects. *26th International Bridge Conference.* Pennsylvania, PA.

[Inman et al.; 2005] Inman, D. Farrar, C. Lopes, V. (2005). *Damage Prognosis: For Aerospace, Civil and Mechanical Systems.* New York: Wiley.

[Schutz; 1996] Schutz, W. (1996). A history of fatigue. *Engineering Fracture Mechanics.* 54(2):263-300.

[Stephens et al.; 2000] Stephens, RI. Fatemi, A. Stephens, RR. Fuchs, HO. (2000). *Metal Fatigue in Engineering.* New York: Wiley, 2.

[USDOH; 2010] U.S. Department of Homeland Security, S. and Technology. (2010). Aging infrastructure: Issues, research, and technology. *Building and Infrastructure Protection Series.*

[van Gent et al.; 2007] van Gent, RN. Siem, D. van Middelkoop, M. (2007). Incidence and determinants of lower extremity running injuries in long distance runners: a systematic review. *British Journal of Sports Medicine.* 41:469-480.

Chapter 2

Fundamentals

This chapter provides the preliminary knowledge to understand the topics covered in the following chapters. It will cover the fundamental principles of system theory, fatigue theory, and structural health monitoring to generate the fatigue monitoring framework for structural and biomechanical systems. A high-level model of the frame-
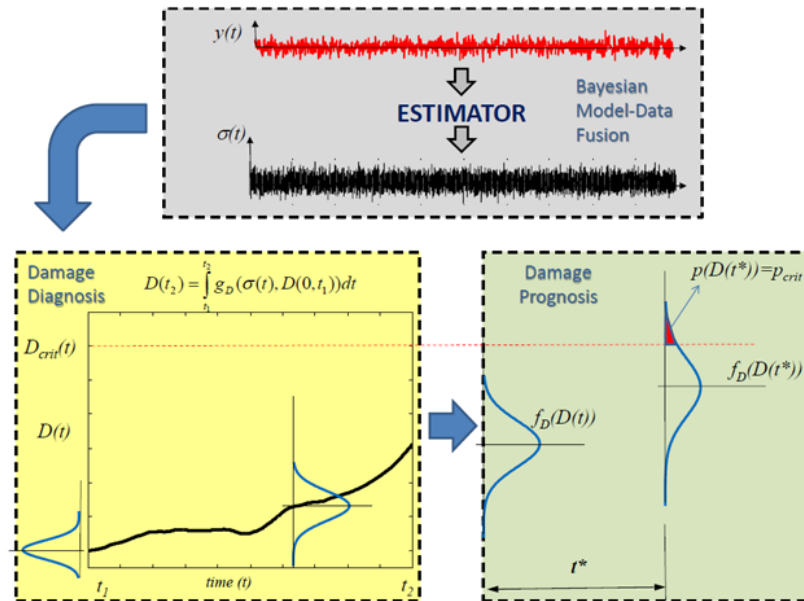
Figure 2.1: Fatigue monitoring framework for structural and biomechanical systems

work is presented in Fig. 2.1, which should become clear after reading this section in its entirety.

2.1   SYSTEM THEORY

Physical systems are studied with a combination of modeling, mathematical equations, analysis and design to understand the systems performance. The system is influenced by various inputs that determine its response which can be measured. If the performance is unsatisfactory then one or more of these parts need to be adjusted in order to improve its performance.

First the physical system needs to be modeled. The model will be dependent on the question that is asked. For example a building might be modelled as a rigid body when subject to static loading conditions but might be modelled as a spring-mass-damper system when determining its response to wind excitation.

After the model is selected the various physical laws are applied in order to develop the mathematical equations that describe the system. For this dissertation the author is interested in structural and biomechanical systems that are subject to Newton's law. These equations might be linear, nonlinear, integral, difference, or differential equations among others.

Next the analysis is carried out in a qualitative and/or quantitative nature. Quantitative analysis determines the response of the system that is excited by inputs; while qualitative analysis defines the parameters of the system such as stability, controllability, and observability. Typically design techniques are influenced by the qualitative analyses performed.

When the response of the system is unsatisfactory, the model has to be adjusted. This can be achieved by adjusting specific parameters of the system; or it could be achieved by introducing compensators. If the model is optimal then the performance of the physical system should be improved by these adjustments or compensators; when this is not the case then the model is incorrect for the given system.

The systems that will be covered in this dissertation are limited to linear systems that have the following equation to describe the relationship between the input $\mathbf{u}$ and output $\mathbf{y}$,

$$y(t) = \int_{t_o}^{t} \mathbf{G}(t, \tau)\mathbf{u}(\tau)d\tau \tag{2.1}$$

This is defined as the input-output description. When the linear system is lumped and time invariant it can be described by,

$$\dot{x}(t) = \mathbf{A}_c x(t) + \mathbf{B}_c u(t) + w(t) \tag{2.2}$$

$$y(t) = \mathbf{C}_c x(t) + \mathbf{D}_c u(t) + r(t) \tag{2.3}$$

Equation 2.2, the state equation, is a set of first-order differential equations and Equation 2.3, the measurement equation, is a set of algebraic equations that define the internal description for the linear system. The vector x is called the state; for structural and biomechanical systems this will consist of displacements and velocities, and the set of two equations are called the state-space representation of the system. $\mathbf{A_c}$ is the n x n continuous state transition matrix, $\mathbf{B_c}$ is the n x p continuous input matrix, $\mathbf{C_c}$ is the m x n continuous measurement matrix, and $\mathbf{D_c}$ is the m x p continuous direct transmission matrix. The process noise is denoted as $w(t)$ and the measurement noise is denoted as $r(t)$

14

Note that these are continuous-time equations in which the variable t is defined at every time instant $(-\infty, \infty)$, however in real world applications measurements are taken at discrete points in time. Therefore the discrete time state space representation is defined as,

$$\dot{x}_{k+1} = \mathbf{A}x_k + \mathbf{B}u_k + w_k \tag{2.4}$$

$$y_{k+1} = \mathbf{C}x_k + \mathbf{D}u_k + r_k \tag{2.5}$$

where the discrete state transition matrix and discrete input matrix are defined as,

$$\mathbf{A} = e^{\mathbf{A_c}dt} \tag{2.6}$$

$$\mathbf{B} = [\mathbf{A} - \mathbf{I}]\mathbf{A_c}^{-1}\mathbf{B_c} \tag{2.7}$$

while the measurement matrix and direct transmission matrix remain unchanged; $\mathbf{C} = \mathbf{C_c}, \mathbf{D} = \mathbf{D_c}$. w_k is the process noise, and r_k is the measurement noise. The system response will be the solution to the problem that is excited by the initial state $x(0)$ and the input $u(0)$ which is formally presented in Fig. 2.2. The fundamental statement is that the state can be reconstructed at unmeasured locations of the system from known measurements.

2.1.1   SYSTEM MODEL

In reality, all biomechanical and structural systems have an infinite number of degrees of freedom. Meaning that there is an infinite number of coordinates necessary to fully define a systems configuration. A degree of freedom is defined as a systems movement in a prescribed direction. For this dissertation each node can have axial
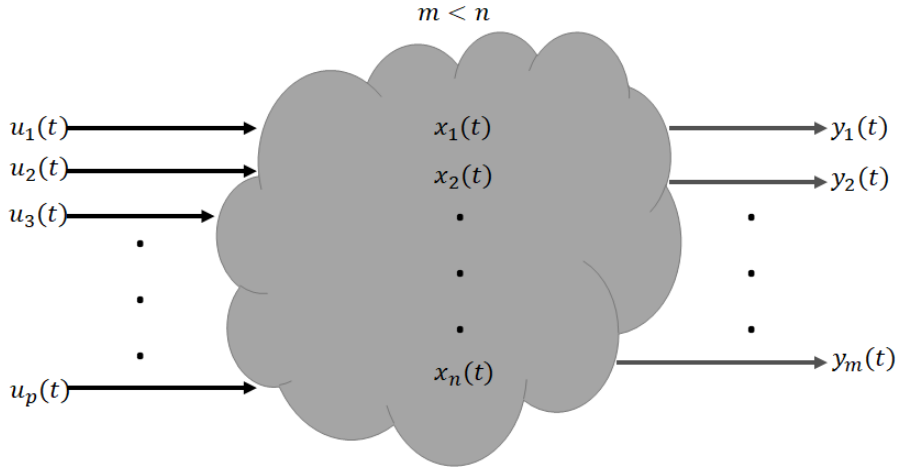
Figure 2.2: The state space representation with a system with n states, m measurements and p inputs.

motion, shear motion, and rotational motion. The simplest model for any system is a single degree of freedom (SDOF), where only one spatial coordinate is required to define it's configuration.

Throughout this dissertation the model will consist of mass-spring-damper (MSD) models. Therefore the description of a mass matrix, a stiffness matrix and a classical damping matrix for all degrees of freedom will fully define the system model. For the SDOF case with vertical motion, the mass matrix is m_1, the stiffness matrix is k_1, and the damping matrix is c_1, which is presented in Fig. 2.3. For most systems a SDOF model won't provide an accurate representation of the system therefore a more complex multidegree-of-freedom (MDOF) system is typically required.

The MDOF system will consist of nodes and elements that are combined to generate a planar frame finite element model (FEM) representation of the system which is presented in Fig 2.4. Each element has six DOFs, a length (L_{ij}), an elastic modulus (E_{ij}), moment of inertia (I_{ij}), and a cross sectional area (A_{ij}). The mass matrix is a
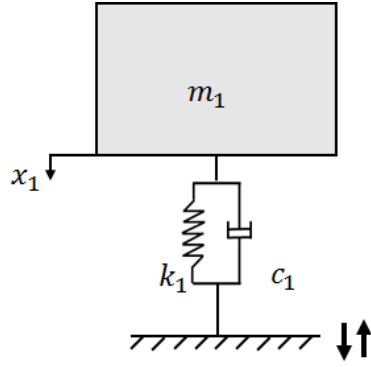
Figure 2.3: Structural and biomechanical SDOF model
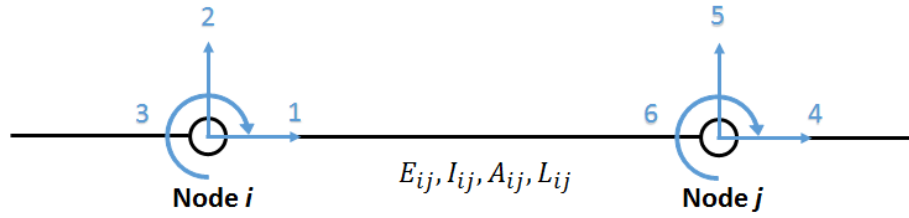
Figure 2.4: Element framework for a 2D Planar Frame

diagonal matrix of the form,

$$\mathbf{M} = \begin{bmatrix} m_1 & 0 & 0 & \ldots & 0 \\ 0 & m_2 & 0 & \ldots & 0 \\ & & \vdots & & \\ 0 & 0 & 0 & \ldots & m_n \end{bmatrix} \tag{2.8}$$

where m is the mass for shear and axial motion and the mass moment of inertia for rotational motion for each node. The stiffness matrix is formulated at the element or local level then related to the global coordinates in post processing which results in

17

a band matrix. The local stiffness matrix is defined as,

$$
\mathbf{K_{ij}} =
\begin{bmatrix}
\frac{A_{ij}E_{ij}}{L_{ij}} & 0 & 0 & \frac{-A_{ij}E_{ij}}{L_{ij}} & 0 & 0 \\[8pt]
0 & \frac{12E_{ij}I_{ij}}{L_{ij}^3} & \frac{6E_{ij}I_{ij}}{L_{ij}^2} & 0 & \frac{-12E_{ij}I_{ij}}{L_{ij}^3} & \frac{6E_{ij}I_{ij}}{L_{ij}^2} \\[8pt]
0 & \frac{6E_{ij}I_{ij}}{L_{ij}^2} & \frac{4E_{ij}I_{ij}}{L_{ij}} & 0 & \frac{-6E_{ij}I_{ij}}{L_{ij}^2} & \frac{2E_{ij}I_{ij}}{L_{ij}} \\[8pt]
\frac{-A_{ij}E_{ij}}{L_{ij}} & 0 & 0 & \frac{A_{ij}E_{ij}}{L_{ij}} & 0 & 0 \\[8pt]
0 & \frac{-12E_{ij}I_{ij}}{L_{ij}^3} & \frac{-6E_{ij}I_{ij}}{L_{ij}^2} & 0 & \frac{12E_{ij}I_{ij}}{L_{ij}^3} & \frac{-6E_{ij}I_{ij}}{L_{ij}^2} \\[8pt]
0 & \frac{6E_{ij}I_{ij}}{L_{ij}^2} & \frac{2E_{ij}I_{ij}}{L_{ij}} & 0 & \frac{-6E_{ij}I_{ij}}{L_{ij}^2} & \frac{4E_{ij}I_{ij}}{L_{ij}}
\end{bmatrix}
\tag{2.9}
$$

for each element. The damping matrix is a function of the mass and stiffness matrix and is formulated as follows,

$$
\mathbf{C_d} = [\Phi]^T [c] [\Phi]
\tag{2.10}
$$

where C_d is diagonal for a special case of c, in which $c = 2M\omega\xi$. ω is the natural frequency, ξ is the modal damping factor, and Φ are the eigenvectors. The damping is classical for the special case when c is proportional to the mass and/or stiffness. The damping is considered Rayleigh damping when its the special case of $c = \alpha[M] + \beta[K]$

2.1.2   EQUATIONS OF MOTION

For this dissertation attention is restricted to structural and biomechanical systems whose dynamic response can be described by the following matrix ordinary differential equation

$$
\mathbf{M}\ddot{q}(t) + \mathbf{C_D}\dot{q}(t) + \mathbf{K}q(t) = \mathbf{b_2}u(t)
\tag{2.11}
$$

where $q(t) \in \mathbf{R}^{nx1}$ is the displacement vector at time t, $\mathbf{M}$ is the mass matrix, $\mathbf{C_D}$ is the damping matrix, and $\mathbf{K}$ is the stiffness matrix. The time history of the

unknown forcing is $u(t) \in \mathbf{R}^{1 x n}$, and $\mathbf{b_2} \in \mathbf{R}^{nx1}$ is the force distribution matrix vector.

Formulated in state space representation the state, $x = \begin{bmatrix} q \\ \dot{q} \end{bmatrix}$ and,

$$\mathbf{A_c} = \begin{bmatrix} \mathbf{0} & \mathbf{I} \\ -\mathbf{M^{-1}K} & -\mathbf{M^{-1}C_d} \end{bmatrix} ; \mathbf{B_c} = \begin{bmatrix} \mathbf{0} \\ \mathbf{M^{-1}b_2} \end{bmatrix} \tag{2.12}$$

The measurements of the system's response are defined by

$$y(t) = \mathbf{C}x(t) + \mathbf{D}u(t) + r(t) \tag{2.13}$$

where $r(t) \in \mathbf{R}^{mx1}$ is the measurement noise. The measurement equation will have the following structure depending on the type of measurement,

$$\mathbf{C_{dis}} = \begin{bmatrix} \mathbf{c_2} & \mathbf{0} \end{bmatrix} \tag{2.14}$$

$$\mathbf{C_{vel}} = \begin{bmatrix} \mathbf{0} & \mathbf{c_2} \end{bmatrix} \tag{2.15}$$

$$\mathbf{C_{acc}} = \begin{bmatrix} -\mathbf{c_2M^{-1}K} & -\mathbf{c_2M^{-1}C_d} \end{bmatrix} \tag{2.16}$$

and $\mathbf{D_{dis}} = \mathbf{D_{vel}} = \mathbf{0}$,

$$\mathbf{D_{acc}} = \mathbf{c_2M^{-1}b_2} \tag{2.17}$$

where $\mathbf{c_2} \in \mathbf{R}^{mxn}$ maps the degrees of freedom to the measurements.

2.1.3   OBSERVABILITY

The concept of observability examines the ability of estimating the state from the output measurements. The discrete-time state equation is observable if for any unknown initial state x_0, there exists a finite integer $k_1 > 0$ such that the knowledge of the input sequence u_k and the output sequence y_k over $[k = 0, k_1]$ uniquely determine the initial state x_0. Observability is determined from the pair (A, C) which is formulated into the observability matrix,

$$\mathbf{O} = \begin{bmatrix} \mathbf{C} \\ \mathbf{CA} \\ \vdots \\ \mathbf{CA^{n-1}} \end{bmatrix} \tag{2.18}$$

If the observability matrix is full rank then the states can be reconstructed from the output of the system. For structural and biomechanical systems that means that the stress at a point will be observable if all the displacements that determine the stress are observable. To determine stresses the Euler Bernoulli Beam curvature equations are used,

$$\sigma = \frac{Mc}{I} \tag{2.19}$$

where M is the moment, c is the distance from the neutral axis, and I is the moment of inertia.

2.1.4 MODEL BASED OBSERVER

The model based observer was originally derived by Hernandez [Hernandez; 2011], and can be written in second order form as,

$$\mathbf{M}\ddot{\hat{q}}(t) + (\mathbf{C_d} + \mathbf{c_2^T E c_2})\dot{\hat{q}}(t) + \mathbf{K}\hat{q}(t) = \mathbf{c_2^T E} y(t) \tag{2.20}$$

under the assumption of velocity measurements. The proposed estimator becomes a modified version of the system with added dampers at measurement locations and excited by forces that are linear combinations of the output measurements and proportional to the added dampers. A visual representation of this is presented in Fig. 2.5. The matrix $\mathbf{E}$ is selected in such a way to minimize the trace of the state error
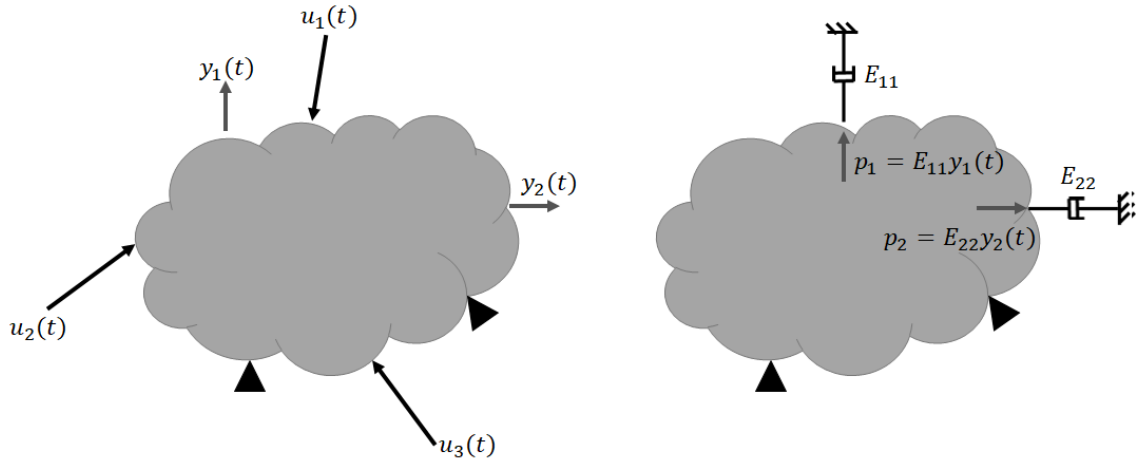
Figure 2.5: Visualization of the MBO with added dampers to the system model at locations of measurements.

covariance matrix. If measurements are accelerations then masses are added and if displacements then springs are added to the system. However, when dampers are added to the system the dynamic properties, i.e modal shapes and frequencies are

unchanged. This results in lower estimation error than in the cases of displacements and acceleration due to the distortion in these frequencies.

The state error is defined as $e = q - \hat{q}$, therefore the state error is given by,

$$\mathbf{M}\ddot{e}(t) + (\mathbf{C_d} + \mathbf{c_2^T}\mathbf{E}\mathbf{c_2}\dot{e}(t) + \mathbf{K}e(t) = \mathbf{b_2}u(t) - \mathbf{c_2}\mathbf{E}r(t) \tag{2.21}$$

The matrix $\mathbf{E}$ ends up on both sides and is free to be selected. As $\mathbf{E}$ increases the effective damping at measurement locations is increased which will reduce the estimation error. However, on the right hand side of the equation it is proportional to the measurement noise which will increase the estimation error. Therefore an optimization algorithm is necessary to determine the optimal $\mathbf{E}$.

To determine the state error covariance, the Fourier transform of both sides of Eq. 2.21 is taken,

$$(-\mathbf{M}\omega^2 + (\mathbf{C_d} + \mathbf{c_2^T}\mathbf{E}\mathbf{c_2})i\omega + \mathbf{K})e(\omega) = \mathbf{b_2}u(\omega) - \mathbf{c_2^T}\mathbf{E}r(\omega) \tag{2.22}$$

and define $\mathbf{G}, \mathbf{H_o}$ as,

$$\mathbf{G}(\omega) = -\mathbf{M}\omega^2 + \mathbf{C_d}i\omega + \mathbf{K} \tag{2.23}$$

$$\mathbf{H_o}(\omega) = (\mathbf{G}(\omega) + \mathbf{c_2^T}\mathbf{E}\mathbf{c_2}i\omega)^{-1} \tag{2.24}$$

then the state error estimate in the frequency domain is written as,

$$e(\omega) = \mathbf{H_o}(\omega)(\mathbf{b_2}u(\omega) - \mathbf{c_2^T}\mathbf{E}r(\omega)) \tag{2.25}$$

If the general assumption that the measurement noise and unmeasured excitation are

uncorrelated is used, and due to the required symmetry of the estimators damping matrix $\mathbf{E} = \mathbf{E^T}$, the spectral density matrix of the state error $\mathbf{S_{ee}}(\omega)$ can be expressed as

$$\mathbf{S_{ee}}(\omega) = \mathbf{H_o}(\omega)\mathbf{b_2}\mathbf{S_{uu}}(\omega)\mathbf{b_2^T}\mathbf{H_o^*}(\omega) + \mathbf{H_o}(\omega)\mathbf{c_2^T}\mathbf{E}\mathbf{S_{rr}}(\omega)\mathbf{E}\mathbf{c_2}\mathbf{H_o^*}(\omega) \qquad (2.26)$$

where $\mathbf{S_{uu}}$ is the spectral density matrix of the unmeasured excitation and $\mathbf{S_{rr}}$ is the spectral density of the noise. The covariance matrix of the state error can then be expressed as

$$\mathbf{P} = \int_{-\infty}^{+\infty} \mathbf{S_{ee}}d\omega = \int_{-\infty}^{+\infty}(\mathbf{H_o}(\omega)\mathbf{b_2}\mathbf{S_{uu}}(\omega)\mathbf{b_2^T}\mathbf{H_o^*}(\omega) + \mathbf{H_o}(\omega)\mathbf{c_2^T}\mathbf{E}\mathbf{S_{rr}}(\omega)\mathbf{E}\mathbf{c_2}\mathbf{H_o^*}(\omega))d\omega$$

$$(2.27)$$

The objective function then becomes to select the matrix $\mathbf{E}$ such that

$$\frac{\partial}{\partial \mathbf{E}}tr(\mathbf{P}) = \frac{\partial}{\partial \mathbf{E}}J_1 = 0 \qquad (2.28)$$

Note that only the displacement portion of the state error covariance is being minimized. The optimal $\mathbf{E}$ does not have an analytical closed-form solution therefore numerical optimization is required. This can be performed in $MATLAB^\circledR$ by using the built-in optimization function, $fminsearch$. If only the diagonal of $\mathbf{E}$ is used the optimization is not numerically intensive and gives the following form for the $\mathbf{E}$ matrix,

$$\mathbf{E} = \begin{bmatrix} E_{11} & 0 & 0 & \ldots & 0 \\ 0 & E_{22} & 0 & \ldots & 0 \\ & & \vdots & & \\ 0 & 0 & 0 & \ldots & E_{nn} \end{bmatrix} \qquad (2.29)$$

The FEM based observer then estimates the state using the second order form (Eq. 2.20) with the previously determined damper matrix.

2.1.5   KALMAN FILTER

The Kalman filter [Kalman; 1960] is a two-step recursive algorithm. First the Kalman filter estimates the current state variables and their associated uncertainties, beginning with the following relations

$$\hat{x}_{k+1}^{(+)} = x_{k+1} + \tilde{x}_{k+1}^{(+)} \tag{2.30}$$

$$\hat{x}_{k+1}^{(-)} = x_{k+1} + \tilde{x}_{k+1}^{(-)} \tag{2.31}$$

the tilde denotes estimation error, the hat denotes an estimate, the + denotes a posteriori and the - denotes a priori. From the assumed form of the linear estimator,

$$\hat{x}_{k+1}^{(+)} = \mathbf{K}_{k+1}'\hat{x}_{k+1}^{(-)} + \mathbf{K_{k+1}}y_{k+1} \tag{2.32}$$

If w_k, r_k are gaussian, the filter that is found will be the optimal linear filter in terms of minimizing the euclidean norm of the estimation error. The estimation error is determined as,

$$\tilde{x}_{k+1}^{(+)} = [\mathbf{K_{k+1}'} + \mathbf{K_{k+1}}\mathbf{C} - \mathbf{I}]x_{k+1} + \mathbf{K_{k+1}'}\tilde{x}_{k+1}^{(-)} + \mathbf{K_{k+1}}r_{k+1} \tag{2.33}$$

where K_{k+1}' and K_{k+1} are time varying weighting matrices that will be defined later. By definition the expected value of the measurement noise is zero or, $E[r_k] = 0$. To

generate an unbiased estimator for any given state vector, x_k, the expected value of the state error must also be zero, $E[\tilde{x}_k^{(-)}] = 0$. This results in,

$$\mathbf{K}'_{\mathbf{k+1}} = \mathbf{I} - \mathbf{K}_{\mathbf{k+1}}\mathbf{C} \tag{2.34}$$

and the estimator will take the form,

$$\hat{x}_{k+1}^{(+)} = (\mathbf{I} - \mathbf{K}_{\mathbf{k+1}}\mathbf{C})\hat{x}_{k+1}^{(-)} + K_{k+1}y_{k+1} \tag{2.35}$$

then the state estimate of a dynamical system $\hat{x}_{k+1}^{(-)}$ at time $t = (k+1)\Delta t$ is corrected by using a weighted difference between model predictions and measurements in its re-written form,

$$\hat{x}_{k+1}^{(+)} = \hat{x}_{k+1}^{(-)} + \mathbf{K}_{k+1}\left(y_{k+1} - \mathbf{C}\hat{x}_{k+1}^{(-)}\right) \tag{2.36}$$

where $\hat{x}_{k+1}^{(+)}$ is the corrected (a posteriori) state estimate and $\hat{x}_{k+1}^{(-)}$ is the a priori state estimate computed for this system as,

$$\hat{x}_{k+1}^{(-)} = \mathbf{A}\hat{x}_{k}^{(+)} \tag{2.37}$$

The recursion method is briefly presented here. A detailed derivation of the gain can be found in [Simon; 2006, Gelb; 1996]. First consider $\mathbf{P}_{k+1}^{(-)}$, the priori state error covariance matrix at time $t = (k+1)\Delta t$, expressed in the following form

$$E[(x_{k+1} - \hat{x}_{k+1})^T(x_{k+1} - \hat{x}_{k+1})] = \mathbf{P}_{k+1}^{(-)} = \mathbf{A}\mathbf{P}_k^{(+)}\mathbf{A}^T + \mathbf{Q}_k \tag{2.38}$$

where $\mathbf{Q}_k$ is the covariance matrix of the unmeasured excitation and $\mathbf{P}_k^{(+)}$ is the posteriori state error covariance at the previous time step. The Kalman feedback gain matrix, $\mathbf{K}_{k+1}$ at time $t = (k+1)\Delta t$, is expressed as

$$\mathbf{K}_{k+1} = \mathbf{P}_{k+1}^{(-)}\mathbf{C}^T\left(\mathbf{C}\mathbf{P}_{k+1}^{(-)}\mathbf{C}^T + \mathbf{R}_{k+1}\right)^{-1} \tag{2.39}$$

where $\mathbf{R}_{k+1}$ is the measurement noise covariance. The a posteriori state error covariance matrix is given by

$$\mathbf{P}_{k+1}^{(+)} = (\mathbf{I} - \mathbf{K}_{k+1}\mathbf{C})\mathbf{P}_{k+1}^{(-)} \tag{2.40}$$

The two step recursive method of the KF is presented visually in Fig. 2.6.

2.1.6   UNSCENTED KALMAN FILTER

The unscented Kalman filter (UKF) is a standard technique used for nonlinear estimation and machine learning applications. This includes estimating the state of a nonlinear dynamical system, estimating parameters for nonlinear system identification, and dual estimation where both the state and unknown parameters are estimated simultaneously. The UKF was proposed by Julier and Uhlman [Julier & Uhlmann; 1997] in order to introduce improvements to the Extended Kalman filter (EKF) during the propagation of the Gaussian random variable (GRV) through the system dynamics. The state distribution is approximated as a GRV which is then propagated through the first-order linearization of the nonlinear system by determining the Jacobian of the state matrix and possibly the measurement matrix if dual estimation is performed. This can lead to large errors in the posterior mean and covariance of the GRV which leads to sub-optimal performance and in many cases divergence. A

26

x_{k-1}

$\hat{x}_{k-2}$ $\vdots$ $\hat{x}_{k-1}$ $\longrightarrow$ $\hat{x}_{k-1}$ $\vdots$ $\hat{x}_k$

t_{k-1} $\qquad$ t_k

(a)

y_{k-1} $\qquad$ y_k

$\hat{x}_{k-1}^{(-)}$ $\vdots$ $\hat{x}_{k-1}$ $\xrightarrow{\textbf{A}}$ $\hat{x}_k^{(-)}$ $\vdots$ $\hat{x}_k$

t_{k-1} $\qquad$ t_k
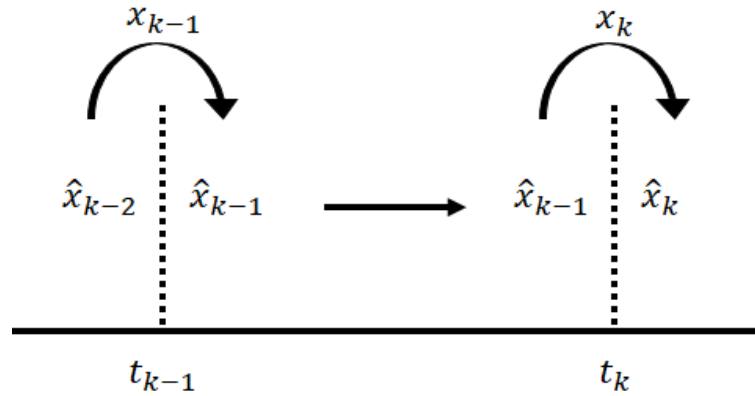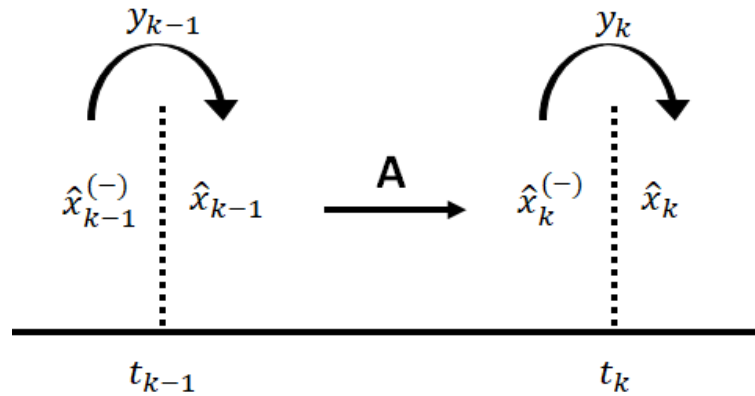
(b)

Figure 2.6: Two step recursive method of the KF, (a) The time update for the covariance, (b) The measurement update for the estimated state

detailed derivation of the EKF can be found in [Jazwinski; 1970, Gelb; 1996].

The UKF addresses this issue by providing a deterministic sampling approach without the requirements of a large number of GRV realizations like with Monte-Carlo methods. Much like the EKF, the state distribution is approximated as a GRV; however the distribution is represented by a minimal set of chosen sigma points. These sample points will completely capture the mean and covariance of the GRV,

and when these points are propagated through the true nonlinear system, the mean and covariance will be accurately determined to the 3rd order taylor series expansion for any nonlinearity. This process is known as the unscented transformation, in which one can determine the statistics of random variable that undergoes a nonlinear transformation. If sigma points are chosen carefully, Z_k, based on the mean and covariance of x, and put through any nonlinear function $y = f(x)$ the mean and covariance of $f(Z_k)$ can be determined which will have the same mean and covariance of y. This process is depicted in Fig.2.7. Assume that x, a length n vector, has a
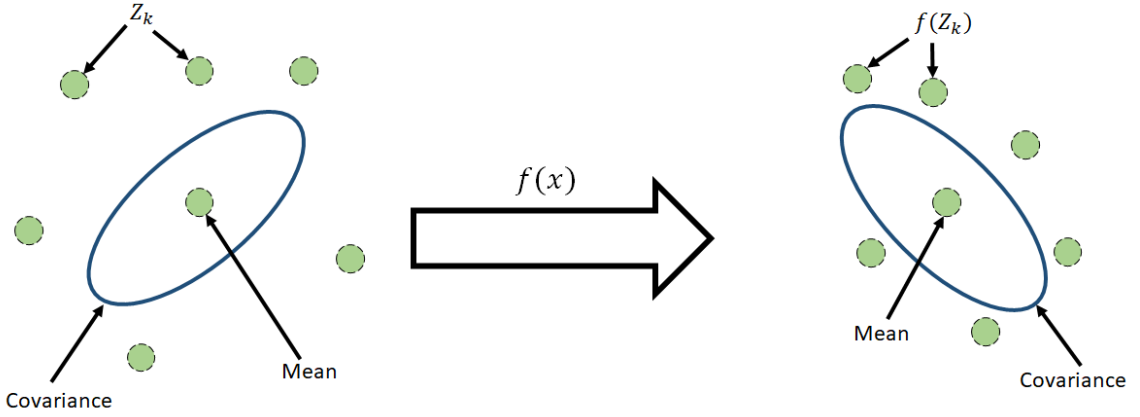
Figure 2.7: The unscented transformation

mean of $\bar{x}$ and a covariance $\mathbf{P_x}$. To evaluate the statistics of y the sigma matrix Z of $2n + 1$ sigma vectors Z_i with corresponding weights W_i is formed as,

$$Z_0 = \bar{x} \tag{2.41}$$

$$Z_i = \bar{x} + (\sqrt{(n + \lambda)\mathbf{P_x}})_i \qquad i = 1, ..., n \tag{2.42}$$

$$Z_i = \bar{x} - (\sqrt{(n + \lambda)\mathbf{P_x}})_{i-n} \qquad i = n + 1, ..., 2n \tag{2.43}$$

$$W_0^m = \lambda/(n + \lambda) \tag{2.44}$$

$$W_0^c = \lambda/(n + \lambda) + (1 - \alpha^2 + \beta) \tag{2.45}$$

$$W_i^m = W_i^c = 1/(2(n + \lambda)) \qquad i = 1, ..., 2n \tag{2.46}$$

where $\lambda = \alpha^2(n + \kappa) - n$ is a scaling parameter, α determines the spread of the sigma points around the mean, κ is a secondary scaling parameter, and β incorporates prior knowledge of the distribution. The sigma vectors are then propagated through the nonlinear function,

$$Y_i = f(Z_i) \qquad i = 0, ..., 2n \tag{2.47}$$

then the mean and covariance of y are approximated by the weighted sample mean and covariance of the posterior sigma points,

$$y \approx \sum_{i=0}^{2n} W_i^m Y_i \tag{2.48}$$

$$\mathbf{P_y} \approx \sum_{i=0}^{2n} W_i^c \{Y_i - y\}\{Y_i - y\}^T \tag{2.49}$$

Briefly presented below is the formulation of the dual estimation approach for the UKF. For a full derivation refer to [Wan & Van Der Merwe; 2000]. First consider the discrete-time nonlinear dynamic system,

$$x_{k+1} = f(z_k, u_k) + w_k \tag{2.50}$$

$$y_k = g(z_k, u_k) + r_k \tag{2.51}$$

where z_k is the augmented state vector, which includes the states and the unknown

parameters that need to be estimated, $z_k = [x_k, \ \theta_k]^T$. The process begins by calcu-
lating the sigma points as,

$$Z_k = [\hat{z}_k \quad \hat{z}_k \pm \sqrt{(n+\lambda)\mathbf{P_k^z}}] \tag{2.52}$$

where P_k^z is the covariance of the augmented state vector. In the time update step
the sigma points are put through the state equations as,

$$Z_{k+1}^{(-)} = f(Z_k, w_k) \tag{2.53}$$

$$\hat{z}_{k+1}^{(-)} = \sum_{i=0}^{2n} W_i^m Z_{i,k+1}^{(-)} \tag{2.54}$$

with the a priori covariance determined as,

$$\mathbf{P}_{k+1}^{(-)} = \sum_{i=0}^{2n} W_i^c [Z_{i,k+1}^{(-)} - \hat{z}_{k+1}^{(-)}][Z_{i,k+1}^{(-)} - \hat{z}_{k+1}^{(-)}]^T \tag{2.55}$$

The sigma points are then put through the measurement equation as,

$$Y_{k+1}^{(-)} = g(Z_{k+1}^{(-)}, r_k) \tag{2.56}$$

$$\hat{y}_{k+1}^{(-)} = \sum_{i=0}^{2n} W_i^m Y_{i,k+1}^{(-)} \tag{2.57}$$

In the measurement update phase the covariance and cross-covariance of the measure-
ments are updated to the state to determine the Kalman gain to provide a estimate
of the augmented state and covariance.

$$\mathbf{P}_{yy} = \sum_{i=0}^{2n} W_i^c [Y_{i,k+1}^{(-)} - \hat{y}_{k+1}^{(-)}][Y_{i,k+1}^{(-)} - \hat{y}_{k+1}^{(-)}]^T \tag{2.58}$$

$$\mathbf{P}_{xy} = \sum_{i=0}^{2n} W_i^c [Z_{i,k+1}^{(-)} - \hat{z}_{k+1}^{(-)}][Y_{i,k+1}^{(-)} - \hat{y}_{k+1}^{(-)}]^T \tag{2.59}$$

$$\mathbf{K}_{k+1} = \mathbf{P}_{xy}\mathbf{P}_{yy}^{-1} \tag{2.60}$$

Similar to the standard kalman filter the augmented state and covariance is updated as,

$$\hat{z}_{k+1} = \hat{z}_{k+1}^{(-)} + \mathbf{K}_{k+1}(y_{k+1} - \hat{y}_{k+1}^{(-)} \tag{2.61}$$

$$\mathbf{P}_{k+1} = \mathbf{P}_{k+1}^{(-)} - \mathbf{K}_{k+1}\mathbf{P}_{yy}\mathbf{K}_{k+1}^T \tag{2.62}$$

This ends the formulation of the UKF, in its implementation it has shown to consistently achieve better accuracy than other methods such as the EKF at a similar computational cost.

2.1.7 State-input-parameter estimation process

A dual observer was established by Dertimanis et al, which combines the dual and unscented Kalman filter (UKF) for state-input parameter estimation. The dual Kalman filter (DKF) determines the unknown structural excitation while the latter solves the state and parameter estimation by means of an augmented state-space formulation. For brevity the key components of the process are highlighted; for a full derivation refer to [Dertimanis et al.; 2019]. The derivation begins by introducing two fictitious equations

$$u_{k+1} = \mathbf{T}u_k + w_k^u \tag{2.63}$$

$$\theta_{k+1} = \theta_k + w_k^\theta \tag{2.64}$$

where $\mathbf{T}$ denotes a state matrix and w_k^u, w_k^θ are zero mean Gaussian processes of covariance matrices Q_{uu} and $Q_{\theta\theta}$, respectively. The augmented state vector is defined as $z_k = [x_k, \theta_k]^T \in \mathbf{R}^{\bar{n}x1}$, for $\bar{n} = 2n + d$, in which the new augmented state-space model is formulated as

$$z_{k+1} = \begin{bmatrix} \mathbf{A} & \mathbf{0} \\ \mathbf{0} & \mathbf{I} \end{bmatrix} z_k + \begin{bmatrix} \mathbf{B} \\ \mathbf{0} \end{bmatrix} u_k + \begin{bmatrix} \mathbf{w_k^x} \\ \mathbf{w_k^\theta} \end{bmatrix} = f(z_k, u_k) + p_k \tag{2.65}$$

$$y_{k+1} = \begin{bmatrix} \mathbf{C} & \mathbf{0} \end{bmatrix} z_k + \begin{bmatrix} \mathbf{D} \end{bmatrix} u_k + r_k = g(z_k, u_k) + r_k \tag{2.66}$$

where w_k^x is uncorrelated with w_k^θ, and is superimposed to Eq. 8. The process noise of the augmented state equation is denoted as p_k which again has zero mean and covariance matrix $Q_{pp} = \text{diag}\{Q_{xx}, Q_{\theta\theta}\}$. The zero mean Gaussian measurement noise is denoted as r_k with a covariance matrix R.

2.1.8   Input Estimation

A new state-space model is considered when an estimate of θ_k becomes available through the UKF, which is a function of the the measured output, y_k, the unknown state, u_k, and known input to the system, x_k

$$\hat{u}_{k+1}^- = T\hat{u}_k + w_k^u \tag{2.67}$$

$$\hat{y}_{k+1} = C\hat{x}_k + D\hat{u}_k + r_k \tag{2.68}$$

The dual Kalman filter is then implemented to provide an online estimation of $\hat{u}_k$. In the measurement update step the input gain, mean and covariance are calculated as follows

$$K^u_{k+1} = (DP^{u-}_{k+1}D^T + R)^{-1}P^{u-}_{k+1}D^T \tag{2.69}$$

$$\hat{u}^+_{k+1} = \hat{u}^-_{k+1} + K^u_{k+1}(y_{k+1} - C\hat{x}^-_{k+1} - D\hat{u}^-_{k+1}) \tag{2.70}$$

$$P^{u+}_{k+1} = P^{u-}_{k+1} - K^u_{k+1}D^T P^{u-}_{k+1} \tag{2.71}$$

the one-step ahead predictions of the input mean, input covariance and state mean at time k are denoted as u^-_{k+1}, P^{u-}_{k+1} and x^-_{k+1} respectively. During the time update step, the input mean and covariance predictions are determined by

$$\hat{u}^-_{k+1} = T\hat{u}^+_k \tag{2.72}$$

$$P^{u-}_{k+1} = TP^{u-}_{k+1}T^T + Q_{uu} \tag{2.73}$$

2.1.9 STATE AND PARAMETER ESTIMATION

Here the UKF is employed to obtain a solution to the joint state and parameter estimation problem. The UKF is based on the unscented transformation. Sigma points, Z_k, are carefully chosen based on the mean and covariance of the state, z_k, and when these points are put through the function $f(x)$ the mean and covariance of $f(Z_k)$ will have the same mean and covariance of $f(z_k)$. The set of sigma points are calculated when the input estimate u^+_k from the DKF and a measurement, y_k,

becomes available by

$$\hat{Z}_k^+ = [\hat{z}_k^+ ... \hat{z}_k^+] + \sqrt{c} \left[\mathbf{0} \ \sqrt{P_k^{z+}} ... - \sqrt{P_k^{z+}} \right] \tag{2.74}$$

where c is a function of the spread of the sigma points. The sigma points are then propagated through the output equation

$$\hat{Y}_{k+1}^+ = g(\hat{Z}_k^+, \hat{u}_k^+) \tag{2.75}$$

The output mean and covariance is then calculated as

$$\hat{y}_{k+1} = \hat{Y}_{k+1}^+ \mu_x \tag{2.76}$$

$$P_{k+1}^y = \hat{Y}_{k+1}^+ M \hat{Y}_{k+1}^{+T} + R \tag{2.77}$$

where μ_x and M are parameters of the UKF which are functions of the first and second-order weightings. From here the cross covariance between the state and the output is calculated

$$P_{k+1}^{xy} = Z_k^+ M \hat{Y}_k^{+T} \tag{2.78}$$

along with the UKF gain

$$K_{k+1}^z = P_{k+1}^{xy} P_{k+1}^{y-1} \tag{2.79}$$

The augmented state mean and covariance matrix are then updated

$$\hat{z}_{k+1}^+ = \hat{z}_{k+1}^- + K_{k+1}^z (y_{k+1} - \hat{y}_{k+1}) \tag{2.80}$$

34

$$P_{k+1}^{z+} = P_{k+1}^{z-} - K_{k+1}^z P_{k+1}^y {K_{k+1}^z}^T \tag{2.81}$$

For the next time update step the sigma points are fed through the state equation to determine the updated sigma points

$$\hat{Z}_{k+1}^- = f(\hat{Z}_k^+, \hat{u}_k^+) \tag{2.82}$$

Then the augmented state mean and covariance is obtained for $k+1$ by

$$\hat{z}_{k+1}^- = \hat{Z}_{k+1}^- \mu_x \tag{2.83}$$

$$P_{k+1}^{z-} = \hat{Z}_{k+1}^- M {\hat{Z}_{k+1}^-}^T + Q_{pp} \tag{2.84}$$

these quantities are then used to calculate the unknown force vector during the next iteration.

2.2   FATIGUE THEORY

This section will focus on the historical development of fatigue monitoring as a branch of technology. The theory will then be applied to structural problems in the assumption that the necessary parameters have been identified through state estimation. Hence it will begin with stress counting and end prior to macroscopic crack growth since that is not the scope of this dissertation. As stated previously, when fatigue cracks have grown to a point where they are visible and can be quantified by visual inspection i.e. crack length, the residual strength of the structure has already been greatly reduced. At this point remediation efforts for structural health monitoring

often can only provide damage location and not the overall current health of the structure at stress critical locations.

2.2.1 HISTORY

The term "fatigue" was originally coined by Braithwaite in his paper 'On the fatigue and consequent fracture of metals' in 1854 [Braithwaite; 1854]. Previously the term "tired" had been used to define the period of usage for metallic structures before breaking. At this time fatigue failures in metallic structures were a well-known technical problem. In the 19th century several serious fatigue failures had already been reported, mainly in the transportation sector and laboratory investigations were being carried out.

This begins with Albert [Albert; 1837], in 1837 designing the first fatigue-test results on conveyor chains that had failed in service. By 1842 Rankine [Rankine; 1842] began discussing the fatigue strength of railway axles. Then in 1853 the first example of a safe life design approach appeared in Morin's book *Resistance des Materiaux* [Morin; 1853] again on train axles. In Braithwaite's fatigue paper he describes several fatigue failures for other systems such as water pumps, propellar shafts, levers, etc. Included in this was a discussion on allowable stress for fatigue-loaded components. Throughout this period there were several disastrous railroad accidents due to fatigue, the most infamous being the Versailles rail accident that resulted in 60 deaths, in combination with thousands of failed railway axles reported by the Institution of Mechanical Engineers.

The first substantial research on fatigue was performed by August Wöhler. He recognized that if a single static load was applied to a structure below its yield strength

it wouldn't result in damage to the structure. However, when that same load was cycled on the structure many times it would induce material failure. In 1867, he presented his work on metal fatigue curves, which were later coined Wöhler or S-N curves, at the Paris World Trade Fair [Wohler; 1867]. These curves related the number of stress cycles to failure within the finite fatigue life region. These were results of fatigue tests on railway axles from a rotating-bending test machine he designed in order to stress cycle the materials. In 1910 Basquin [Basquin; 1910] formulates the Wöhler curve in present day formulation with log-log scales for the stress vs. number of cycles with the following equation to show the linearity of the process for a majority of the stress life,

$$\log(N_f) = K - b\log(\sigma_i) \tag{2.85}$$

where σ_i is the measured stress and K, b are material dependent properties that define the slope and intercept of the curve. At this time numerical values for material parameters were determined from Wöhler's previous research decades prior.

The next substantial research on fatigue monitoring was performed by Palmgren in 1924 [Palmgren; 1924]. His trademark paper focused on extending from the tensile strength of a material to the fatigue limit for the S-N curve using a four-parameter equation. This was the first quantitative description of a probability of life for fatigue-loaded components. Then in 1945 Miner extended this work by defining a damage-accumulation hypothesis,

$$D = \sum_{i=1}^{k} \frac{n_i}{N_i} = 1.0 \tag{2.86}$$

which states that the ratio of the experienced stress cycles to the number of cycles to failure approaches 1.0 at failure. This has been coined as the 'Palmgren-Miner

Damage Accumulation rule' [Miner; 1945]. At the time there were many restrictions that made application for this hypothesis infeasible in practice, however they have since been relaxed. Miner was the first to check his hypothesis by performing fatigue tests.

The work of Wöhler, Palmgren, and Miner provide the fundamental basis for the fatigue monitoring framework used in this dissertation. Fatigue research remained of utmost importance, however research focused on topics such as stress-concentration factors, fatigue limit influencers, design of fatigue testing, fracture mechanics, Goodman diagrams, and the empirical study of material fatigue properties. For an extensive list of fatigue contributions between 1838 and 1987 refer to [Schutz; 1996]

2.2.2 FATIGUE MONITORING

Fatigue is driven by the cyclic or fluctuating stresses or strains, that arise due to the excitation of real-life engineering structures. Mechanical fatigue is the classical example of fatigue in which internal repetitive stresses occur under the excitation of externally applied mechanical loading, which could include forces or displacements. Civil structures such as bridges and buildings, or mechanical components such as gears and pumps are susceptible to this form of fatigue. However, there are other types of fatigue which won't be covered in this dissertation but include thermal fatigue, electrical fatigue, creep fatigue, corrosion fatigue or a combination of those stated.

Fatigue originates from the local yielding of the material regardless of the type of loading condition [Schijve; 2008, Sobczyk; 1992] experienced by the system. The local stress concentration at the microscopic level or grain level of the material can cause dislocations or micro-cracks to form in slip bands. Under the influence of

cyclic stresses these dislocations shift and coalesce to form micro-cracks. It is from these micro-cracks that the formation of a macro-crack begins. The macro-crack will propagate through the structure, in most cases perpendicular to the maximum principle stress direction, which will ultimately lead to structural failure of the system [Cui; 2002,Ottosen et al.; 2008]. Therefore there exists two principle phases to fatigue life of structural systems, namely crack initiation and crack propagation. This is presented in Fig 2.8.
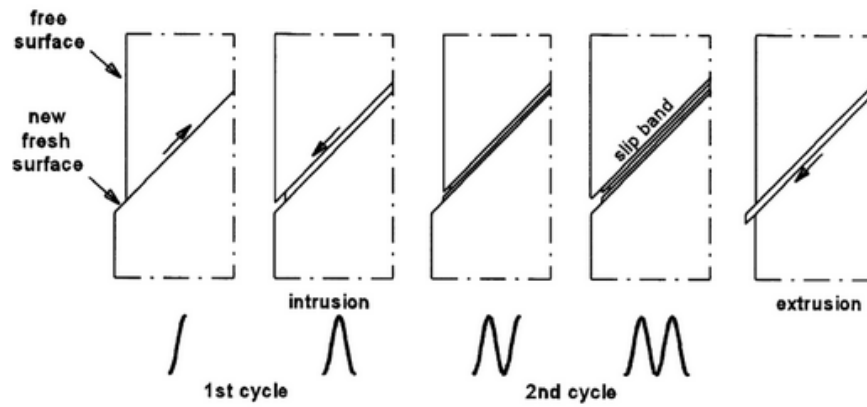
Figure 2.8: Crack initiation by cyclic slip [Schijve; 2008].

The crack initiation phase of mechanical fatigue can be explained as a surface phenomenon. Plasticity, which is a local phenomenon, for initial cycles is restricted to a small number of grains and will be able to occur more effectively when there are no surrounding grains to stop the plastic deformation at the surface. As a consequence of cyclic slips originating from cyclic stresses and the inhomogeneity from grain to grain, micro-plasticity often occurs. The cyclic loading results in the creation of non-reversible slip bands on parallel slip planes. The original initiation has been shown to develop along a slip band in the form of an intrusion or extrusion [Suresh; 2001]. High stress concentrations, geometric discontinuities, inherent material defects,

and surface imperfections lead to the initiation of micro-defects. The micro-cracks will grow into adjacent grains with the growth directions deviating from initial slip band orientations. Each grain boundary will provide resistance against growth. This resistance to crack growth is material dependent and determines the growth rate. Growth becomes continuous when the number of grains along the micro-crack front becomes sufficiently large. The end of the crack initiation phase concludes when the growth of the micro-crack becomes independent of the surface conditions.

After the crack initiation phase there is the crack propagation phase. This phase is not the scope of this dissertation because once cracks become visible, the remaining fatigue life of a laboratory specimen is usually a small percentage of the total life. However, for real structures the crack propagation phase could be a larger percentage. Therefore the quantification of fatigue through the crack initiation phase will be explained now.

To facilitate fatigue there must exist different types of fluctuations or load forms on the structure. The simplest type of load form is constant amplitude loading where the forms are repetitive in time. Each stress cycle will be identical [Pook; 2007]. The loading can be expressed as a stress amplitude,

$$\sigma_a = \frac{\sigma_{max} - \sigma_{min}}{2} \tag{2.87}$$

and/or a mean stress as,

$$\sigma_m = \frac{\sigma_{max} + \sigma_{min}}{2} \tag{2.88}$$

The loading can also be expressed in terms of the stress ratio,

$$R = \frac{\sigma_{min}}{\sigma_{max}} \qquad (2.89)$$

and/or amplitude ratio,

$$A = \frac{\sigma_a}{\sigma_m} \qquad (2.90)$$

The other type of load forms are variable amplitude loading which covers everything that isn't constant amplitude loading [Schijve; 2009]. The simplest form consist of several blocks of continuous amplitude loadings to the most complex; arbitrary non-periodic loading. Variable loading is sometimes broken into narrow band random loading, where the cycles can be distinguished and broad band random loading where the individual cycles can't be distinguished.

To count the cycles independent of the type of loading condition the structure undergoes; the rainflow counting algorithm is commonly used [Matsuishi; 1968]. This method was coined "rainflow" due to its resemblance of rain falling onto a pagoda and running down the edges of the roof. The algorithm is defined as follows,

1. The loading history is rotated, such that the time axis is vertically downward.

2. A flow of rain starts at each successive extremum point.

3. A half cycle is defined by allowing each rainflow to drip down the roof until,

   (a) It falls opposite a larger maximum or smaller minimum point.

   (b) Meets a rainflow falling from above

   (c) It falls indefinitely

4. Each full cycle is counted by pairing the repeated half cycles.

A visual representation of the motivation and application of the algorithm is presented in Fig. 2.9.
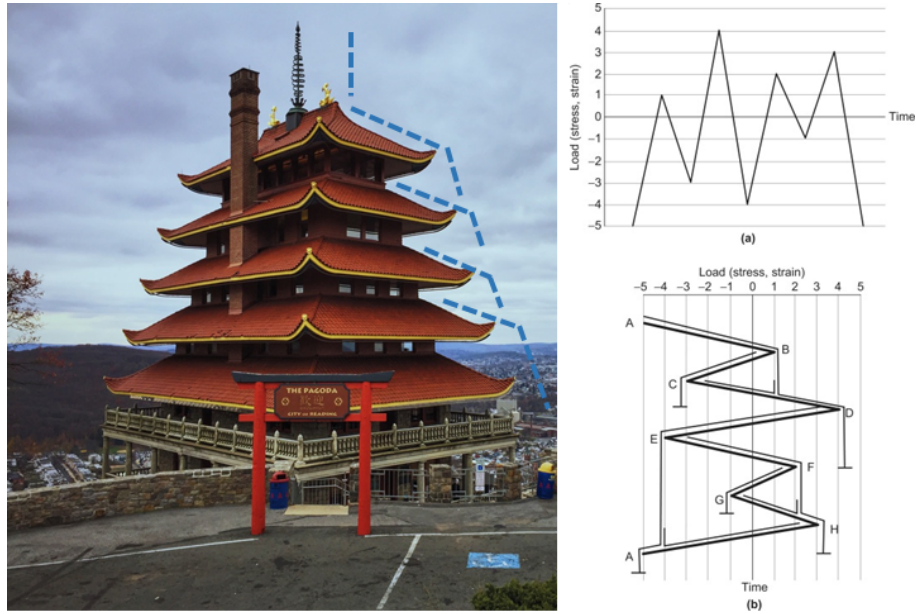
Figure 2.9: The motivation and application of the rainflow algorithm. (a) time history of stress loading (b) the method to count cycles

Once the cycles are counted a cumulative fatigue damage theory can be applied. The fundamental idea behind these theories is that inherent microscopic parameters that govern the accumulation of damage is related to macroscopic quantities such as stress or strain. This dissertation focuses on stress-based approaches for fatigue damage quantification. However, there also exists strain based approaches that use the Coffin-Manson relationship [Coffin; 1954, Manson; 1954], energy based methods that focus on the relationship between hysteretic area and fatigue behavior [Inglis; 1927], or continuum damage mechanics which studies the deterioration of mechanical variables in a thermodynamically consistent contiuum framework [Kachanov; 1958,

Kachanov; 1986].

The stress-based approach was introduced by Wöhler in 1860 with his formulation of the S-N curve. Specimens are loaded at specific cyclic stresses until ultimate failure is reached, at that point the number of cycles, N_f, are recorded. Either the stress range or the stress amplitude is plotted against the number of cycles to failure in order to obtain the S-N curve. For most engineering materials these curves were empirically generated in the 20th century. A generic S-N curve is presented in Fig. 2.10. Note that at the high cycle region there exists asymptotic behavior of the S-N
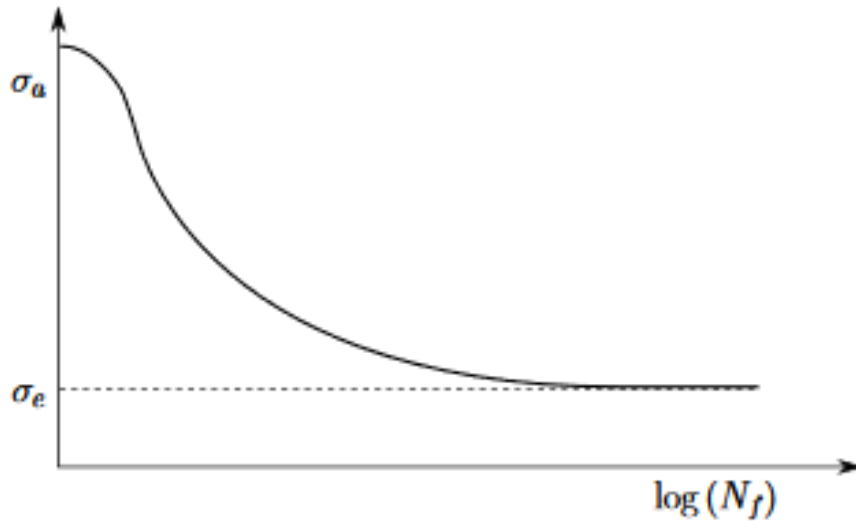
Figure 2.10: The general form of an S-N curve.

curve which is defined as the endurance or fatigue limit. In which specimens loaded with a stress amplitude below this limit will have infinite life. Some materials such as Aluminum have been shown to not have a well defined endurance limit. The S-N curve is numerically quantified by Basquin's equation,

$$\log(N_f) = K - b\log(\sigma_i) \tag{2.91}$$

43

Note that empirical data from cyclic stress fatigue tests determine the parameters that define the curve. Typically, several tests are performed at each stress amplitude which provides a distribution of cycles to failure. This commonly follows a normal distribution about each parameter, yet the mean value is used in the formulation for most S-N curves.

Once the time history of the stresses on the structure are rainflow counted and an S-N curve of the material is formulated one can use the Palmgren-Miner linear damage rule to determine the extent of damage as,

$$D = \sum_{i=1}^{k} r_i = \sum_{i=1}^{k} \frac{n_i}{N_{f,i}} \tag{2.92}$$

where D is the damage index, r_i is the cycle ratio corresponding to each load level $\sigma_{a,i}$, n_i is the estimated or measured number of cycles at stress value $\sigma_{a,i}$, $N_{f,i}$ is the number of cycles til failure at stress value $\sigma_{a,i}$ from the S-N curve. Failure will occur when this damage index approaches 1.

2.2.3 FATIGUE UNCERTAINTY

The accumulation of fatigue damage is a random process. Typically the fatigue material properties can be expressed as a random variable while the applied loading on the structure is a stochastic process [Shen et al.; 2000]. Uncertainty is introduced into the damage index from the the estimated stresses determined by the Kalman filter and the empirical fatigue material properties. The objective of this dissertation is to characterize the variation in the damage index in order to quantify confidence in the fatigue state at any time for any structure in order to determine a stopping

criteria. The stress estimation uncertainty can be expressed as a single-sided Gaussian probability distribution with bounds on the acceptable range of expected damage values per cycle.

$$f(d) = \frac{1}{b}(n_s K)^{(\frac{d}{b})(\frac{1-b}{b})} \frac{1}{\sqrt{2\pi}\sigma_s} e^{-(\frac{((n_s K d)^{\frac{1}{b}} - \mu_s)^2}{2\sigma_s^2})} + \frac{1}{\sqrt{2\pi}\sigma_s} e^{-(\frac{((n_s K d)^{\frac{1}{b}} + \mu_s)^2}{2\sigma_s^2})}$$ (2.93)

where d is the range of possible damages for PDF integration, n_s is the inverse of the number of cycles at each experienced stress, b, K are the empirically determined material-dependent parameters that describe the shape of the S-N curve, σ_s is the standard deviation of the stresses, and μ_s is the mean estimated stresses.

Material fatigue is well understood in a qualitative sense, yet statistical distributions for fatigue parameters are unable to be derived from this physical interpretation [Schijve; 2003]. Therefore a distribution must be assumed, the most common distribution function is the normal distribution which is used here. Other applicable distribution functions are the $\log(N)$-normal distribution, the 3-parameter Weibull distribution, and the $\log(N - N_o)$-normal distribution [Schijve; 2005]. The slope and y-intercept for the S-N curve presented above are assumed to be jointly Gaussian random variables with the following probability density function,

$$y = f(x, \mu, \Sigma) = \frac{1}{\sqrt{|\Sigma|(2\pi)^2}} \exp(-\frac{1}{2}(x - \mu)\Sigma^{-1}(x - \mu)'$$ (2.94)

where μ is the mean vector and Σ is the covariance matrix.

It is essential to include both the uncertainty of the estimated stresses and the uncertainty in the S-N curve fatigue parameters to minimize the risk of material failure prior to maintenance. The associated risk is directly related to the quantification

of uncertainty in both state estimation and material properties. If the uncertainty in the S-N curve parameters are not included the extent of fatigue damage is underestimated which is not representative of real-world applications. This was experimentally validated in Chapter 4.

Two methods are proposed for this framework. Both take advantage of defining the slope and y-intercept of the S-N curve as jointly Gaussian random variables. For method one, Monte-Carlo simulations are performed by realizing S-N curves for the structures life which are used along with the estimated stresses to quantify an estimated index. The uncertainty bounds were then chosen based on the variance in the fatigue indices realized. The downside of this method is that it can't be performed in near-real time, therefore an offline method that can be performed a priori is proposed.

For method two realizations of the slope and y-intercept are realized as correlated Gaussian random variables. Then an ellipse is drawn around the data based on the variance in the semi-major and semi-minor axes. The percent of realizations that fall within the ellipse will define the confidence in the estimate of the material's fatigue parameters. Maxima and minima of the semi-major axis are then chosen as the parameters for the S-N curve that will determine the uncertainty bounds of the estimated damage index. This allows near-real time tracking of the damage index since the estimated stresses are directly used in three probabilistic S-N curves that are defined based on confidence intervals and material properties. The two methods are presented in Fig. 2.11.
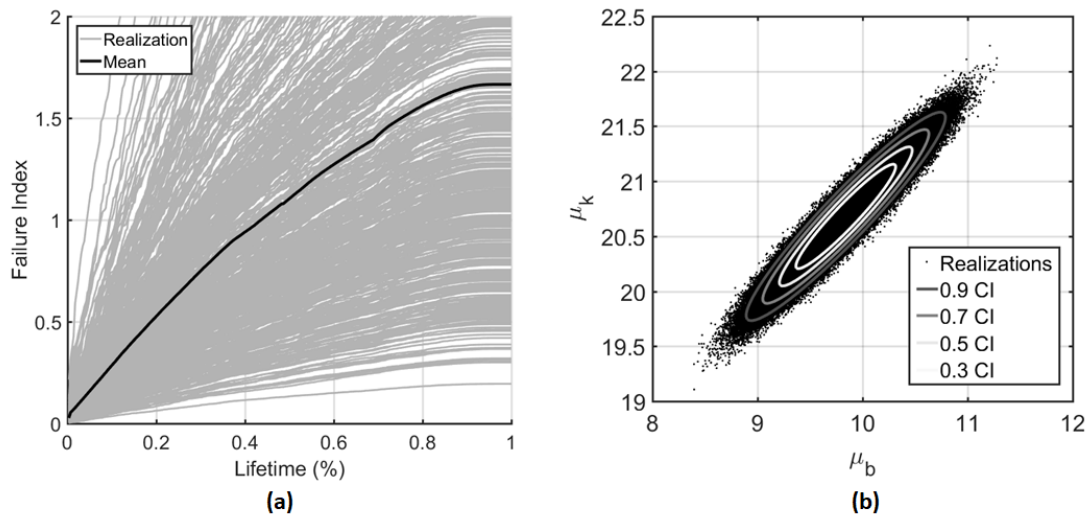
Figure 2.11: (a) Monte-Carlo like method to determine uncertainty in damage index (b) Offline method to determine confidence interval of fatigue material properties of S-N curve.

2.3 STRUCTURAL HEALTH MONITORING

Structural health monitoring (SHM) is the process of formulating a damage identification framework for civil, mechanical, and aerospace structures. The general format for this process consists of detection, localization, classification, assessment and prediction of fatigue damage. Detection will qualitatively indicate present damage in a structure, localization will provide a probable location for damage, classification will determine the type of damage, assessment will provide an estimate of the extent of damage, and prediction will estimate the remaining life of the structure. Most SHM research has been conducted over the last 40 years and has attempted to identify global damage in structures. The interest has been spurred by the potential for significant life-safety and economic benefits through implementation.

Essential to the damage identification framework is the need to define two different

states of the system, namely the current state and an initial, undamaged state. This allows for a meaningful comparison for the state of system degradation. Changes in material and/or geometric properties of the system allow for quantification of damage. This damage is often seen as changes to the system response or mechanical properties.

All damage will begin at the material level, and all materials will have some degree of defect or flaw in its undamaged state unbeknownst to the user. Then when the system is loaded these defects or flaws will grow and coalesce at varying rates to cause local component failure which ultimately leads to system-level damage. In this sense the definition of damage isn't total system failure, but rather that the system can no longer operate in its intended manner. When the damage continues to grow, there will be a point where the system will no longer be able to operate acceptably to the user. This point will be considered system failure.

Damage accumulation is typically defined on two different time scales, relatively long periods and discrete time events. The long periods of damage accumulation are associated with fatigue or corrosion, while discrete events could include nonscheduled events such as earthquakes or scheduled events such as aircraft take-offs.

A successful SHM procedure incorporates three main processes for implementation. This include observations of the mechanical or structural system through sensor measurements, the extraction of damage-sensitive features from the measurements, and then the analysis of these features to quantify the extent of damage through the current state of the system. Much like the two time scales for damage accumulation there exists long-term and discrete time SHM. In terms of long-term SHM the output of the process, damage accumulation, is periodically updated in regards to the structures ability to perform its intended function under its operational environment which

is continually degrading the system. During a discrete event, such as an earthquake, SHM can be used for rapid condition screening and risk assessment. The screening process will provide real-time information about the system integrity during and after the event.

Five closely related disciples are incorporated to completely identify damage in civil, mechanical, and aerospace structures. This includes SHM, condition monitoring (CM), non-destructive evaluation (NDE), statistical process control (SPC) and damage prognosis (DP). SHM provides online-global damage identification of these systems. CM addresses damage identification for rotating machinery such as those used in manufacturing [Bently & Hatch; 2002]. NDE is a local damage identification procedure that is performed off-line after damage has been located. This process is carried out for damage characterization and as a post processing method using a priori knowledge of the damage [Schull; 2002]. SPC uses a variety of sensors to monitor changes in a process rather then the structure, where one cause of the change could result from structural damage [Montgomery; 1997]. DP is performed once damage has been detected and is used to predict the remaining useful life of the system [Farrar & Worden; 2007]. For a review of the technical literature for damage identification refer to [Doebling et al.; 1996, Sohn et al.; 2003].

High fidelity finite element model updating has been proposed by some authors in order to estimate fatigue damage. Specifically, the hypothesis is that as damage accumulates the mechanical characteristics such as natural frequencies, damping ratios, and mode shapes will also change. Giagopoulos et al. have proposed a structural health monitoring framework that incorporates a model updating method as changes are seen in the structural response to provide an estimate of the fatigue pro-

cess [Giagopoulos et al.; 2019]. These changes can be incorporated into a fatigue accumulation framework based on updating the joint conditional probability of the damage estimate as knowledge of the damage sensitive features are evaluated [Gobbato et al.; 2012]. The framework has been proposed and experimentally validated for crack propagation trajectories and shown to improve remaining fatigue life estimates [Gobbato et al.; 2014]. As this dissertation shows, for certain types of systems the model updating approach is only viable once the structure is damaged to a point of imminent failure.

2.3.1 Fatigue Monitoring Framework

Traditionally a fatigue analysis is carried out during the structural design stage of a machine or structure, however, more recently there has been a marked interest in monitoring and prognosis of fatigue damage in existing and operating structures. Several important differences exist between the design and the monitoring/prognosis problem in fatigue. In design the engineer is dealing with a hypothetical, yet unbuilt structure and therefore mechanical properties and boundary conditions can (and must) be assumed. In monitoring, the structure already exists and its mechanical properties can be estimated by processing sensor measurements and non-destructive testing. Furthermore, in the design stage, the structure will begin its operation in a pristine state, while in the monitoring case the current state of the fatigue damage of the structure is highly uncertain.

The traditional practical approach to monitoring fatigue is to carry out a visual inspection, find macroscale cracks and track/predict their evolution; however, in many cases, by the time the cracks grow to a point where they are detectable, the load bear-

ing capacity of the structure has been greatly reduced [Downing; 2012]. A preferable approach is to track fatigue damage on the whole structure prior to the appearance of macroscopic cracks. This would allow for higher levels of reliability, larger lead times and reduced risk. However, since it is not cost effective to use strain sensors at all critical locations of a structure, the essential capability that is required to achieve this objective is tracking stress/strain time history through the whole structure by using global vibration measurements, such as accelerations. One possibility to achieve this capability is via state estimation.

State estimation is a model-data fusion approach that aims to reconstruct the state of a dynamical system, displacements and velocities within a linear model framework, from noisy observations of its response and a model. The state is a set of variables that if known along with the input/excitations at a given time can uniquely describe the future system response. For the purpose of fatigue monitoring the components of the response that are of interest are the internal stress and strain fields of the structural elements which can be derived from displacements, velocities, and accelerations. This is possible when the state is observable. A state is observable if it can be reconstructed from knowledge of the outputs and inputs of the system. Observability is determined by the rank of the observability matrix. The stress at a point will be observable if all the displacements necessary to determine the stress are observable.

Several methods have been proposed and successfully validated to estimate unmeasured response in structural systems [Palanisamy et al.; 2015, Hernandez; 2011, Erazo & Hernandez; 2014]. The Kalman filter is the optimal state estimator in the sense that it minimizes the Euclidean norm of the state error time step of interest. A fundamental assumption of the Kalman filter is that the unmeasured excitations are

51

realizations of a Gaussian random process, this condition is often relaxed; however, a dual-Kalman filter approach can be used to estimate both the state and the unmeasured excitation in order to reduce the state error [Azam et al.; 2015]. By strategically placing sensors it is possible to use minimal sensors to ensure that the states of interest are observable. Minimal sensor instrumentation is desirable due to decreased cost of the sensor network, ease of installation, and decreased maintenance.

From the estimated stress, the evolution of mechanical fatigue can be monitored by using a rainflow cycle counting algorithm and an S-N curve to estimate fatigue damage [Schijve; 2003]. Fatigue accumulation frameworks with minimal instrumentation have been proposed and validated for a subset of the structures serviceable lifetime in both simulation and experimentally [Papadimitriou et al.; 2011]. The Kalman filter has been shown to be an effective tool to estimate the unmeasured response in structural systems. However, the accuracy of the damage accumulation framework throughout the structures serviceable lifetime has yet to be quantified. Many frameworks incorporate the uncertainty in the stress estimation yet use the expected value of the S-N curve parameters which makes them over-confident in the estimated damage index bounds. The true bounds of the damage estimate provide a more realistic interpretation of the fatigue index in near-real time, allowing for remedial action to be performed before macroscopic crack growth and/or component failure. An important challenge that is addressed in this dissertation is quantifying the uncertainty in the damage estimate throughout the structures serviceable life by tracking stress cycles.

REFERENCES

[Albert; 1837] Albert, WAJ. (1837). Uber Treibseile am Harz. Archiv fur Mineralogie, Georgnosie *Bergbau und Huttenkunde.* 10:215-234.

[Azam et al.; 2015] Azam, SR. Chatzi, E. Papadimitriou, C. (2015). A dual kalman filter approach for state estimation via output-only acceleration measurements. *Mechanical Systems and Signal Processing.* 60(61):866-886.

[Basquin; 1910] Basquin, OH. (1910). The exponential law of endurance tests. *Proc. Annual Meeting, American Society for Testing Materials.* 10:625-630.

[Bently & Hatch; 2002] Bently, DE. Hatch, CT. (2002). *Fundamentals of rotating machinery diagnostics.* ASME Press: New York,NY.

[Braithwaite; 1854] Braithwaite, F. (1854). On the fatigue and consequent fractures of metals. *Institution of Civil Engineers, Minutes of Proceedings.* Vol. XIII:463-474.

[Chen & Xu; 2016] Chen, X. Xu, JZ. (2016). Structural failure analysis of wind turbines impacted by super typhoon Usagi. *Engineering Failure Analysis.* 60:391-404.

[Coffin; 1954] Coffin, LF. (1954). A study of the effects of cyclic thermal stresses on a ductile metal. *Transactions of the American Society of Mechanical Engineers.* 76:931-950.

[Cui; 2002] Cui, W. (2002). A state-of-the-art review on fatigue life prediction methods for metal structures *Journal of Marine Science and Technology.* 7(1):43-56.

[Doebling et al.; 1996] Doebling, SW. Farrar, CR. Prime, MB. Shevitz, DW. (1996).*Damage identification and health monitoring of structural and mechanical systems from changes in their vibration characteristics: a literature review.* Los Alamos National Laboratory Report LA-13070-MS.

[Doebling et al.; 1998] Doebling, S. Farrar, C. Prime, MB. (1998). A summary review of vibration-based damage identification methods. *Shock and Vibration Digest.* 30(2):91-105.

[Downing; 2012] Downing, NE. (2012). *Mechanical behavior of materials: engineering methods for deformation, fracture, and fatigue.* 4th ed. Pearson: Boston, MA.

[Erazo & Hernandez; 2014] Erazo, K. Hernandez, EM. (2014). A model-based observer for state and stress estimation in structural and mechanical systems: Experimental validation. *Mechanical Systems and Signal Processing.* 43(1):141-152.

[Farrar et al.; 2001] Farrar, C. Doebling, S. Nix, D. (2001). Vibration-based structural damage identification. *Philosophical Transaction of the Royal Society.* 359:131-149.

[Farrar & Lieven; 2002] Farrar, CR. Lieven, NAJ. (2002). Damage prognosis: the future of structural health monitoring. *Phil. Trans. R. Soc. A.* 365:623-632.

[Farrar & Worden; 2007] Farrar, CR. Worden, K. (2007). An introduction to structural health monitoring. *Philos Trans A Math Phys Eng Sci.* 365(1851):303-315.

[Gelb; 1996] Gelb, A. (1996). *Applied Optimal Estimation..* 14 MIT Press: Cambridge, MA.

[Giagopoulos et al.; 2019] Giagopoulos, D. Arailopoulos, A. Dertimanis, V. Papadimitriou, C. Chatzi, E. Grompanopoulos K. (2019). Structural health monitoring and fatigue damage estimation using vibration measurements and finite element model updating. *Structural Health Monitoring* . 18(4):1189-1206.

[Gobbato et al.; 2012] Gobbato, M. Conte, JP. Kosmatka, JB. Farrar CR.(2012). A reliability-based framework for fatigue damage prognosis of composite aircraft structures. *Probabilistic Engineering Mechanics.* 29:176-188.

[Gobbato et al.; 2014] Gobbato, M. Kosmatka, JB. Conte JP. (2014). A recursive bayesian approach for fatigue damage prognosis: An experimental validation at the reliability component level. *Mechanical Systems and Signal Processing.* 45(2):448-467.

[Hao; 2010] Hao, S. (2010). I-35W bridge collapse. *Journal of Bridge Engineering.* 15(5):608-614.

[Hernandez; 2011] Hernandez, EM. (2011). A natural observer for optimal state estimation in second order linear structural systems. *Mechanical Systems and Signal Processing.* 25(8):2938-2947.

[Inaudi & Deblois; 2009] Inaudi, D. Deblois, R. (2009). Overview of 40 bridge structural health monitoring projects. *26th International Bridge Conference.* Pennsylvania, PA.

[Inglis; 1927] Inglis, NP. (1927). Hysteresis and fatigue of Wohler rotating cantilever specimen. *The Metallurgist.* 23-27.

[Inman et al.; 2005] Inman, D. Farrar, C. Lopes, V. (2005). *Damage Prognosis: For Aerospace, Civil and Mechanical Systems.* New York: Wiley.

[Jazwinski; 1970] Jazwinski, AH. (1970). *Stochastic Processes and Filtering Theory.* Academic Press: New York, NY.

[Julier & Uhlmann; 1997] Julier, SJ. Uhlmann, JK. (1997). A new extension of the kalman filter to nonlinear systems. *Proc. of AeroSense: The 11th Int. Symp. on Aerospace/Defense Sensing, Simulation and Controls.*

[Kachanov; 1958] Kachanov, LM. (1958). In time to rupture in creep conditions. *Izviestia Akademii Nauk SSSR, Otdelenie Tekhnicheskikh Nauk .* 8:26-31.

[Kachanov; 1986] Kachanov, LM. (1986). *Introduction to continuum damage mechanics. Mechanics of Elastic Stability.* Netherlands: Springer.

[Kalman; 1960] Kalman, RE. (1960). A new approach to linear filtering and prediction problems. *Transaction of the ASME. Series D, Journal of Basic Engineering.* 82(1):35-45.

[Manson; 1954] Manson, SS. (1954). Behavior of materials under conditions of thermal stress. *Technical Report, National Advisory Commission on Aeronautics: report 1170.* Cleveland: Lewis Flight Propulsion Laboratory.

[Matsuishi; 1968] Matsuishi, M. Endo, T. (1968). Fatigue of metals subjected to varying stress. *Journal of Basic Engineering.*

[Miner; 1945] Miner, MA. (1945). Cumulative damage in fatigue. *Trans. ASME J. appl. Mech,.* 59:A160-A162.

[Montgomery; 1997] Montgomery, DC. (1997). *Introduction to statistical quality control.* John Wiley & Sons Inc: New York, NY.

[Morin; 1853] Morin, A. (1853). Lecons de mecanique practique-resistance des materiaux. *Paris, Librairie de L. Hachette et Cie.* p.456.

[NTSB; 2007] National Transportation Safety Board. (2007). Collapse of I-35W Highway Bridge Minneapolis, Minnesota. *Accident Report.* NTSB/HAR-08/03:PB2008-916203.

[Ottosen et al.; 2008] Ottosen, NS. Stenstrom, R. Ristinmaa, M. (2008). Continuum approach to high-cycle fatigue modeling. *International Journal of Fatigue.* 30(6):996-1006.

[Palanisamy et al.; 2015] Palanisamy, R. Cho, S. Kim, H. Sim, SH. (2015). Experimental validation of Kalman filter-based strain estimation in structures subjected to non-zero mean input. *Smart Structures and Systems.* 15(2), 489-503.

[Palmgren; 1924] Palmgren, A. (1924). Die Lebensdauer von Kugellagern. *VDI-Zeitschrift.* 68:339-341.

[Papadimitriou et al.; 2011] Papadimitriou, C. Fritzen, CP. Kraemer, P. Ntotsios, E. (2011). Fatigue predictions in entire body of metallic structures from a limited number of vibration sensors using kalman filtering. *Structural Control and Health Monitoring.* 18(5):554-573.

[Pook; 2007] Pook, LP. (2007). *Metal Fatigue: What It Is, Why It Matters. Solid Mechanics and Its Applications.* Netherlands: Springer.

[Rankine; 1842] Rankine, WJM. (1842). On the causes of the unexpected breakage of the journals of railway axles, and on the means of preventing such accidents by observing the law of continuity in their construction. *Institution of Civil Engineers, Minutes of Proceedings.* 2:105-108.

[Ribeiro; 2004] Ribeiro, MI. (2004) Kalman and extended Kalman filters: concept, derivation and properties. *Technical report.* Institute for Systems and Robotics.

[Schijve; 2003] Schijve, J. (2003). Fatigue of structures and materials in the 20th century and the state of the art. *International Journal of Fatigue.* 25(8):679-702.

[Schijve; 2005] Schijve, J. (2005). Statistical distribution functions and fatigue of structures. *International Journal of Fatigue.* 27:1031-1039.

[Schijve; 2008] Schijve, J. (2008). *Fatigue of Structures and Materials.* Netherlands: Springer.

[Schijve; 2009] Schijve, J. (2009). Fatigue under variable-amplitude loading. *Fatigue of Structures and Materials.* 295-328. Netherlands: Springer.

[Schull; 2002] Shull, P. (2002). *Nondestructive evaluation theory, techniques, and applications.* Marcel Dekker, Inc: New York, NY.

[Schutz; 1996] Schutz, W. (1996). A history of fatigue. *Engineering Fracture Mechanics.* 54(2):263-300.

[Shen et al.; 2000] Shen, HJ. Lin, J. Mu, E. (2000). Probabilistic model on stochastic fatigue damage. *International Journal of Fatigue.* 22:569-572.

[Simon; 2006] Simon, D. (2006). *Optimal State Estimation..* New York: Wiley.

[Sobczyk; 1992] Sobczyk, K. Spencer, BF. (1992). *Random Fatigue: From Data to Theory.* Academic Press.

[Sohn et al.; 2003] Sohn, H. Farrar, CR. Hemez, FM. Czarnecki, JJ. Shunk, DD. Stinemates, DW. Nadler, BR. (2003). *A review of structural health monitoring literature: 1996-2001.* Los Alamos National Laboratory Report LA-13976-MS.

[Stephens et al.; 2000] Stephens, RI. Fatemi, A. Stephens, RR. Fuchs, HO. (2000). *Metal Fatigue in Engineering.* New York: Wiley, 2.

[Suresh; 2001] Suresh, S. (2001). *Fatigue of materials.* Cambridge: Cambridge University Press

[USDOH; 2010] U.S. Department of Homeland Security, S. and Technology. (2010). Aging infrastructure: Issues, research, and technology. *Building and Infrastructure Protection Series.*

[van Gent et al.; 2007] van Gent, RN. Siem, D. van Middelkoop, M. (2007). Incidence and determinants of lower extremity running injuries in long distance runners: a systematic review. *British Journal of Sports Medicine.* 41:469-480.

[Wan & Van Der Merwe; 2000] Wan, EA. Van Der Merwe, R. (2000). The unscented kalman filter for nonlinear estimation. *Proc. of IEEE Symposium 2000.* Lake Louise, Oct 2000.

[Wohler; 1867] Wohler's experiments on the strength of metals. (1867). *Engineering.* 4:160-161.

CHAPTER 3

FATIGUE USAGE MONITORING IN 5MW SIMULATED WIND TURBINE USING SPARSE VIBRATION MEASUREMENTS: COMPARATIVE STUDY

3.1 ABSTRACT

As wind turbine design technology remains an industry focus the size and flexibility of wind turbines continues to increase. This has resulted in the viability of offshore wind farms making maintenance and repair operations more difficult and costly. One consequence of the increased size and harsh operational environment is the potential for fatigue failure of structural components. The development of structural health monitoring systems capable of tracking fatigue damage is desirable. This type of sys-

tem can be coupled with control mechanisms to simultaneously maximize generation
and minimize operational loads which lead to fatigue damage. Various researchers
have proposed the use of vibration measurements to monitor stresses and fatigue
damage in the tower and blades of turbines. This paper compares three methods
to estimate loads and stresses (and their associated uncertainty) in the tower of the
National Renewable Energy Laboratory's (NREL) 5 MW reference turbine subjected
to turbulent wind. Simulations are carried out using NREL's high-fidelity FAST soft-
ware. The methods are compared under a 20 different operating conditions, which
include varying wind speeds and pitch angles.

3.2 INTRODUCTION

As the United States and the rest of the world set renewable energy pathways for
energy electrification, the investment into wind energy technology becomes neces-
sary. The blades of wind turbines have continued to be the target for technological
improvement resulting in larger wind turbines in more remote locations [Veers et al.;
2003]. The change in size and environmental conditions leads to challenging main-
tenance and repair operations. Not only does this increase the maintenance cost for
wind farm operators, it also increases the fatigue loading on structural components
of the wind turbine system, thus reducing service life. It is therefore desirable to
develop structural health monitoring (SHM) systems that are capable of tracking fa-
tigue damage in susceptible areas and/or components to increase the reliability of
the entire system. In addition SHM systems can be coupled with control mechanisms
to simultaneously maximize generation and minimize operational loads resulting in a

significant increase in the expected component lifetime [Hammerum et al.; 2007].

An SHM framework is necessary when operation and maintenance costs can account for 20%-30% of the levelized cost of electricity (LCOE) averaged across the lifetime of a wind turbine [Blanco; 2009]. Documented cases of wind turbine accidents since the 1980s show that approximately 35% result from some type of structural failure [CWIF; 2016]. Structural failures include damage to the tower, nacelle, blades, and/or bolts. The anchor bolts have been shown to be the dominant load carrying failure mode of the tower-foundation system due to poor quality and insufficient strength [Fujiyam et al.; 2014, Chou & Tu; 2011].

SHM systems for wind turbines typically use localized methods to detect damage in structural components [Ciang et al.; 2008, Wymore et al.; 2015]. These methods include visual inspection, digital image correlation, acoustic emission, etc. Due to their localized nature, finding damage can be time consuming and in some cases not practical. The alternative is to use global response measurements, yet these practices tend to have low sensitivity to localized damage. Therefore it is desirable to have a method that uses global response of the system to estimate local quantities related to damage. In this paper we propose the use of global measurements to estimate stresses in critical locations and connections.

In order to place the current work in context we briefly summarize recent work on the use of vibration measurements to perform damage diagnosis. Soman et al. [Soman et al.; 2016] used a discrete Kalman Filter along with several Fibre Bragg grating based strain sensors to determine the neutral axis position of the DTU 10 MW reference wind turbine tower. The bi-axial tracking of the neutral axis was performed in a simulated environment with sensor pairs at various tower heights. The study was

performed to determine and validate the efficacy of using the neutral axis to quantify damage in the presence of measurement noise.

Benedetti et al. [Benedetti et al.; 2013] used strain measurements from an operating two-bladed mini wind turbine (11 kW) to observe the onset of fatigue cracks in real-time monitoring. They provide experimental characterization of the operating turbine and then recreate the turbine in a simulated environment to determine the strain sensitivity of a damaged tower. By using the strain difference between adjacent strain sensors they were able to detect the presence of a crack, however the detection algorithm is limited by the number of sensors and their location. Tibaldi et al. [Tibaldi et al.; 2016] used a high fidelity linear model of the 5 MW reference turbine in the HAWC2 simulated environment to evaluate wind turbine fatigue loads. A spectral method is used to compute the fatigue loads from the power spectral density of the response at selected sensor locations. Three load evaluation cases were examined which included the normal operation full wind speed range, two different controller tunings, and three different wind speeds with variable turbulence seeds.

Recently there has been a focus on automated operational modal analysis (OMA) for SHM of wind turbine support structures. OMA identifies resonance frequencies, mode shapes, and damping parameters in near real time from acceleration data, namely SCADA data and acceleration signals as input. OMA is attractive due to its ability to estimate fatigue in unmeasured locations from minimal easily measured locations. Shirzadeh et al. [Shirzadeh et al.; 2015] used OMA to compare dynamic properties of a 3 MW Vestas wind turbine instrumented with 10 accelerometers in the field and in a simulated environment, HAWC2, showing good agreement. Weijtjens et al. [Weijtjens et al.; 2016] has performed a full scale test study of a 3 MW Vestas

wind turbine instrumented with six accelerometers. Two years of continuous data was processed using a case-by-case strategy to determine changes in modal parameters, they determined an increased stiffness of the turbine tower. Similarily, Iliopoulos et al. [Iliopoulos et al.; 2015] identified modal parameters of a 3 MW Vestas wind turbine with 10 sensors through OMA. A numerical FE model was created in ANSYS to estimate accelerations, stresses and strains at unmeasured locations. Several studies have shown the efficacy of OMA for variable wind turbine sizes, locations and quantity of sensors [Iliopoulos et al.; 2014, Iliopoulos et al.; 2016, Pacheco et al.; 2017, Tewolde et al.; 2017, Weijtjens et al.; 2017].

Tatsis et al. [Tatsis et al.; 2017] used minimal output only measurements in combination with an augmented Kalman filter to estimate fatigue damage accumulation at the support structure of the 5 MW reference turbine within FAST. The estimated states are combined with an FE model of the substructure to quantify the stress which is propagated through a fatigue model to identify the accumulated damage.

This paper compares the accuracy of three popular algorithms for dynamic response estimation, namely a model-based observer (MBO), the Kalman filter (KF) and modal interpolation (MI). Each algorithm makes specific assumptions that are never fully satisfied in practice. In the context of wind turbine structures some of these assumptions manifest themselves in the characterization of the unmeasured wind excitations, the model simplifications and measurement noise. In a realistic environment it is not possible to control all the conditions separately, therefore in this paper we resort to simulations in order to compare the various methods under 20 different operating conditions.

The MBO was originally derived by Hernandez [Hernandez; 2011, Hernandez;

2013] and was subsequently validated in the lab by Erazo [Erazo & Hernandez; 2014]. It explicitly accounts for spatial correlation and the statistical properties of the excitation through knowledge of the underlying power spectral density of the wind loads. The KF is the optimal state estimator in the sense that it minimizes the Euclidian norm of the estimation error [Kalman; 1960]. However, there is significant temporal and spatial correlation in the loading for wind turbines. The KF has been used for real-time parameter estimation under wind loading yet it is not evident that the KF provides an accurate estimation of the state for cumulative fatigue loading models [Hernandez et al.; 2013]. The MI method makes use of low order mode shapes along with noise contaminated sensor measurements to estimate the dynamic response of the wind turbine structure.

Each method is used to estimate loads and stresses (and their associated uncertainty) throughout the tower and bolted connections of the NREL 5 MW reference turbine subjected to turbulent wind. The comparative study is implemented in a simulated environment where the system is a FAST model of the turbine, the turbulent wind field is generated using TurbSim, and the estimator is formulated using a simplified finite element model of the tower [Jonkman & Buhl; 2005, Jonkman et al.; 2009, Jonkman & Buhl; 2005b].

The paper is organized as follows, it begins with a section that provides a description of the assumed system model followed by a section with a description of the wind load model. The introductory sections are followed by sections that describe the modal interpolation method, the standard KF formulation and the MBO. The final section presents the simulation results along with a thorough comparison between the MBO, the KF and the MI estimates which concludes the paper.

3.3 System Model and Measurements

We restrict our attention to wind turbine structures whose dynamic response to turbulent wind loads can be simulated as a linear system of the form

$$\mathbf{M}\ddot{q}(t) + \mathbf{C_D}\dot{q}(t) + \mathbf{K}q(t) = \mathbf{b_2}f(t) \tag{3.1}$$

where $q(t) \in \mathbf{R}^{nx1}$ is the displacement vector at time t, $\mathbf{M}$ is the mass matrix, $\mathbf{C_D}$ is the damping matrix, and $\mathbf{K}$ is the stiffness matrix. The forcing function vector is $f(t) \in \mathbf{R}^{nx1}$, and $\mathbf{b_2} \in \mathbf{R}^{nxn}$ is the force distribution matrix.

Throughout the paper measurements of the structural response will be given by velocities defined by

$$y(t) = [0 \quad \mathbf{c_2}]x(t) + v(t) \tag{3.2}$$

where $\mathbf{c_2} \in \mathbf{R}^{mxn}$ maps the degrees of freedom to the measurements and $v(t)$ $\in \mathbf{R}^{mx1}$ is the measurement noise. Velocities can be readily obtained from acceleration measurements using a variety of filtering techniques.

3.4 Wind Load Model

In the absence of vortex shedding or aeroelastic effects the wind-induced force on a discretized section of a slender structure at height z, and time t can be characterized

in quasi-steady form below

$$F(z,t) = \frac{1}{2}\rho \mathbf{C_d}(z)\mathbf{A_t}(z)\mathbf{V}(z,t)^2 = \frac{1}{2}\rho \mathbf{C_d}(z)\mathbf{A_t}(z)(\mathbf{U}(z) + \mathbf{u}(z,t))^2 \qquad (3.3)$$

where $\mathbf{u}(z,t)$ is the time-varying along-wind turbulence component of the wind at height z at time t and $\mathbf{U}(z)$ is the along-wind mean wind speed at height z. The parameters ρ, $\mathbf{C_d}$, and $\mathbf{A_t}$ are the air density, the drag coefficient at height z, and the projected area of contact at height z respectively. The equation above represents a partially correlated non-white random excitation in a one-dimensional frame neglecting transverse wind force and torsional moment effects.

The time varying component, $\mathbf{u}(z,t)$, is generally simulated as a realization of a stationary random process characterized by its PSD, defined as

$$\mathbf{S}(n) = \int_{-\infty}^{\infty} \mathbf{e}^{(-2\pi n)i\tau}\mathbf{R}(\tau)\mathrm{d}\tau \qquad (3.4)$$

where n is the frequency in Hz and $\mathbf{R}(\tau)$ is the autocorrelation function of the real-valued process $h(t)$, expressed as

$$\mathbf{R}(\tau) = \lim_{T \to \infty} \frac{1}{T} \int_{-T/2}^{T/2} h(t)h(t + \tau)\mathrm{d}t \qquad (3.5)$$

Parseval's equality gives a physical interpretation of the PSD,

$$\mathbf{P} = \int_{-\infty}^{\infty} |f(t)|^2 \mathrm{d}t = \frac{1}{2\pi} \int_{-\infty}^{\infty} S(n)\mathrm{d}n \qquad (3.6)$$

The time varying along-wind turbulence component is generated using the software TurbSim, which simulates a full-field turbulent wind time series by using a

66

statistical model with the underlying assumption that the wind velocity is a stationary random process [Jonkman & Buhl; 2005, Jonkman et al.; 2009, Jonkman & Buhl; 2005b].

A common model to describe the time-varying component of the wind turbulence is the IEC Kaimal spectrum [Jonkman & Buhl; 2005b] expressed in the frequency domain by

$$S_{uu}(n) = \frac{\frac{4\sigma_u^2(5.67*min(60m,HubHt))}{\bar{u}_{hub}}}{(1 + \frac{6*n*(5.67*min(60m,HubHt))}{\bar{u}_{hub}})^{5/3}} \tag{3.7}$$

where $S_{uu}(n)$ is the value of the spectrum at frequency n, σ_u is the standard deviation of the wind velocity, $\bar{u}_{hub}$ is the mean velocity at hub height, $min(x,y)$ indicates the minimum of x and y, and $HubHt$ is the height of the hub (90m for the turbine considered in this paper). A reference height wind speed is necessary to generate the scalar values for the mean speeds at points i, j.

The coherence function between two points, i and j, spatially separated on a grid is defined as

$$C_{i,j}(n) = \exp\left[-a\sqrt{(\frac{n*\Delta}{\bar{u}_{hub}})^2 + (0.12\frac{\Delta}{L_c})^2} \right] \tag{3.8}$$

where a is the coherence decrement (8.8), Δ is the distance between points i and j on the grid, and L_c is the coherence scale parameter defined as

$$L_c = 2.45min(30m, HubHt) \tag{3.9}$$

3.5 RESPONSE ESTIMATION

This section presents a brief description of the fundamental theory behind the three response estimation algorithms to be compared in this paper. Namely, modal interpolation, the Kalman filter and the model-based observer. All three algorithms make certain simplifying assumptions and it is not clear from the onset how these assumptions propagate to the estimation errors. Another important aspect to be considered is variance estimation. It is important to determine which algorithm can provide error bounds that are consistent with the actual estimation errors.

An essential module of the proposed fatigue usage monitoring framework is state estimation. State estimation aims to reconstruct the dynamic response of a dynamical system from measurements of noise contaminated measurements and a model. An observer is a dynamical system driven by the measurements and whose state is an estimate of the original system of interest. In the case of a linear second order structural system, the state vector corresponds to the displacement and velocity of all degrees of freedom.

3.5.1 MODAL INTERPOLATION

The objective in modal interpolation is to estimate the response at all degrees of freedom based on the measured response at some degrees of freedom. The modal interpolation (MI) estimate is given by

$$\mathbf{Y}_m(t) = \Phi_m z(t) \tag{3.10}$$

where $\mathbf{Y}_m(t)$ is the time history response at all degrees of freedom of the system model. Φ_m is a selected modal subset, and $z(t)$ is the time history response of each modal coordinate.

The estimation is carried out using mode shapes as the interpolation function. Thus, denoting $y(t)$ as the measurement at time t, the estimated modal response is

$$z(t) = \Phi_{m,m}^{-1} y(t) \tag{3.11}$$

where $\Phi_{m,m}$ is a matrix of modal coordinates that correspond to the rows at the measured degrees of freedom. For a unique solution $\Phi_{m,m}$ must be invertible (i.e. number of measurements greater than or equal to the number of interpolating mode shapes). Modal interpolation has been used successfully by [Baqersad et al.; 2015] for dynamic response estimation in wind turbine structures. the variance in the estimated modal response is given by

$$\mathrm{var}[z(t)] = \left(\frac{\Phi_m}{\Phi_{m,s}}\right)^2 \mathrm{var}[v(t)] \tag{3.12}$$

where $\Phi_{m,s}$ is the modal coordinate at the sensor location.

3.5.2 KALMAN FILTER

The Kalman filter [Kalman; 1960] is a recursive estimation algorithm that uses a weighted difference between model predictions and measurements to correct the state estimate of a dynamical system $\hat{x}_{k+1}^{(-)}$ at time $t = (k+1)\Delta t$, where $k = 1, 2, \ldots$

$$\hat{x}_{k+1}^{(+)} = \hat{x}_{k+1}^{(-)} + \mathbf{K}_{k+1}\left(y_{k+1} - \mathbf{C}\hat{x}_{k+1}^{(-)}\right) \tag{3.13}$$

69

where $\hat{x}_{k+1}^{(+)}$ is the corrected (a posteriori) state estimate and $\hat{x}_{k+1}^{(-)}$ is the a priori state estimate computed for this system as,

$$\hat{x}_{k+1}^{(-)} = \mathbf{A}\hat{x}_k^{(+)} \tag{3.14}$$

$\mathbf{A}$ is the state transition matrix, defined as

$$\mathbf{A} = e^{\mathbf{F}\Delta t} \tag{3.15}$$

where $\mathbf{F}$ is a matrix of the form

$$\mathbf{F} = \begin{bmatrix} 0 & \mathbf{I} \\ -\mathbf{M}^{-1}\mathbf{K} & -\mathbf{M}^{-1}\mathbf{C_D} \end{bmatrix} \tag{3.16}$$

The recursion method used will be briefly presented here, for a more detailed derivation of the gain refer to [Simon; 2006, Gelb; 1996]. First consider $\mathbf{P}_{k+1}^{(-)}$, the priori state error covariance matrix at time $t = (k+1)\Delta t$, expressed in the following form

$$E[(x_{k+1} - \hat{x}_{k+1})^T(x_{k+1} - \hat{x}_{k+1})] = \mathbf{P}_{k+1}^{(-)} = \mathbf{A}\mathbf{P}_k^{(+)}\mathbf{A}^T + \mathbf{Q}_k \tag{3.17}$$

where $\mathbf{Q}_k$ is the covariance matrix of the unmeasured excitation and $\mathbf{P}_k^{(+)}$ is the posteriori state error covariance at the previous time step. The Kalman feedback gain matrix, $\mathbf{K}_{k+1}$ at time $t = (k+1)\Delta t$, is expressed as

$$\mathbf{K}_{k+1} = \mathbf{P}_{k+1}^{(-)}\mathbf{C}^T\left(\mathbf{C}\mathbf{P}_{k+1}^{(-)}\mathbf{C}^T + \mathbf{R}_{k+1}\right)^{-1} \tag{3.18}$$

and the a posteriori state error covariance matrix is given by

$$\mathbf{P}_{k+1}^{(+)} = (\mathbf{I} - \mathbf{K}_{k+1}\mathbf{C})\mathbf{P}_{k+1}^{(-)} \tag{3.19}$$

3.5.3 MODEL BASED OBSERVER

Lastly this paper considers the use of a Model-based observer (MBO) to perform state estimation. This estimator was originally derived by Hernandez in [Hernandez; 2011]. The MBO can be written in second order form as

$$\mathbf{M}\ddot{\hat{q}}(t) + (\mathbf{C_D} + c_2^T\mathbf{E}c_2)\dot{\hat{q}}(t) + \mathbf{K}\hat{q} = c_2^T\mathbf{E}y(t) \tag{3.20}$$

As can be seen, the estimator modifies the original system by adding viscous dampers and corrective forces at the measurement locations. The corrective forces are linear combinations of the velocity at those points and proportional to the added dampers (see fig. 3.1). The matrix $\mathbf{E}$ in the above equation is diagonal and contains the added viscous damping constants in the diagonal. The matrix $\mathbf{E}$ is selected such that it minimizes the trace of the state error covariance matrix.

The state error, defined as $e = q - \hat{q}$ is given by

$$\mathbf{M}\ddot{e}(t) + (\mathbf{C_D} + c_2^T\mathbf{E}c_2)\dot{e}(t) + \mathbf{K}e(t) = \mathbf{b_2}f(t) - c_2^T\mathbf{E}v(t) \tag{3.21}$$

where the value of $\mathbf{E}$ needs to be determined. Note that the matrix $\mathbf{E}$ is found on both sides of the equation, therefore an optimal balance needs to be reached between the effective damping of the estimator and estimation error that is proportional to

71

the measurement noise.

By taking Fourier transform of both sides of the state error equation

$$(-\mathbf{M}\omega^2 + (\mathbf{C_D} + \mathbf{c_2^T}\mathbf{E}\mathbf{c_2})i\omega + \mathbf{K})e(\omega) = \mathbf{b_2}f(\omega) - \mathbf{c}_2^T\mathbf{E}v(\omega) \qquad (3.22)$$

and defining

$$\mathbf{G}(\omega) = -\mathbf{M}\omega^2 + \mathbf{C_D}i\omega + \mathbf{K} \qquad (3.23)$$

and

$$\mathbf{H}_o(\omega) = (\mathbf{G}(\omega) + \mathbf{c}_2^T\mathbf{E}\mathbf{c}_2 i\omega)^{-1} \qquad (3.24)$$

The frequency domain expression for the state error estimate is given by

$$e(\omega) = \mathbf{H}_o(\omega)(\mathbf{b_2}f(\omega) - \mathbf{c}_2^T\mathbf{E}v(\omega)) \qquad (3.25)$$

If measurement noise and unmeasured excitation are uncorrelated, then the spectral density matrix of the state error, $\mathbf{S_{ee}}(\omega)$, can be expressed as

$$\mathbf{S_{ee}}(\omega) = \mathbf{H_o}(\omega)\mathbf{b_2}\mathbf{S_{ff}}(\omega)\mathbf{b_2^T}\mathbf{H_o^*}(\omega)$$
$$+ \mathbf{H_o}(\omega)\mathbf{b_2^*}\mathbf{S_{vv}}(\omega)\mathbf{b_2^{*T}}\mathbf{H_o^*}(\omega)$$
$$+ \mathbf{H_o}(\omega)c_2^T\mathbf{E}\mathbf{S_{nn}}(\omega)\mathbf{E^T}c_2\mathbf{H_o^*}(\omega) \quad (3.26)$$

where $\mathbf{S_{ff}}(\omega)$ is the spectral density matrix of the wind load acting on the turbine tower,

$$\mathbf{S}_{ff}(z) = (\rho C_d(z)A_t(z)U(z))^2\mathbf{S}_{uu}(z) \qquad (3.27)$$

$\mathbf{S_{vv}}(\omega)$ is the spectral density matrix of the lateral loading at the connection between the turbine nacelle and the tower, $\mathbf{S_{nn}}(\omega)$ is the spectral density of the measurement noise.

We can now express the covariance matrix of the state error as

$$\mathbf{P} = \int_{-\infty}^{+\infty} \mathbf{S_{ee}} \ d\omega \tag{3.28}$$

The objective function for the optimization process is to select the diagonal of $\mathbf{E}$ such that

$$\frac{\partial}{\partial \mathbf{E}} tr(\mathbf{P}) = \frac{\partial}{\partial \mathbf{E}} \mathbf{J}_1 = 0 \tag{3.29}$$

The objective functions used in the derivation of the KF and the MBO are similar in that the state error covariance is minimized. However in the MBO only the displacement section of the state error covariance is minimized while the KF minimizes the full state error covariance. Another important difference is that the KF operates in the time domain, while the MBO operates in the frequency domain. This makes a difference whenever the characterization of the unknown excitation is considered. In most wind turbine applications the excitations are characterized in the frequency domain by their power spectral density.

Numerical optimization is required to define the optimal matrix $\mathbf{E}$ for the general multivariable case, due to there being no analytic closed-form solution as of now. The minimization of the diagonal of $\mathbf{E}$ will yield acceptable results therefore the minimization procedure is not numerically expensive since the problem is reduced from $(m^2 + m)/2$ to m independent values to uniquely define $\mathbf{E}$. Physically this means that the new system will only add grounded and corrective forces proportional

to the measurements and will not add interconnecting dampers. Therefore the matrix **E** will be a diagonal matrix.

3.5.4 FATIGUE DAMAGE

To evaluate the fatigue damage at any location along the height of the wind turbine tower, the Palmgren-Miner linear accumulation rule is used [Miner; 1945]. The damage at a point is quantified as the sum of the ratios of the number of operational cycles to the number of failure cycles at each experienced stress level. Expressed as

$$\mathbf{D} = \sum_i D_i = \sum_i \frac{n(\sigma_i)}{N_f(\sigma_i)} \tag{3.30}$$

where $n(\sigma_i)$ is the number of cycles at stress level σ_i and $N_f(\sigma_i)$ is the number of cycles to failure at the same stress level. The stress time history provided by measurements or determined through state estimation are used in combination with the rainflow counting algorithm to supply the number of cycles at each stress level. To determine the number of cycles to failure at the same stress level an experimentally obtained SN curve is used. An SN curve is defined by

$$N_f = A\sigma_i^{-b} \tag{3.31}$$

where A and b are material-dependent parameters that determine the shape of the curve.

3.6　Simulation Results

This section presents the numerical results of the MBO, KF, and MI methods compared against simulated results from FAST. The simulated system is the tower of the 5 MW reference turbine designed by Jonkman [Jonkman et al.; 2009], and is discretized every 8.76 m resulting in 10 elements along the height. Gross properties of the turbine system are presented in table 1. A full description of structural properties and dimensions are found in [Jonkman et al.; 2009]. Virtual sensors are located at the top and midpoint of the tower. Our model only includes the tower therefore the shear force at the connection between the nacelle and the tower was determined from the FAST simulations. Twenty test cases were considered which span four operational conditions; a parked turbine with blades at 0 pitch, a parked turbine with blades at 90 pitch, an operating turbine with variable controlled pitch, and an operating turbine with optimal pitch angle for five different wind regimes. The operational turbines were initialized at the rated rotor speed of 12.1 rpm. Simulations were sampled in 10-minute steady state intervals with a time step of 0.01 seconds. A schematic of the 5 MW reference wind turbine system is seen in Fig. 3.1. The number of nodes, the location of the wind and shear forces, the physical dimensions, and the MBO on the updated system is presented.
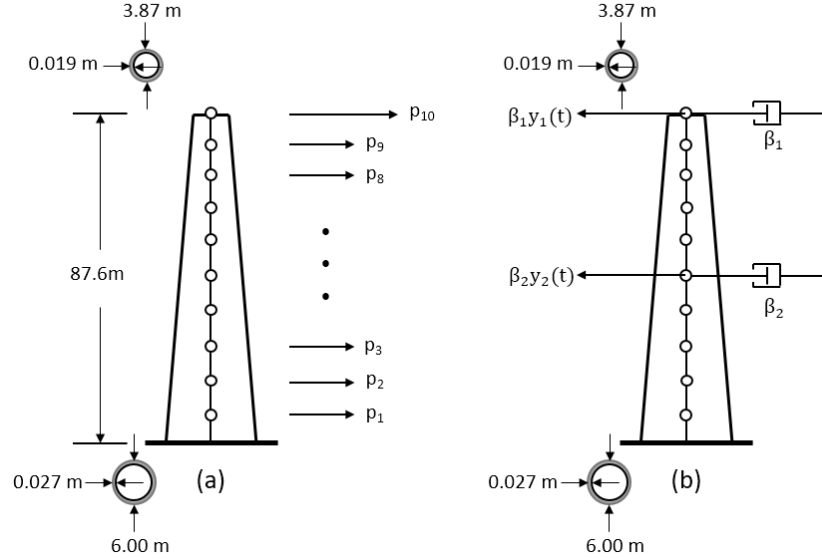
Figure 3.1: (a) Schematic of the 5 MW reference turbine and (b) the MBO estimator. The number of nodes, the location of the forces, the physical dimensions, and the estimator are shown.

Table 3.1: NREL 5-MW Baseline Wind Turbine Properties.

NREL 5-MW Baseline Wind Turbine Gross Properties		Full-System Natural Frequencies in Hertz	
Rating	5 MW	1st Tower Fore-Aft	0.324
Rotor Configuration	Upwind, 3 Blades	1st Blade Collective Flap	0.6993
Hub Height	90 m	1st Blade Asymmetric Edgewise	1.0793
Cut-in, Rated, Cut-Out Wind Speed	3 m/s, 11.4 m/s, 25 m/s	2nd Blade Asymmetric Edgewise	1.9337
Cut-in, Rated Rotor Speed	6.9 rpm, 12.1 rpm	2nd Blade collective Flap	2.0205
Blade Length	61.5 m	2nd Tower Fore-Aft	2.9003
Tower Structural-Damping Ratio	1%		

3.6.1 WIND LOAD SIMULATION

The wind velocity field is simulated in TurbSim, a module of FAST. TurbSim numerically simulates the time series for three-component wind speed vectors in a rectangular two dimensional grid using a statistical model. Our simulations used TurbSim to generate unidirectional wind speed time series at each nodal point of the tower FEM. We realized a IEC Kaimal Spectra with a reference height of 10 m, a surface

Test	Wind Profile	Pitch	Operating Conditions	E_{top}	E_{mid}
1	Cut In	0	Parked	7.60E+08	5.21E+08
2	Rated	0	Parked	6.43E+08	4.42E+08
3	Cut Out	0	Parked	6.83E+08	4.75E+08
4	8 m/s	0	Parked	6.46E+08	4.37E+08
5	17 m/s	0	Parked	5.76E+08	3.95E+08
6	Cut In	90	Parked	6.45E+08	4.56E+08
7	Rated	90	Parked	4.87E+08	3.45E+08
8	Cut Out	90	Parked	4.93E+08	3.55E+08
9	8 m/s	90	Parked	7.40E+08	5.52E+08
10	17 m/s	90	Parked	4.26E+08	3.01E+08
11	Cut In	Variable	Generating	*	*
12	Rated	Variable	Generating	7.22E+08	4.98E+08
13	Cut Out	Variable	Generating	2.34E+08	1.55E+08
14	8 m/s	Variable	Generating	8.28E+08	5.70E+08
15	17 m/s	Variable	Generating	4.13E+08	2.81E+08
16	Cut In	90	Generating	6.62E+08	4.71E+08
17	Rated	0	Generating	7.22E+08	4.98E+08
18	Cut Out	23	Generating	3.37E+08	2.25E+08
19	8 m/s	0	Generating	1.70E+09	1.37E+09
20	17 m/s	13	Generating	5.68E+08	3.95E+08

roughness length of 0.1, and various mean wind speeds at the reference height. The other input variables were set to default. A realization of each wind regime and its corresponding PSD is shown in Fig. 3.2. The mean wind speed of the wind regimes are 3, 8, 11, 17, and 24 m/s, which correspond to the cut-in wind speed, between the cut-in and rated wind speed, the rated wind speed, between the rated and cut-out wind speed, and the cut-out wind speed for the 5 MW reference turbine. The power of the unmeasured forcing resides in the low frequency region, hence the lower order modes will be excited for the wind turbine system. Table 2 defines the parameters used in the 20 simulated test cases including the corresponding damper values. For test case 11, the FAST controller wouldn't initiate due to the wind speed being at the cut in value.

The associated wind loads for a rated wind speed of the operational turbine is shown in Fig. 3.3, the wind load value is compared to the shear loading at the top of the tower to emphasize the magnitude of the shear force from the rotor interaction.
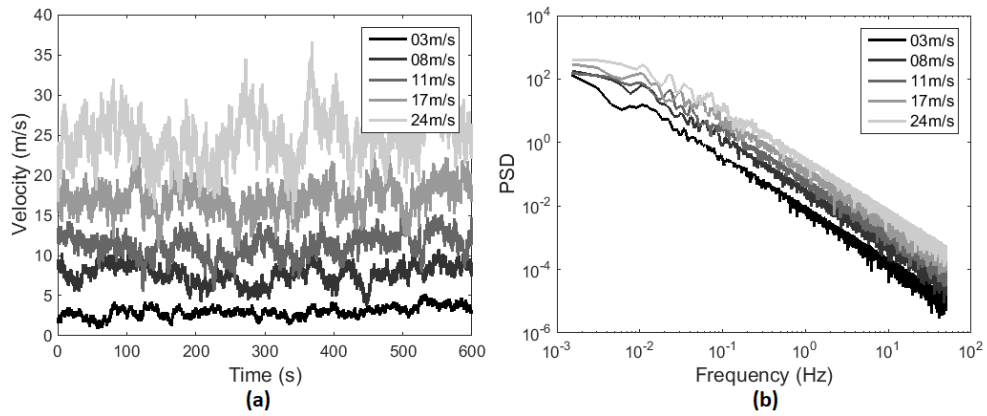
Figure 3.2: (a) Realization of wind velocity field at the hub height for five different full field mean wind speeds (U = 3, 8, 11, 17, and 24 m/s) and (b) their corresponding PSD.
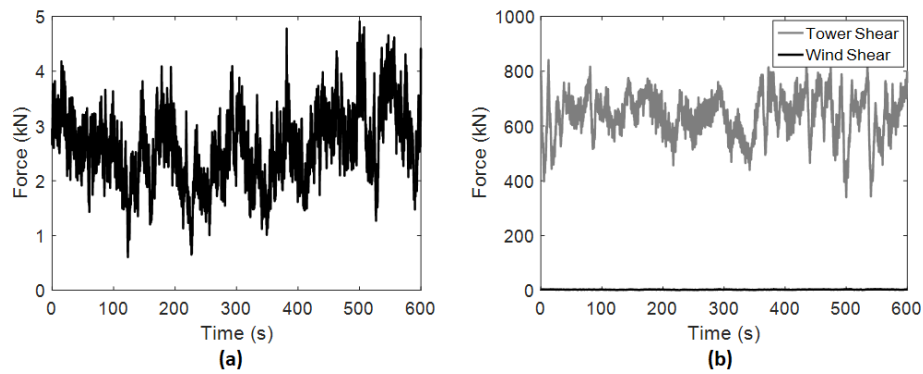
Figure 3.3: (a) Wind loading on an operating wind turbine at a rated wind speed of 11 m/s. (b) The wind loading is then compared against the shear loading at the tower-nacelle connection.

3.6.2   TOWER SHEAR FORCE

The FAST model includes a combined multi-body and modal-dynamics formulation to solve the nonlinear equations of motion that are derived and implemented using Kane's method. Modal properties of the blades and tower are used as input, while the multi-body formulation includes the platform, nacelle, generator, gears, and hub.

To determine the true dynamics of the wind turbine substructure it is necessary to determine the connection forces between the nacelle and tower. The shear force at the connection contains the coupled dynamic information of the tower and the rotor which is contained within its PSD shown in Fig. 3.4. The defined peaks correspond to the first and second mode of the tower and blades.
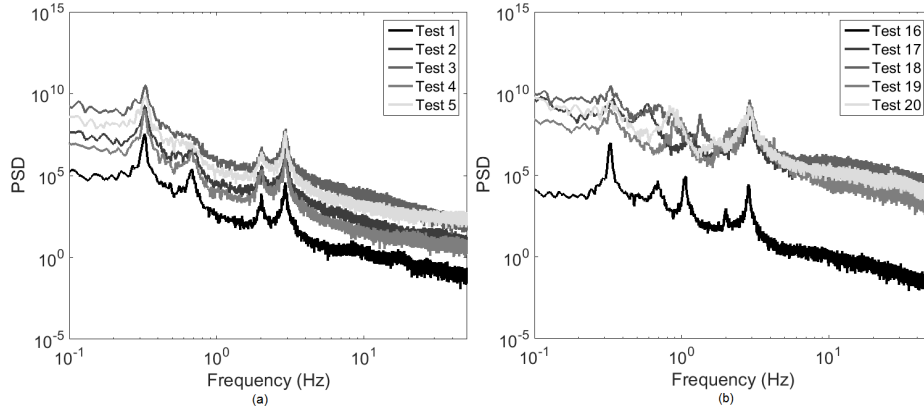
Figure 3.4: (a) The PSD of the tower shear force for a braked wind turbine (test cases 1-5). (b) The PSD of the tower shear force for an operating wind turbine (test cases 16-20).

The shear force at the nacelle connection accounts for the tower and blade deflections, tilt/pre-cone angles, dynamic excitation, etc [Noppe et al.; 2016]. A more detailed description of dynamic modeling using Guyan Reduction [Guyan; 1965] or the Craig-Bampton method [Craig & Bampton; 1968] can be found in literature while its application to a wind turbine support structure can be found in [van der Valk & Voormeeren; 2012].

3.6.3 FLANGED TOWER BOLT TENSION

For wind turbine applications bolted joints consist of interior or exterior flange connections along the steel tubular structure. Connections are susceptible to bolt fatigue

damage and can lead to tower collapse. When the structure is subjected to a bending moment the maximum tension force can be determined by a conventional linear force distribution method as seen in Fig. 3.5 and the following equation [Azim; 2013].
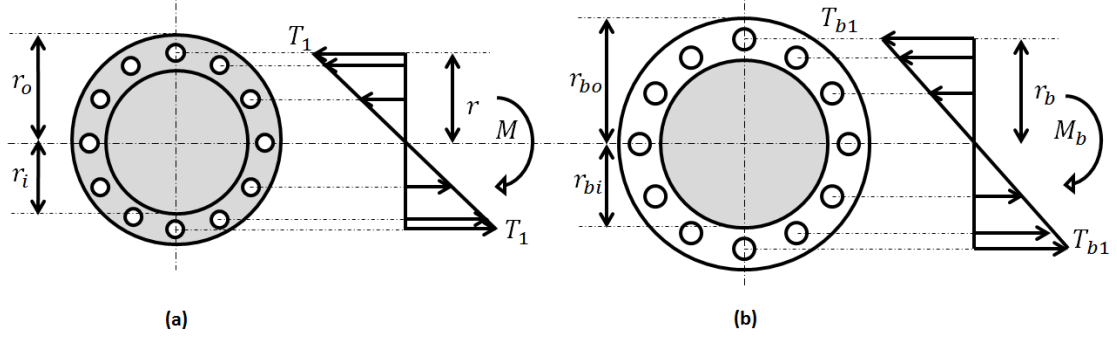
Figure 3.5: The force distribution of a typical flanged pipe joint with 12 bolts. (a) is a location on the tower with interior bolts, (b) is the exterior base bolts of the tower.

$$\mathbf{T}_{max} = \frac{M}{2r + \sum_{b=1}^{N} 4rsin(\theta_b)^2} \tag{3.32}$$

where M is the applied bending moment, r is the distance from the center of the pipe to the center of the bolt, and θ_b is the circular angle of the bolt. This simplified approach does not account for the effect of variation in flange thickness and/or the diameter of the bolt. A more detailed analysis requires a modification of the FEM to incorporate a change in the stiffness of the structure at bolted connections, thorough derivations can be found in the literature [Azim; 2013, Tafheem & Amanat; 2015]. Bolts are also subjected to shear forces which can be readily estimated using the proposed method.
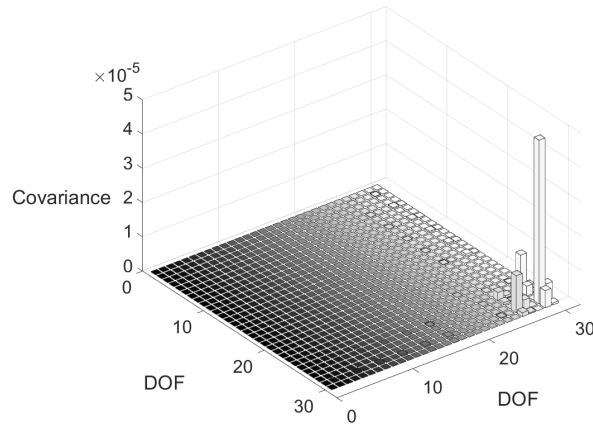
Figure 3.6: The covariance matrix Q. The 29th DOF is the location of the shear loading force.

3.6.4 KALMAN FILTER COMPUTATION

The KF gain matrix was computed while the **R** and **Q** matrices were held constant. The noise covariance matrix **R** is dependent on the simulated wind conditions and is five percent of the standard deviation of the velocity measurements. The equivalent load covariance matrix **Q** is also dependent on the simulated wind conditions and is calculated by determining the covariance matrix of the load vector throughout the time period of interest. Due to this dependence the values of **R** and **Q** vary for each simulation under consideration. A realization of the **Q** matrix is seen in Fig. 3.6. Note that the magnitude of DOF [29,29] is significantly higher than the other DOF's, this is the location of the shear interaction force at the tower-nacelle connection.

81
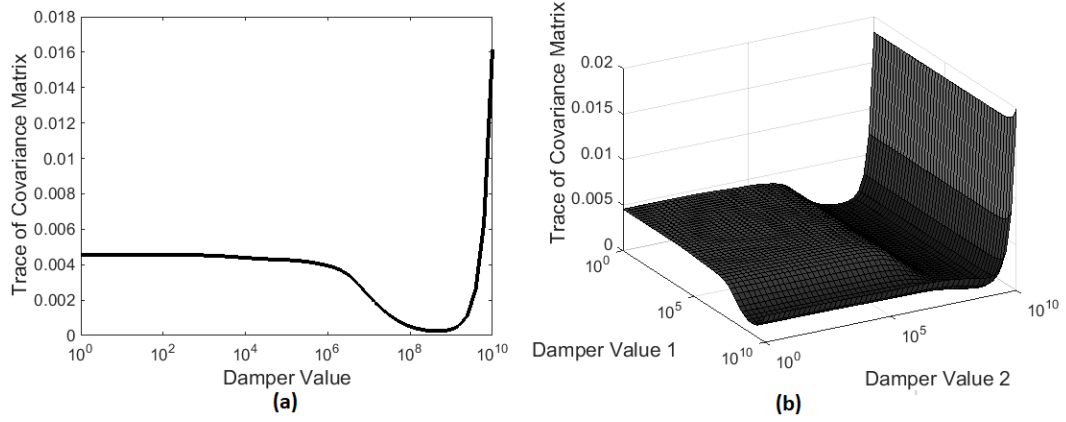
Figure 3.7: The optimization of E for (a) one and (b) two sensor locations for an operating turbine with variable pitch at cut-out wind speed.

3.6.5 Optimal E Matrix

The FEM-based estimator was computed by determining the feedback matrix **E** from the optimization of equation 29. When a single virtual sensor measurement is used, **E** will be a single value and if two measurements are used then **E** will be a diagonal $2x2$ matrix. The **MATLAB**[ö] function, `fminsearch` was used to optimize equation 29 by finding the optimal **E** value(s) that minimize the trace of the state error covariance matrix. This function uses the Nelder-Mead simplex direct search algorithm to find an optimal solution. The set of all damper values is shown in Fig. 3.7 for one and two sensors of an operating turbine with variable pitch at cut-out wind speed. Similar results were found for the other cases, hence there was a unique minimum for each test case.

3.6.6 ESTIMATOR PERFORMANCE

The accuracy of the three estimators (MBO, KF, and MI) were assessed by comparing twenty simulations with varying operating conditions for the 5 MW reference turbine. Two virtual sensor measurements were used in the estimator formulation for increased tracking capabilities although one sensor was sufficient. For each simulation the bending moment at the base and mid height, the stress at the base and mid height, the tension in the connection bolts at the base and mid height, the shear force at the base of the tower, and the tension and shear force in the bolts was calculated for each estimator. For brevity only the stress at the base, the shear force at the base, and the tension in the connection bolts at the base will be presented for two test cases.

Since the FEM only included the tower of the turbine, the mass of the rotor and nacelle were not included in the formulation of the FEM. However the statistics of the shear force at the connection between the nacelle and the top of the tower was determined from FAST and used directly in the KF and MI while the PSD was used in the optimization of **E** for the MBO. The FAST output was assumed to be the true dynamics of the system and used as a comparison to determine the accuracy of the various estimators.

The confidence intervals for the MBO and KF take advantage of the state error covariance matrix and the local stiffness matrix to determine the element uncertainty. The confidence interval for the MI takes advantage of the square of the modal coordinate ratio and the variance of the measurement noise to determine the element uncertainty. The relative uncertainties can be seen in the remaining figures. The state error covariance matrix for the MBO is larger in relative magnitude than the

KF which results in a larger uncertainty in the dynamics of the system while the modal coordinate ratio and measurement noise variance is small for the MI resulting in a small associated uncertainty. For all test cases a one standard deviation confidence interval was used.

The five wind speed regimes detailed previously interact with four wind turbine operating conditions to account for the twenty simulation test cases. Test cases 1-5 the turbine is parked with 0 pitch, for test cases 6-10 the turbine is parked with 90 pitch, for test cases 11-15 the turbine is operating with variable pitch, for test cases 16-20 the turbine is operating with fixed pitch. The most interesting test cases are case three and twelve. Test case three has the wind turbine parked with a fixed pitch of 0 degrees and a mean wind speed of 24 m/s. This is a worst case scenario for the wind turbine, the blades are not rotating and are fully bracing the wind which mainly activates first modes. This simulation resembles a parked turbine with a pitch failure, where there is no aerodynamics/generation. Test case twelve has an operating turbine with variable pitch at a rated wind speed of 11 m/s simulating a turbine in normal operating conditions.

A comparison between the three estimators for the base stress for test cases three and twelve are shown in Figs. 3.8 and 3.9 respectively. For test case three the estimators are able to match the true dynamics of the system. As stated previously the confidence interval decreases in size from MBO to KF to MI. Note that for this case aerodynamics minimally influence the system response, the tower/rotor systems motion is mainly in the first mode. For test case twelve, aerodynamic effects are seen in the turbulent response. The MBO and KF are able to match the true dynamics of the system, while the confidence interval of the MBO allows for a larger percentage
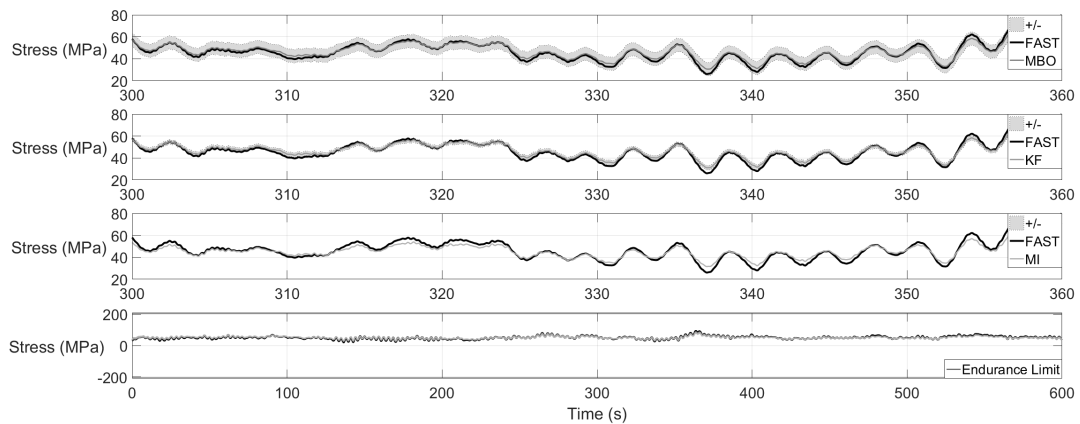
Figure 3.8: Comparison of estimated bending stress at the tower base between the FAST model, the MBO, the KF and MI. The confidence interval is one standard deviation. The test case under consideration is of a 0 pitch parked turbine with a mean wind speed of 24 m/s. The endurance limit is 207 MPa

of the true dynamics to lie within it's bounds. The MI is not able to match the true dynamics of the system to the same degree as the MBO or KF. In an operating turbine several modes are activated; however since two only two sensors are being used the dynamics are constructed from only two mode shapes resulting in poor estimation. In both figures the base stress is plotted against the endurance limit for the ten minute interval. It is seen that the stresses are below the endurance limit therefore no damage is accumulating. This is what we would expect during normal operating conditions. In other words if a damage accumulation algorithm was used along with an SN curve, the cycles wouldn't add significant damage to the structure.

A comparison between the three estimators for the base shear for test cases three and twelve are shown in Figs. 3.10 and 3.11 respectively. For test case three the MBO and KF are able to match the true dynamics of the system yet with higher error than with the base stress. This is also seen for test case twelve. For both case three and twelve the MI is not able to match the true dynamics. The frequency

85
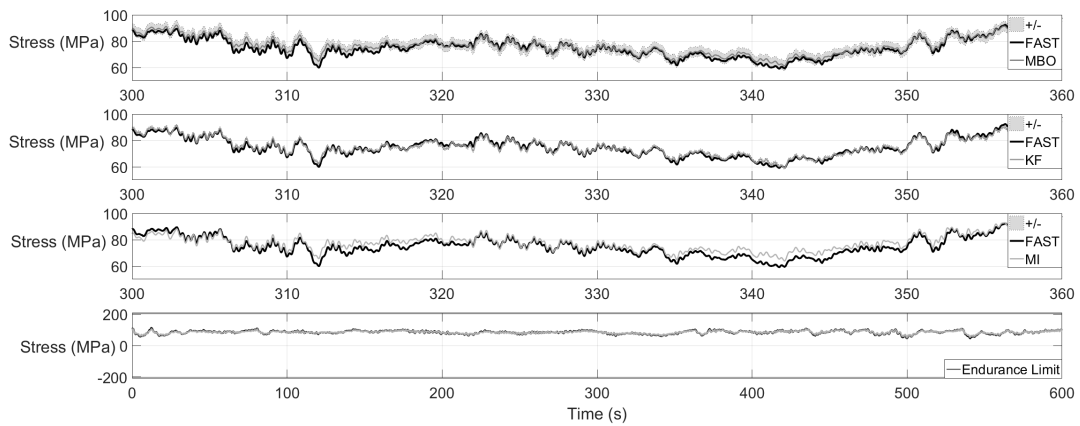
Figure 3.9: Comparison of estimated bending stress at the tower base between the FAST model, the MBO, the KF and MI. The confidence interval is one standard deviation. The test case under consideration is of an operating turbine with variable pitch with a mean wind speed of 11 m/s. The endurance limit is 207 MPa
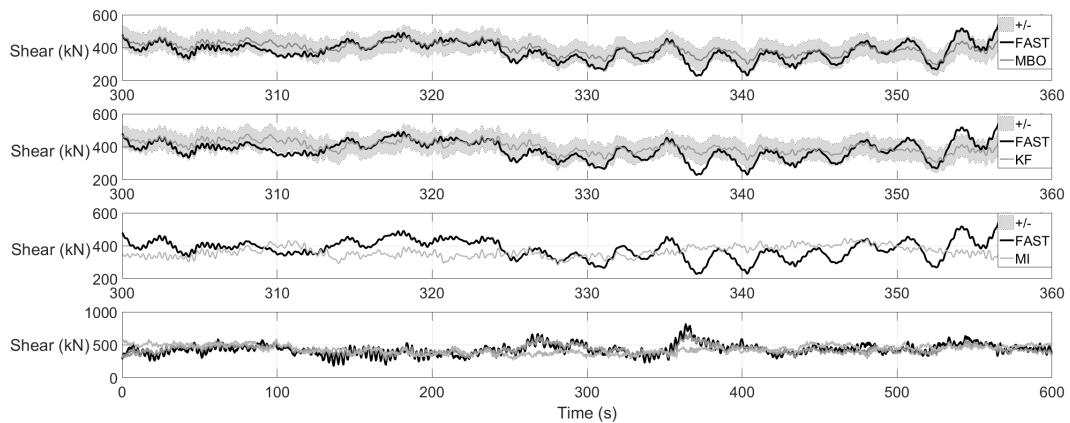
Figure 3.10: Comparison of the estimated shear force at the the tower base between the FAST model, the MBO, the KF and MI. The confidence interval is one standard deviation. The test case under consideration is of a 0 pitch parked turbine with a mean wind speed of 24 m/s.

content is matched yet the magnitudes and shape are incorrect and during the ten minute interval we see that tracking is inadequate.

For the time intervals shown the true dynamics are within the uncertainty bounds
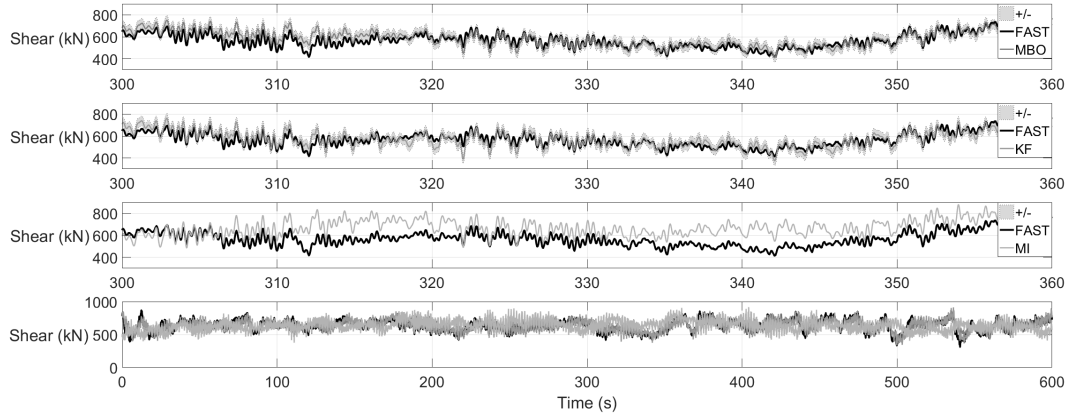
Figure 3.11: Comparison of the estimated shear force at the tower base between the FAST model, the MBO, the KF and MI. The confidence interval is one standard deviation. The test case under consideration is of an operating turbine with variable pitch with a mean wind speed of 11 m/s.

of the estimator. We then quantify the percent of time that the real dynamics of the wind turbine system is within our MBO estimate and its associated uncertainty bounds, Fig. 3.12, this is compared against the KF. For all test cases we find that the accuracy of the MBO is higher than the KF. The error-covariance for the MBO is larger than that of the KF resulting in larger confidence bounds, hence the MBO is more conservative in its estimation. Yet when we look at the average error of our displacement estimates the MBO has an average error of $3.61E-06$ while the KF has an average error of $3.54E-06$. Therefore the MBO provides a similar estimate of the system dynamics compared to the KF with only knowledge of the underlying PSD of the unmeasured excitation which is typically the metric known for wind forces. The average error of the MI is $3.74E-06$.

Another way to provide a comparison between the methods is to determine the error in the damage index. If we assume an SN curve for the wind turbine tower, we can perform cycle counting on the MBO/KF/MI estimates and compare them against

87
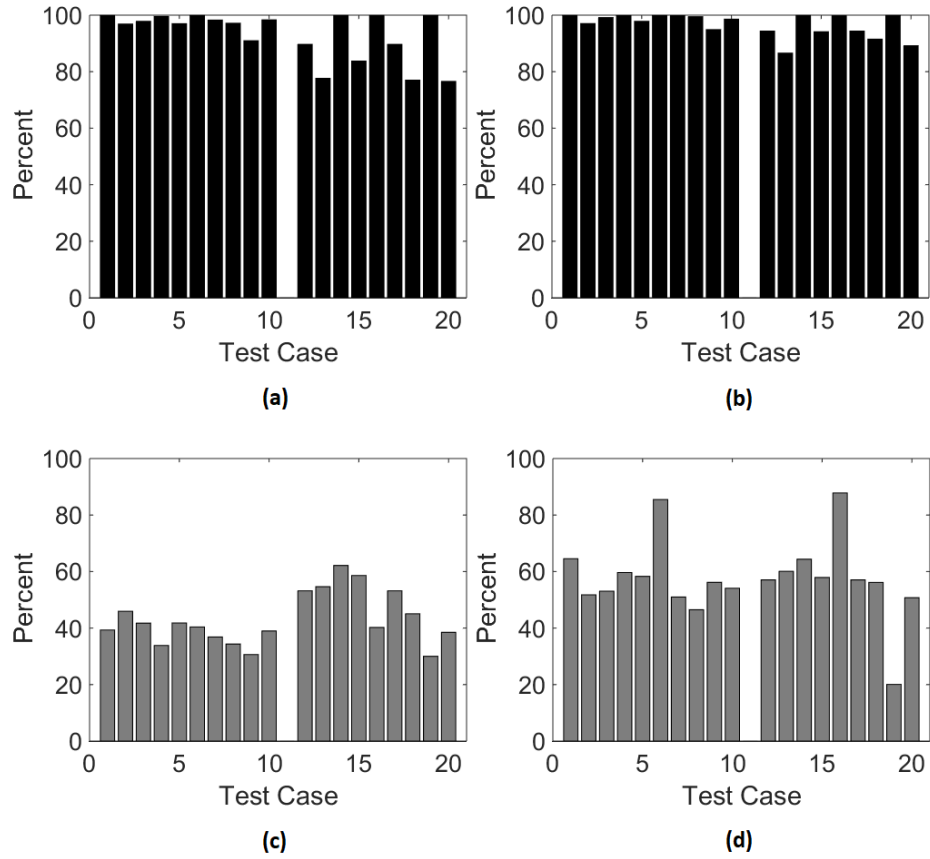
Figure 3.12: Comparison of the accuracy of the MBO against that of the KF for each test case. (a) MBO (base), (b) MBO (mid height), (c) KF (base), and KF(mid height). The accuracy is based on the percent of time the true dynamics is within the uncertainty bounds.

the real system dynamics. This provides a better estimate of the fatigue error since error in displacements can be attributed to phase offset. Fig. 3.13 shows the percent difference between the estimates and the real damage at the base of the turbine tower. The MBO, KF and MI estimates underestimate the damage, with the MBO being more conservative than the KF which was also seen in the stress estimation. In some cases all the estimators perform poorly specifically when the blades are feathered.
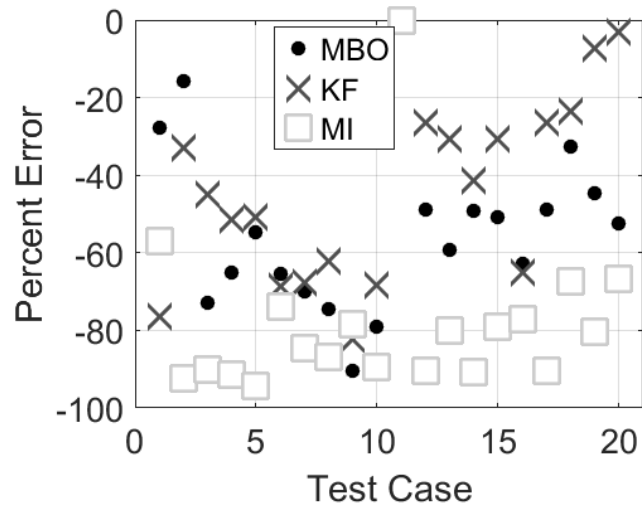
Figure 3.13: Percent error in damage estimates between the MBO/KF/MI and the true dynamics.

3.6.7 BOLT FATIGUE

The 5 MW reference turbine is in a simulated environment with no documentation for the bolted connection design or bolt dimensions. Literature shows that large offshore wind turbines typically have bolt sizes ranging from M64-M72. Schaumann and Eichstadt state that applications with M72 bolts reduce the number of required bolts to 100 [Schaumann & Eichstadt; 2015]. If we assume the use of 100 M72 bolts at the base of the wind turbine tower the maximum tension in the bolt can be determined by equation 31. The pretension is determined from the following equation

$$\mathbf{F}_P = 0.7 R_{p,0.2\%} A_{sp} \tag{3.33}$$

where F_p is the nominal pre-load, $R_{p,0.2\%}$ is the 0.2% yield stress and A_{sp} is the tensile stress area of the bolt. For the 5 MW turbine a pre-tension of 1526 kN should be
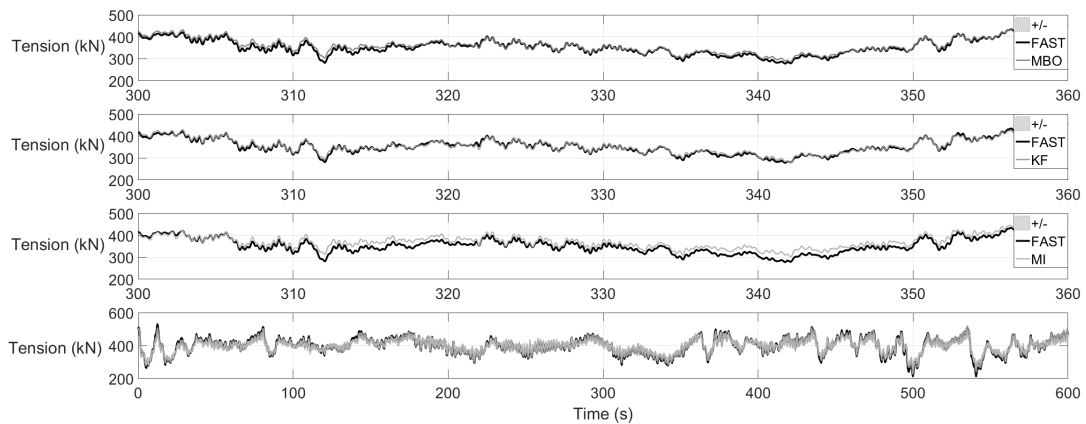
Figure 3.14: Comparison of estimated bolt tension at the tower base between the FAST model, the MBO, the KF and MI. The test case under consideration is of an operating turbine with variable pitch with a mean wind speed of 11 m/s.

used for the 100 M72 bolts. The pre-tension is applied to the bolts for the test cases under consideration. A bolt fatigue analysis would use the estimated bolt tension to quantify damage but this is outside the scope of this paper. Fig. 3.14 show the tension in the base bolts for test case 12. Equation 3.33 uses the estimated base moment we found previously multiplied by a constant therefore again we see that the MBO, KF, and MI are able to match the true dynamics, with the MI having the greatest error.

3.7 CONCLUSIONS

This paper expands on the problem of tracking internal forces on minimally instrumented structures subjected to turbulent stationary wind. The performance of three popular methods for response and fatigue damage estimation are compared,namely, the Kalman filter, model-based observer and modal interpolation. The comparison

is performed in a simulated environment that is not ideal with respect to the afore-mentioned methods. The authors treat the particular case of estimating time history of stresses, bolt tensions, and shear forces throughout the tower of a simulated 5MW wind turbine under 20 different conditions with varying wind profile, blade pitch angle and energy generation.

For response estimation it is shown that the Modal interpolation method is out-performed by the model-based observer and Kalman filter in nearly all the cases. It was found for all case the model-based observer seems to overestimate the estimation variance while the Kalman filter displays a slight underestimation of estimation variance with respect to the actual error.

In the case of fatigue damage estimation, the rainflow cycle counting was used together with Miner's rule. Again, modal interpolation is outperformed by both the Kalman filter and the model-based observer, with the Kalman filter providing slightly superior estimation accuracy than the model-based observer.

In conclusion, based on the simulated results, the authors recommend either the Kalman filter or the model-based observer over modal interpolation.

References

[Azim; 2013] Azim, R. (2013). An analytical investigation on bolt tension of a flanged steel pipe joint subjected to bending moments. *International Journal of Engineering and Applied Sciences.* 2(3):71-81.

[Baqersad et al.; 2015] Baqersad, J. Niezrecki, C. Avitabile, P. (2015). Extracting full-field dynamic strain on a wind turbine rotor subjected to arbitrary excitations using 3d point tracking and a modal expansion technique. *Sound and Vibration.* 352:16-29.

[Benedetti et al.; 2013] Benedetti, M. Fontanari, V. Battisti, L. (2013). Structural health monitoring of wind towers: residual fatigue life estimation. *Smart Materials and Structures.* 22(4): 045017

[Blanco; 2009] Blanco, MI. (2009). The economics of wind energy. *Renewable and Sustainable Energy Reviews.* 13(6):1372-1382.

[Ciang et al.; 2008] Ciang, CC. Lee, JR. Bang, HJ. (2008). Structural health monitoring for a wind turbine system: a review of damage detection methods. *Measurement Science and Technology.* 19(12): 122001.

[Chou & Tu; 2011] Chou, JS. Tu, W. (2011). Failure analysis and risk management of a collapsed large wind turbine tower. *Engineering Failure Analysis.* 18(1):295-313

[Craig & Bampton; 1968] Craig, RR. Bampton, MCC. (1968). Coupling of Substructures for Dynamic Analyses. *AIAA Journal.* 6(7):1313-1319.

[CWIF; 2016] CWIF. (2016). Accident statistics. URL http://www.caithnesswindfarms.co.uk/

[Erazo & Hernandez; 2014] Erazo, K. Hernandez, EM. (2014). A model-based observer for state and stress estimation in structural and mechanical systems: Experimental validation. *Mechanical Systems and Signal Processing.* 43(1):141-152

[Fujiyam et al.; 2014] Fujiyama, C. Yonetsu, K. Maeshima, T. Koda, Y. (2014). Identifiable stress state of wind turbine tower-foundation system based on field measurement and fe analysis. *Procedia Engineering.* 95:279-289.

[Gelb; 1996] Gelb, A. (1996). *Applied Optimal Estimation.* 14th ed., MIT Press: Cambridge, MA

[Guyan; 1965] Guyan, R. (1965). Reduction of stiffness and mass matrices. *AIAA Journal.* 3:380

[Hammerum et al.; 2007] Hammerum, K. Brath, P. Poulsen, NK. (2007). A fatigue approach to wind turbine control. *Journal of Physics:Conference Series.* 75(1): 012081.

[Hernandez; 2011] Hernandez, EM. (2011). A natural observer for optimal state estimation in second order linear structural systems. *Mechanical Systems and Signal Processing.* 25(8):2938-2947.

[Hernandez; 2013] Hernandez, EM. (2013). Optimal model-based state estimation in mechanical and structural systems. *Structural Control and Health Monitoring.* 20(4):532-543.

[Hernandez et al.; 2013] Hernandez, EM. Bernal, D. Caracoglia, L. (2013). On-line monitoring of wind-induced stresses and fatigue damage in instrumented structures. *Structural Control and Health Monitoring.* 20(10);1291-1302.

[Iliopoulos et al.; 2014] Ilopoulos, A. Devriendt, C. Guillaume, P. Van Hemelrijck, D. (2014). Continuous Fatigue Assessment of an Offshore Wind Turbine Using a Limited Number of Vibration Sensors. *EWSHM - 7th European Workshop on Structural Health Monitoring.*

[Iliopoulos et al.; 2015] Iliopoulos, AN. Weijtjens, W. Hemelrijck, DV. Devriendt, C. (2015). Prediction of dynamic strains on a monopile offshore wind turbine using virtual sensors. *Journal of Physics: Conference Series.* 628(1):012108.

[Iliopoulos et al.; 2016] Iliopoulos, A. Shirzadeh, R. Weijtjens, W. Guillaume, P. Hemelrijck, DV. Devriendt, C. (2016). A modal decompositionand expansion approach for prediction of dynamic responses on a monopile offshore

wind turbine using a limited number of vibration sensors. *Mechanical Systems and Signal Processing.* 68-69:84-104.

[Jonkman & Buhl; 2005] Jonkman, B. Buhl, M. (2005). Turbsim user's guide. http://wind.nrel.gov/designcodes/preprocessors/turbsim/turbsim.pdf. National Renewable Energy Laboratory. Golden, CO, USA.

[Jonkman & Buhl; 2005b] Jonkman, J. Buhl, M. (2005). Fast user's guide. NREL/EL-500-38230 (previously NREL/EL-500-29798). National Renewable Energy Laboratory. Golden, CO, USA.

[Jonkman et al.; 2009] Jonkman, J. Butterfield, S. Musial, W. Scott, G. (2009). Definition of a 5-mw reference wind turbine for offshore system development. NREL/TP-500-38060. National Renewable Energy Laboratory. Golden, CO, USA

[Kalman; 1960] Kalman, R. (1960). A new approach to linear filtering and prediction problems. *Transactions of the ASME. Series D, Journal of Basic Engineering.* 82(1):35-45.

[Miner; 1945] Miner, M. (1945). Cumulative damage in fatigue. *ASME Applied Mechanics Transactions.* 159-164.

[Noppe et al.; 2016] Noppe, N. Iliopoulos, A. Weijtjens, W. Devriendt, C. (2016). Full load estimation of an offshore wind turbine based on scada and accelerometer data. *J. Phys.: Conf. Ser.* 753:072025.

[Pacheco et al.; 2017] Pacheco, J. Oliveira, G. Magalhaes, F. Cunha, A. Caetano, E. (2017). Wind turbine vibration based shm system: influence of the sensors layout and noise. *Procedia Engineering.* 2017;199:2160-2165. x International Conference on Structural Dynamics, EURODYN.

[Schaumann & Eichstadt; 2015] Schaumann, P. Eichstadt, R. (2015). Fatigue assessment of high-strength bolts with very large diameters in substructures for offshore wind turbines. *Proceedings of the twenty-fifth International Ocean and Polar Engineering Conference,ISOPE.*

[Shirzadeh et al.; 2015] Shirzadeh, R. Weijtjens, W. Guillaume, P. Devriendt, C. (2015). The dynamics of an offshore wind turbine in parked conditions: a comparison between simulations and measurements. *Wind Energy.* 18(10):1685-1702.

[Simon; 2006] Simon, D. (2006). *Optimal State Estimation.* John Wiley and Sons: New York, NY

[Soman et al.; 2016] Soman, R. Malinowski, P. Ostachowicz, W. (2016). Bi-axial neutral axis tracking for damage detection in wind-turbine towers. *Wind Energy.* 19:639-650.

[Tafheem & Amanat; 2015] Tafheem, Z. Amanat, K. (2015). Finite element investigation on the behavior of bolted flanged steel pipe joint subject to bending. *Journal of Civil Engineering.* 43(1): 79-91.

[Tatsis et al.; 2017] Tatsis, K. Dertimanis, V. Abdallah, I. Chatzi, E. (2017). A substructure approach for fatigue assessment on wind turbine support structures using output-only measurements. *Procedia Engineering.* x International Conference on Structural Dynamics, EURODYN. 199:1044-1049.

[Tewolde et al.; 2017] Tewolde, S. Hoffer, R. Haardt, H. (2017). Validated model based development of damage index for structural health monitoring of offshore wind turbine support structures. *Procedia Engineering.* x International Conference on Structural Dynamics, EURODYN. 199:3242-3247.

[Tibaldi et al.; 2016] Tibaldi, C. Henriksen, L. Hansen, M. Bak, C. (2016). Wind turbine fatigue damage evaluation based on a linear model and a spectral method. *Wind Energy.* 19: 1289-1306.

[van der Valk & Voormeeren; 2012] van der Valk, P. Voormeeren, S. (2012). An overview of modeling approaches for complex offshore wind turbine support structures. *Proceedings of ISMA.* 4437-4452.

[Veers et al.; 2003] Veers, PS. Ashwill, TD. Sutherland, HJ. Laird, DL. Lobitz, DW. Griffin, DA. Mandell, JF. Musial, WD. Jackson, K. Zuteck, M. Miravete, A. Tsai, SW. Richmond, JL. (2003). Trends in the Design, Manufacture and Evaluation of Wind Turbine Blades. *Wind Energy.* 6(3):245-259

[Weijtjens et al.; 2016] Weijtjens, W. Verbelen, T. Sitter, GD. Devriendt, C. (2016). Foundation structural health monitoring of an offshore wind turbine a full-scale case study. *Structural Health Monitoring.* 15(4):389-402.

[Weijtjens et al.; 2017] Weijtjens, W. Verbelen, T. Capello, E. Devriendt, C. (2017). Vibration based structural health monitoring of the sub-structures of five offshore wind turbines. *Procedia Engineering.* x International Conference on Structural Dynamics, EURODYN. 199:2294-2299.

[Wymore et al.; 2015] Wymore, M. Dam, JV. Ceylan, H. Qiao, D. (2015). A survey of health monitoring systems for wind turbines. *Renewable and Sustainable Energy Reviews.* 52: 976-990.

CHAPTER 4

FATIGUE LIFE PROGNOSIS USING MINIMUM GLOBAL RESPONSE MEASUREMENTS: EXPERIMENTAL VALIDATION

4.1   ABSTRACT

The authors present a probabilistic methodology for fatigue prognosis using global response measurements. The methodology employs a Kalman filter to estimate local stress fields based on global acceleration measurements. The estimated stress field time history along with fatigue damage models are used to compute fatigue damage and its uncertainty in near-real time. The authors present the results from laboratory experiments aimed at validating the proposed methodology. The laboratory model is a one meter 6061-T6 aluminum cantilever beam with a reduced cross-section near the base support to facilitate crack initialization. The structure was excited with

a sequence of base motions, which were realizations of a low-pass white noise. The instrumentation consisted of two accelerometers, a strain gage and a shake table for base excitation. Each beam was tested until failure while the proposed algorithm simultaneously predicted the extent of damage. In all tests conducted, the remaining useful life and its uncertainty was estimated. A stopping criteria was found to be an estimated damage index of 0.60 based on several confidence interval metrics.

4.2 INTRODUCTION

Fatigue damage can be defined as the degradation of a material, primarily due to the formation of cracks and resulting from repeated application of stress cycles. Fatigue is a significant and complex phenomena occurring in structures such as aircraft, bridges, turbines, cranes, trains, etc. Although no exact figures are available, it is estimated that upwards of 50% of all mechanical failures in metallic structures can be attributed to fatigue [Gagg & Lewis; 2009, Sobczyk & Spencer; 1991].

Fatigue encompasses two scales. At the microscopic scale; defects, voids and cracks begin to grow and coalesce until one (or multiple) visible macroscopic cracks form and grow up to a point where the structural integrity is compromised. Due to the lack of knowledge regarding the state of microscale defects, it has not been possible to obtain a deterministic theory that fully describes the micro-macro fatigue phenomena. Therefore most fatigue failure models are phenomenological and stochastic.

Three fundamental steps are necessary in order to carry out a fatigue analysis: (1) definition of the loads, (2) detailed stress analysis and (3) statistical model for the variation of material properties. Traditionally a fatigue analysis is carried out during

the structural design stage of a machine or structure, however, more recently there has been a marked interest in monitoring and prognosis of fatigue damage in existing and operating structures. Several important differences exist between the design and the monitoring/prognosis problem in fatigue. In design the engineer is dealing with a hypothetical, yet un-built structure and therefore mechanical properties and boundary conditions can (and must) be assumed. In monitoring, the structure already exists and its mechanical properties can be estimated by processing sensor measurements and non-destructive testing. Furthermore, in the design stage, the structure will begin its operation in a pristine state, while in the monitoring case the current state of the fatigue damage of the structure is highly uncertain.

The traditional practical approach to monitoring fatigue is to carry out a visual inspection, find macroscale cracks and track/predict their evolution; however, in many cases, by the time the cracks grow to a point where they are detectable, the load bearing capacity of the structure has been greatly reduced [Downing; 2012]. A preferable approach is to track fatigue damage on the whole structure prior to the appearance of macroscopic cracks. This would allow for higher levels of reliability, larger lead times and reduced risk. Since it is not cost effective to use strain sensors at all critical locations of a structure, the essential capability that is required to achieve this objective is tracking stress/strain time history through the whole structure by using global vibration measurements, such as accelerations. One possibility to achieve this capability is via state estimation.

State estimation is a model-data fusion approach that aims to reconstruct the state (displacements and velocities in the cases of a linear elastic structure) from noisy measurements and a model. Several methods have been proposed and successfully

validated to estimate unmeasured response in structural systems [Palanisamy et al.; 2015, Hernandez; 2011, Erazo & Hernandez; 2014]. The Kalman filter is the optimal state estimator in the sense that it minimizes the Euclidean norm of the state error time step of interest. A fundamental assumption of the Kalman filter is that the unmeasured excitations are realizations of a Gaussian random process, this condition is often relaxed; while a dual-Kalman filter approach can be used to estimate both the state and the unmeasured excitation in order to reduce the state error [Azam et al.; 2015].

From the estimated stress, the evolution of mechanical fatigue can be monitored by using a rainflow cycle counting algorithm and an S-N curve to estimate fatigue damage [Schijve; 2003]. Fatigue accumulation frameworks with minimal instrumentation have been proposed and validated for a subset of the structures serviceable lifetime in both simulation and experimentally [Papadimitriou et al.; 2011]. The Kalman filter has been shown to be an effective tool to estimate the unmeasured response in structural systems. However, the accuracy of the damage accumulation framework throughout the structures serviceable lifetime has yet to be quantified. Many frameworks incorporate the uncertainty in the stress estimation yet use the expected value of the S-N curve parameters which makes them over-confident in the estimated damage index bounds. The true bounds of the damage estimate provide a more realistic interpretation of the fatigue index in near-real time, allowing for remedial action to be performed before macroscopic crack growth and/or component failure. An important challenge that is addressed in this paper is quantifying the uncertainty in the damage estimate throughout the structures serviceable life by tracking stress cycles.

High fidelity finite element model updating has been proposed by some authors

in order to estimate fatigue damage. Specifically, the hypothesis is that as damage accumulates the mechanical characteristics such as natural frequencies, damping ratios, and mode shapes will also change. Giagopoulos et al. have proposed a structural health monitoring framework that incorporates a model updating method as changes are seen in the structural response to provide an estimate of the fatigue process [Giagopoulos et al.; 2019]. These changes can be incorporated into a fatigue accumulation framework based on updating the joint conditional probability of the damage estimate as knowledge of the damage sensitive features are evaluated [Gobbato et al.; 2012]. The framework has been proposed and experimentally validated for crack propagation trajectories and shown to improve remaining fatigue life estimates [Gobbato et al.; 2014]. As this paper shows, the model updating approach is only viable once the structure is damaged to a point of imminent failure.

This paper proposes and experimentally validates a methodology to estimate and predict the remaining fatigue life of an instrumented structure. A Kalman filter is used to estimate local stress fields based on global acceleration measurements. From the estimated stress, the evolution of mechanical fatigue can be monitored by using a rainflow cycle counting algorithm and an empirical S-N curve to estimate a damage index and its uncertainty using Miner's rule [Schijve; 2003]. The methodology is tested using aluminum cantilever beams with a reduced cross section near the base support to facilitate crack initialization and propagation. The structure is excited until failure with a sequence of base motions, which are realizations of a low-pass white noise. The damage estimate and its uncertainty is tracked in near-real time until macroscopic crack growth is seen and the structures remaining strength has been greatly reduced. The flowchart in Fig. 4.1 illustrates the fatigue framework. To

the authors' best knowledge this is the first paper that tracks fatigue damage and its uncertainty using global measurements until failure. The natural frequency of the system is tracked during the process to show that in non-redundant systems changes in modal characteristics aren't seen until significant microscopic damage has already occurred and failure is imminent, thus highlighting the value of the proposed fatigue monitoring approach.
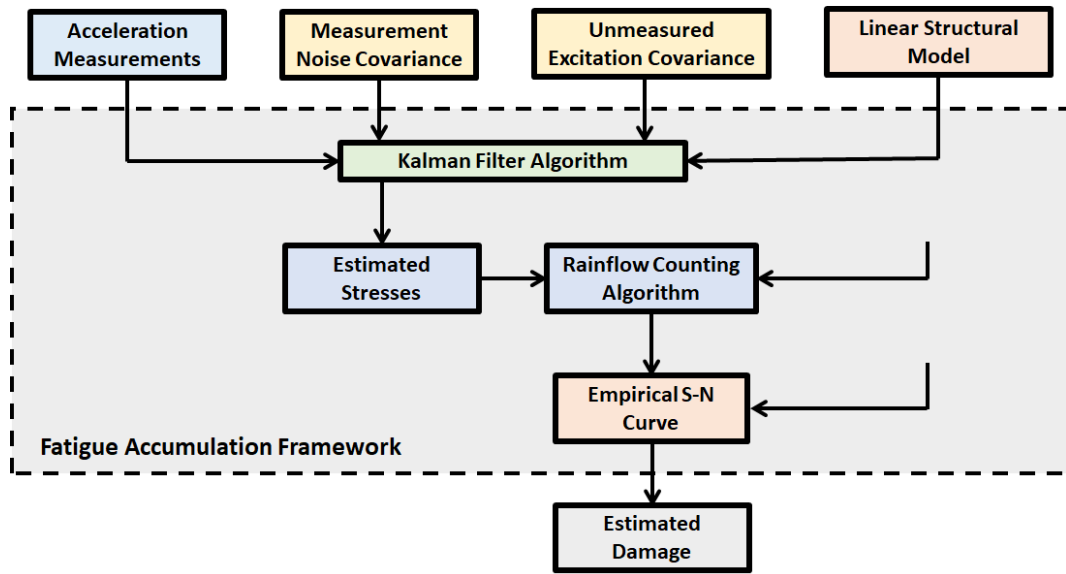
Figure 4.1: Overview of proposed fatigue accumulation framework for remaining fatigue life prediction.

The paper is organized as follows, it begins with a section that provides a description of the fatigue damage framework. This is followed by a section that describes the experimental setup and procedure. The final section presents the experimental results which includes a discussion on the accuracy of the framework and concludes the paper.

4.3   Theoretical Background

We restrict our attention to systems whose dynamic response to ground motion can be described by the following matrix ordinary differential equation

$$\mathbf{M}\ddot{q}(t) + \mathbf{C_D}\dot{q}(t) + \mathbf{K}q(t) = -\mathbf{M}\mathbf{r}\ddot{u}_b(t) \tag{4.1}$$

where $q(t) \in \mathbf{R}^{nx1}$ is the displacement vector at time t, $\mathbf{M}$ is the mass matrix, $\mathbf{C_D}$ is the damping matrix, and $\mathbf{K}$ is the stiffness matrix. The time history of the base acceleration is $\ddot{u}_b(t) \in \mathbf{R}^{1xn}$, and $\mathbf{r} \in \mathbf{R}^{nx1}$ is the influence vector.

The absolute measurements of the system's response are defined by

$$y(t) = -\mathbf{c_2}\mathbf{M}^{-1}\mathbf{K}q(t) - \mathbf{c_2}\mathbf{M}^{-1}\mathbf{C_D}\dot{q}(t) + r(t) \tag{4.2}$$

where $\mathbf{c_2} \in \mathbf{R}^{mxn}$ maps the degrees of freedom to the measurements and $r(t)$ $\in \mathbf{R}^{mx1}$ is the measurement noise.

4.3.1   Kalman Filter

The Kalman filter [Kalman; 1960] is a two-step recursive estimation algorithm. First the Kalman filter estimates the current state variables and their associated uncertainties, then the state estimate of a dynamical system $\hat{x}_{k+1}^{(-)}$ at time $t = (k+1)\Delta t$ is corrected by using a weighted difference between model predictions and measurements,

$$\hat{x}_{k+1}^{(+)} = \hat{x}_{k+1}^{(-)} + \mathbf{K}_{k+1}\left(y_{k+1} - \mathbf{C}\hat{x}_{k+1}^{(-)}\right) \tag{4.3}$$

102

where $\hat{x}_{k+1}^{(+)}$ is the corrected (a posteriori) state estimate and $\hat{x}_{k+1}^{(-)}$ is the a priori state estimate computed for this system as,

$$\hat{x}_{k+1}^{(-)} = \mathbf{A}\hat{x}_k^{(+)} \tag{4.4}$$

$\mathbf{A}$ is the state transition matrix, defined as

$$\mathbf{A} = e^{\mathbf{F}\Delta t} \tag{4.5}$$

where $\mathbf{F}$ is a matrix of the following form

$$\mathbf{F} = \begin{bmatrix} 0 & \mathbf{I} \\ -\mathbf{M}^{-1}\mathbf{K} & -\mathbf{M}^{-1}\mathbf{C_D} \end{bmatrix} \tag{4.6}$$

The recursion method is briefly presented here. A detailed derivation of the gain can be found in [Simon; 2006, Gelb; 1996]. First consider $\mathbf{P}_{k+1}^{(-)}$, the a priori state error covariance matrix at time $t = (k+1)\Delta t$, expressed in the following form

$$E[(x_{k+1} - \hat{x}_{k+1})^T(x_{k+1} - \hat{x}_{k+1})] = \mathbf{P}_{k+1}^{(-)} = \mathbf{A}\mathbf{P}_k^{(+)}\mathbf{A}^T + \mathbf{Q}_k \tag{4.7}$$

where $\mathbf{Q}_k$ is the covariance matrix of the unmeasured excitation and $\mathbf{P}_k^{(+)}$ is the posteriori state error covariance at the previous time step. The Kalman feedback gain matrix, $\mathbf{K}_{k+1}$ at time $t = (k+1)\Delta t$, is expressed as

$$\mathbf{K}_{k+1} = \mathbf{P}_{k+1}^{(-)}\mathbf{C}^T\left(\mathbf{C}\mathbf{P}_{k+1}^{(-)}\mathbf{C}^T + \mathbf{R}_{k+1}\right)^{-1} \tag{4.8}$$

where $\mathbf{R}_{k+1}$ is the measurement noise covariance. The a posteriori state error covariance matrix is given by

$$\mathbf{P}_{k+1}^{(+)} = (\mathbf{I} - \mathbf{K}_{k+1}\mathbf{C})\mathbf{P}_{k+1}^{(-)} \tag{4.9}$$

4.3.2 FATIGUE DAMAGE

The Palmgren-Miner linear accumulation rule is used to evaluate fatigue damage. The rule states that the fatigue damage at any stress cycle is the ratio of the operational cycles to the average number of cycles to failure [Miner; 1945]. The damage time history can be expressed as

$$\mathbf{D} = \sum_i D_i = \sum_i \frac{n(\sigma_i)}{N_f(\sigma_i)} \tag{4.10}$$

where $n(\sigma_i)$ is the number of cycles at stress level σ_i and $N_f(\sigma_i)$ is the number of cycles to failure at the same stress level. The estimated stress time history is used in combination with a rainflow counting algorithm to determine the number of cycles at each stress level. Then an empirical S-N curve is used to determine the number of cycles to failure at the estimated or measured stress levels. One way to express an S-N curve is:

$$\log(N_f) = K - b \log(\sigma_i) \tag{4.11}$$

where K and b are empirically determined material-dependent parameters that describe the shape of the curve.

4.4 Experiment and Procedure

Ten (10) instrumented fatigue critical 6061-T6 aluminum cantilever beams with dimensions shown in Fig. 4.2, were used to validate the procedure. The aluminum beams were machined at the Instrumentation and Model facility at the University of Vermont. Free vibration data was used to identify the first modal frequency and a damping ratio for each beam. The average values were 4.97 Hz and 0.017 respectively.

Each cantilever was instrumented with two accelerometers (PCB 333B30) as indicated in Fig. 4.3(c),(d). Cantilever five (5) was instrumented with a strain gage (PCB 740B02) shown in Fig. 4.3(e). The data was recorded using the LMS Scadas Mobile Data Acquisition System at a sampling frequency of 100 Hz. The cantilever beams were attached to the Quanser Shake Table II using plates as shown in Fig. 4.3(b). The experimental set-up is presented in Fig. 2(b) where the location of the applied base motion, accelerometer measurements and strain measurement are shown.

The objective is to track fatigue damage at the critical location where there is a reduced cross section. This is performed by estimating the stress time history between 13 and 17 cm above the base support along with an empirical S-N curve. Each cantilever was subjected to a sequence of base motions, which are a realization of a low-pass white noise. A 60 second frequency sweep ranging from 4-6 Hz was used to excite the structure. This provided a dynamic amplification factor that would on average cause structural failure within several hundred loading sequences. The estimates obtained from the Kalman filter will be compared against the measured response for cantilever five (5) at the location of the strain gage. In order to not affect the fatigue properties of the beam at the reduced cross section the strain gage

was mounted 25 cm from the base.
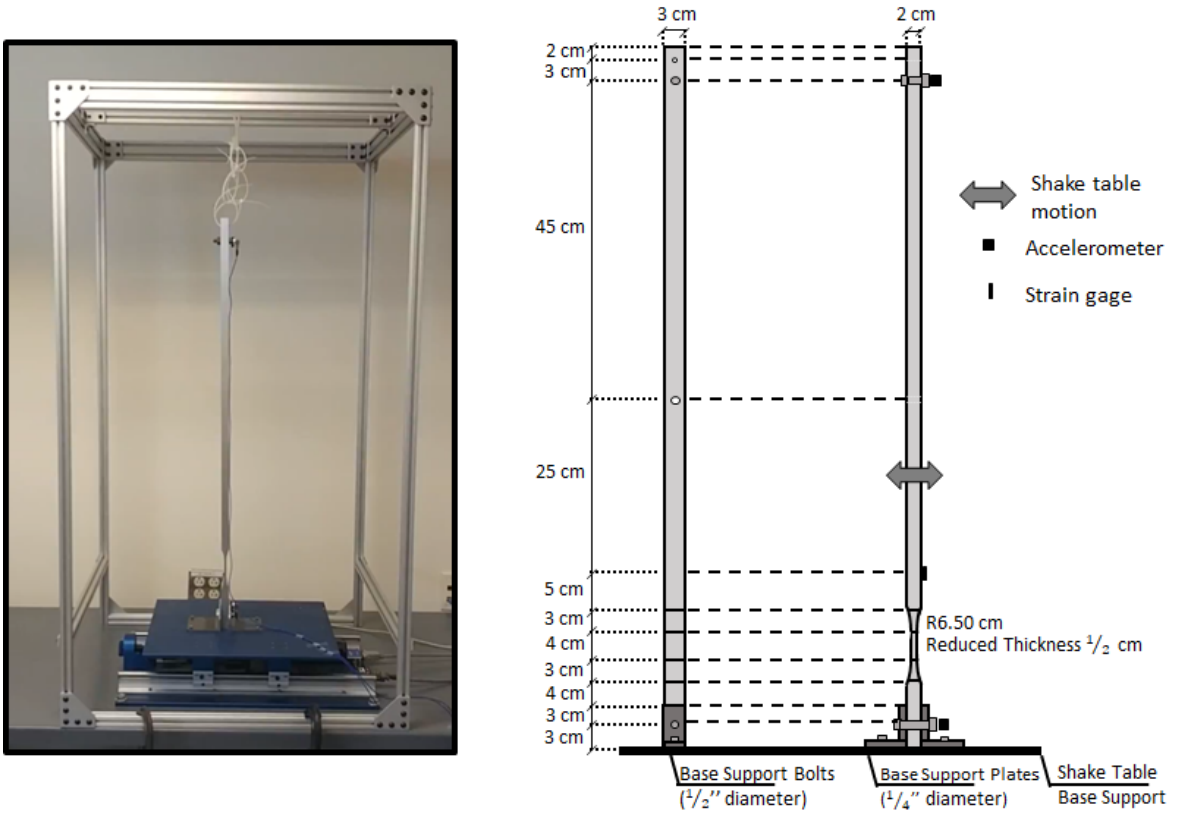
Figure 4.2: (a) Experimental set-up for ground motion dynamic test (b) Instrumented cantilever test beam with dimensions, sensor locations and excitation description.

4.4.1 KALMAN FILTER FORMULATION

Three matrices need to be defined in order to formulate the discrete-time Kalman filter. The initial error covariance matrix, the measurement noise covariance and the covariance matrix of the unmeasured excitation. For each test case the cantilever structure begins at rest; therefore the initial error covariance matrix is zero. The measurement noise covariance is dependent on the accelerometers that were used.
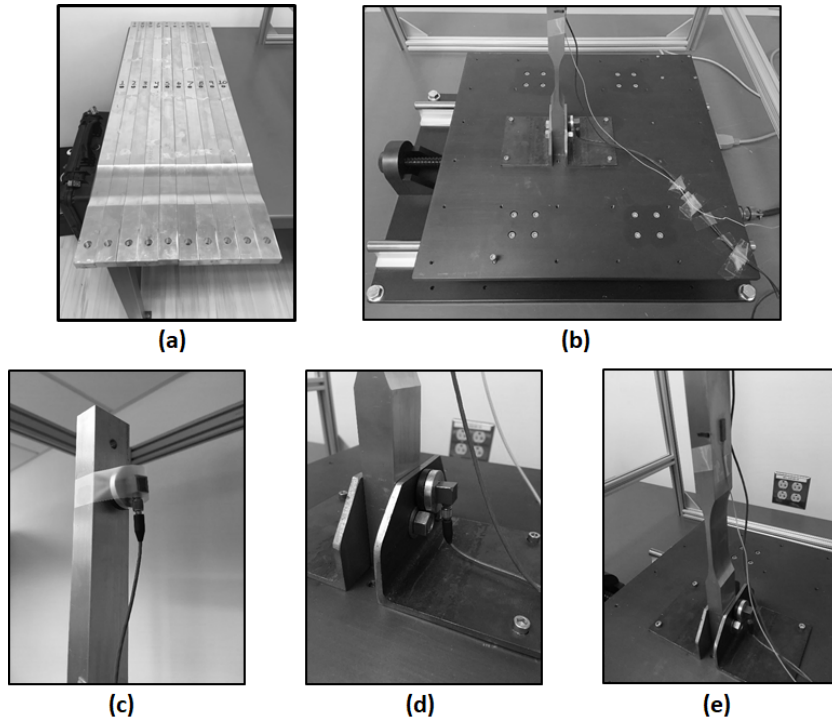
Figure 4.3: Experimental set up for fatigue testing; (a) Ten (10) fatigue critical 6061-T6 aluminum cantilever beams, (b) Connection to the shake table, (c) Top accelerometer, (d) Base accelerometer, (e) Strain gage.

Note that the only measurement that was used in the Kalman filter implementation was the top accelerometer. The base accelerometer was only used to determine the covariance matrix of the unmeasured excitation. The top accelerometer at rest had a covariance of $2.25\text{x}10^{-6}$ which was used as our $\mathbf{R}$ value. The base accelerometer was used to determine the unmeasured excitation imposed by the base motion. From the measurements a $\mathbf{Q}$ value of 0.0135 was found.

4.5   Results and Discussion

This section presents the results of the fatigue tests for the ten (10) cantilever experiments. Each cantilever was tested until failure, which was defined as a macroscopic crack with a length at least half of the width, 1.5 cm, at the reduced cross section. The cantilevers were subjected to the same 60 second sequence of base motions until failure. A realization of the base motion is presented in Fig. 4.4 with the dynamic response to the same realization shown in Fig. 4.5.

(a)   **(b)**
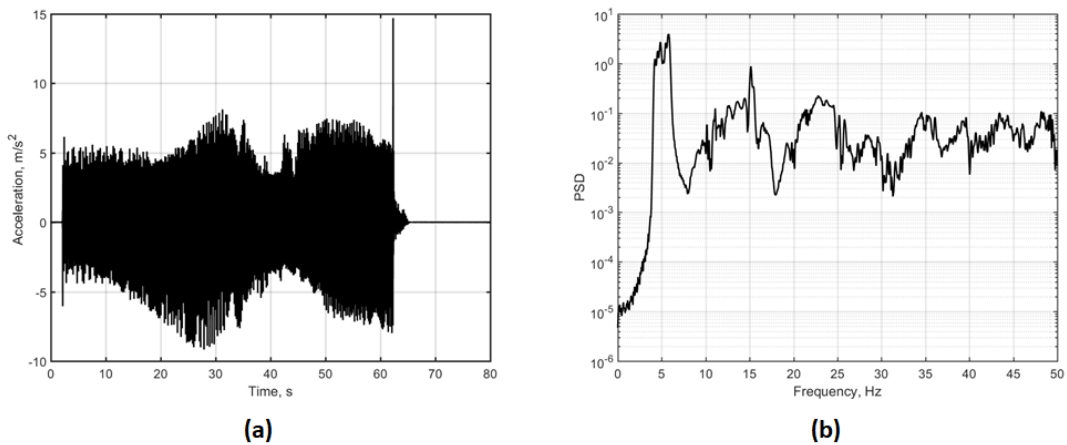
Figure 4.4: Realization of a 60 second base motion, (a) presents the absolute accelerations, and (b) shows the frequency content.

4.5.1   System model

The simulated system model of the cantilever beam is discretized into 26 elements where each node has three degrees-of-freedom; axial, shear, and moment. At the reduced cross section there is element refinement to match the average observed natural frequency of the true beams which is seen in Fig 4.6. This results in a 78 degree-of-

108
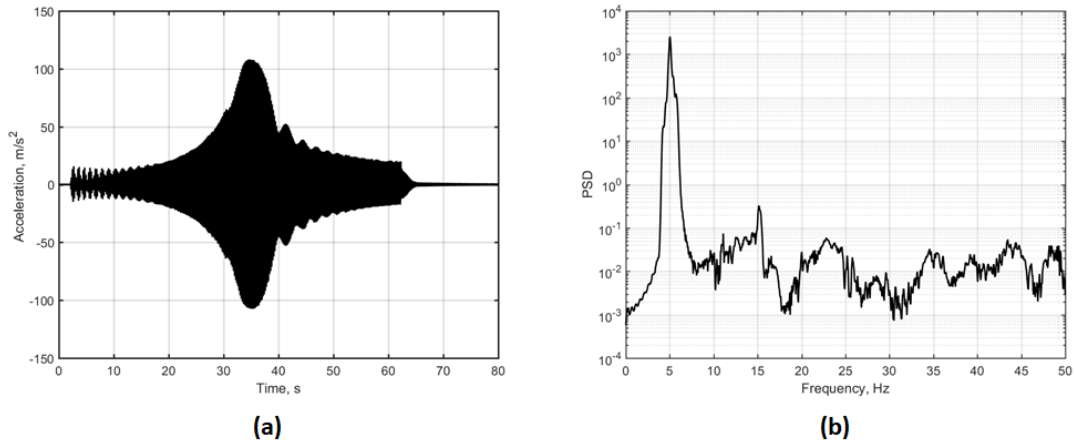
Figure 4.5: Realization of the dynamic response of a 60 second base motion at the top accelerometer, (a) presents the absolute accelerations, and (b) shows the frequency content.

freedom system with a natural frequency of 4.92 Hz and a damping ratio of 0.0165. Therefore the initial model has small yet quantifiable and consistent model error prior to fatigue accumulation.

4.5.2   Fatigue model

An empirical S-N curve from MIL-HDBK-5H: Metallic Materials and Elements for Aerospace Vehicle Structures was used. The S-N curve for 6061-T6 Aluminum with fully reversed stress cycles were based on the net section for an axially loaded specimen. To convert from axial to bending stresses a constant ratio was used, $\frac{0.70}{0.90}$, as recommended in [Juvinall & Marshek; 2012]. The S-N curve is shown in Fig. 4.7 with the corresponding equation in MPa:

$$\log\left(N_f\right) = 20.68 - 67.84 \log\left(S_{eq}\right) \tag{4.12}$$
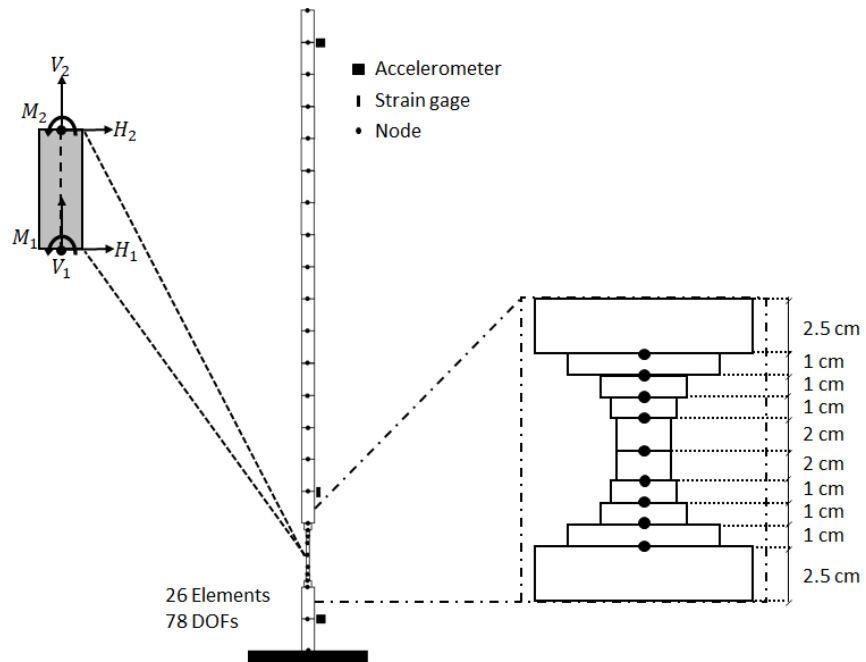
Figure 4.6: The 78 DOF system model for each cantilever beam with an element refinement at the reduced cross section.
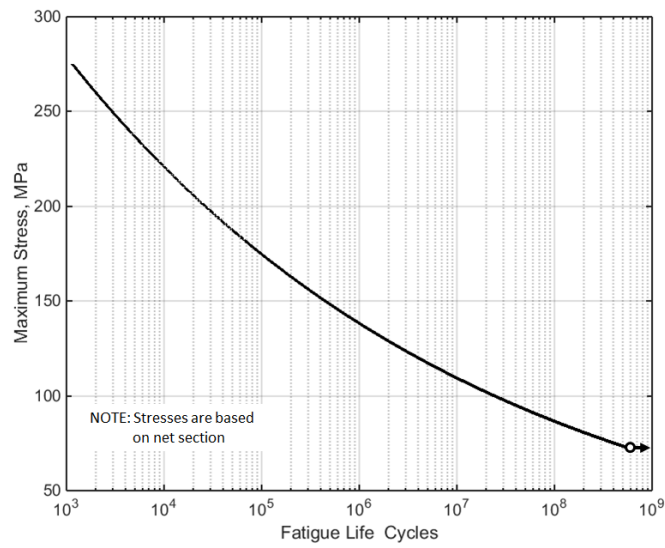
Figure 4.7: The S-N curve for 6061-T6 aluminum for fully reversed axially loaded specimens.

110

where the equivalent stress for a fully reversed stress cycle is defined as,

$$S_{eq} = 2^{0.63} \, S_{max} \qquad (4.13)$$

4.5.3 KALMAN FILTER PERFORMANCE

This section presents the experimental performance of the Kalman filter in tracking stresses in near-real time. The accuracy of the Kalman filter is examined in cantilever five (5) with a dynamic strain gage. For comparison the measured strain is converted to stress by multiplying by the elastic modulus of aluminum (68.9 GPa) which is presented in Fig. 4.8.
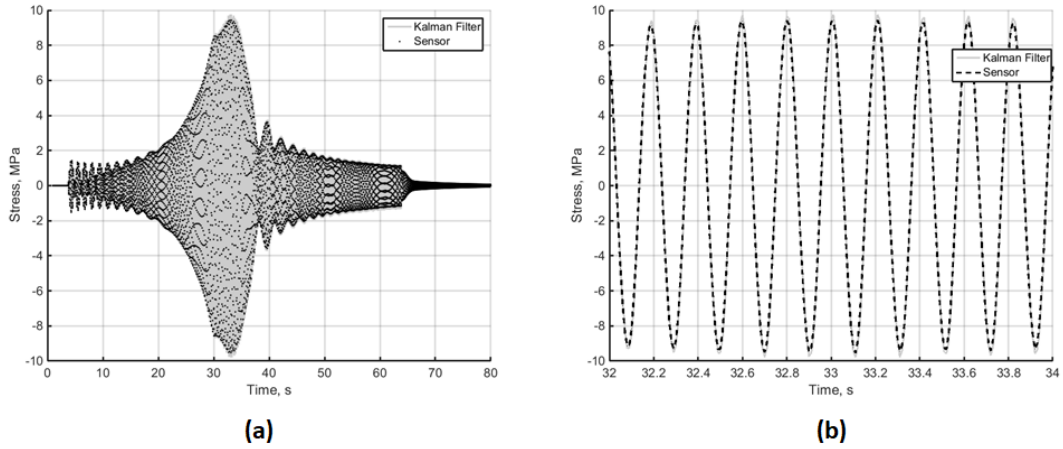
Figure 4.8: Kalman stress estimation compared against strain gage measurement, (a) presents the absolute accelerations, and (b) zooms into the dynamic amplification region.

The Kalman filter is able to estimate stresses with high accuracy throughout the base motion sequence except at the dynamic amplification peak where the Kalman filter overestimates the stress. Cycle counting is performed on the estimated stresses from the Kalman filter, 437 cycles are counted for a corresponding damage of $2.3620e^{-17}$.

111

When cycle counting is performed using direct measurements from the dynamic strain sensor 453.5 cycles are counted for a corresponding damage of $1.8216e^{-17}$.

As test cases are performed the coalescence of microscopic cracks caused a decrease in the natural response frequency of the beams prior to macroscopic crack growth. Fig. 4.9 shows the change in the response frequency of all the cantilevers throughout the fatigue process. A macroscopic crack often formed by 0.90 % of the lifetime, at this point the average natural frequency had decreased from 4.865 Hz to 4.80 Hz.
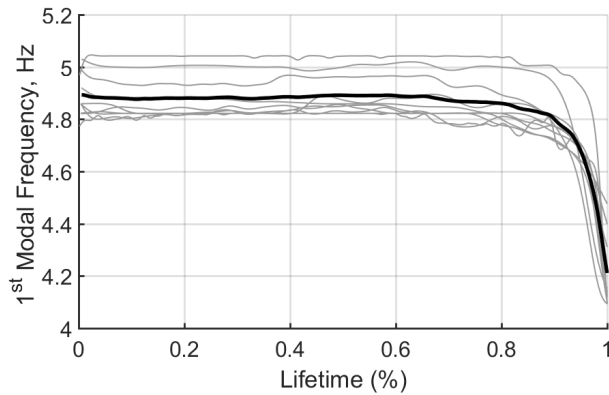
Figure 4.9: Tracking of the natural response frequency throughout the fatigue lifetime of all cantilevers. The black line corresponds to the average modal frequency.

Similar results were found for all ten (10) cantilevers. Therefore it is necessary to determine the effect of model error in the Kalman estimate prior to and during crack growth. A reduction in the stiffness of the element that corresponds to the stress critical location was implemented by a reduction in the elastic modulus of this element by 14%. This resulted in a modeled natural frequency of 4.785 Hz. The Kalman filter was then re-ran with the introduced model error and compared with the strain measurements from cantilever five (5) to determine the accuracy of the estimate during fatigue degradation. The results are seen in Fig. 4.10.
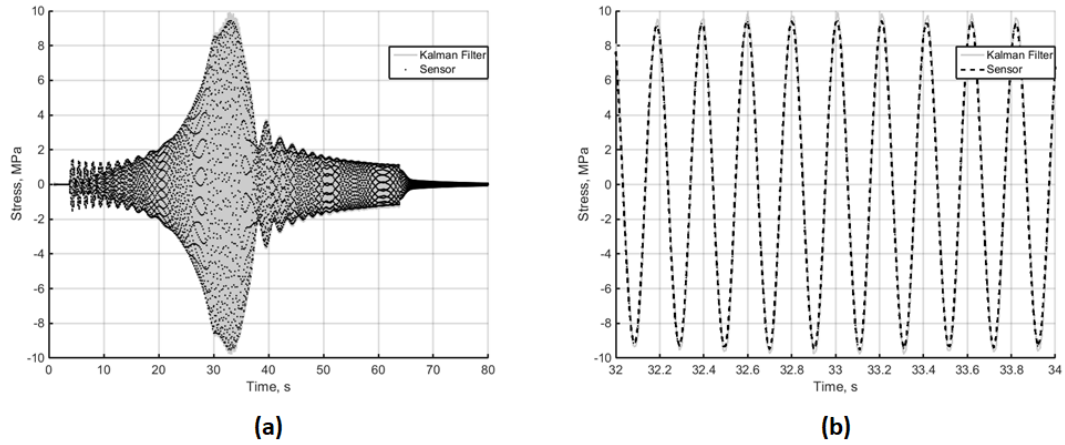
Figure 4.10: Kalman stress estimation for reduced stiffness element at possible fatigue crack location compared against strain gage measurement, (a) presents the absolute accelerations, and (b) zooms into the dynamic amplification region.

The reduced element model overestimates the stresses compared to the original model. If cycle counting is performed on the new Kalman estimate 474 cycles are counted for a corresponding damage of $2.547e^{-17}$. Therefore the Kalman filter will overestimate the number of cycles and the corresponding damage estimate for the test cases where macroscopic crack growth is visible. Yet this is a small percentage of the total lifetime of the structure.

4.5.4 UNCERTAINTY QUANTIFICATION

The accumulation of fatigue damage is a random process. Typically the material properties can be expressed as random variables while the applied loading on the structure is a stochastic process [Shen et al.; 2000]. Uncertainty is introduced into the damage index from the the estimated stresses determined by the Kalman filter and the material properties. The stress estimation uncertainty can be expressed as

a single-sided Gaussian probability distribution with bounds on the acceptable range
of expected damage values per cycle,

$$f(d) = \frac{1}{b}(n_s K)^{(\frac{d}{b})^{(\frac{1-b}{b})}} \frac{1}{\sqrt{2\pi}\sigma_s} e^{-(\frac{((n_s K d)^{\frac{1}{b}} - \mu_s)^2}{2\sigma_s^2})} + \frac{1}{\sqrt{2\pi}\sigma_s} e^{-(\frac{((n_s K d)^{\frac{1}{b}} + \mu_s)^2}{2\sigma_s^2})} \qquad (4.14)$$

where d is the range of possible damages for PDF integration, n_s is the inverse of
the number of cycles at each experienced stress, b, K are the empirically determined
material-dependent parameters that describe the shape of the S-N curve, σ_s is the
standard deviation of the stresses, and μ_s is the mean estimated stresses.

Material fatigue is well understood in a qualitative sense, yet statistical distribu-
tions for fatigue parameters are unable to be derived from this physical interpreta-
tion [Schijve; 2003]. Therefore a distribution must be assumed, the most common
distribution function is the normal distribution which was used for this experimental
validation. Other applicable distribution functions are the $\log(N)$-normal distribu-
tion, the 3-parameter Weibull distribution, and the $\log(N - N_o)$-normal distribu-
tion [Schijve; 2005]. The SN curve shape parameters, originally defined in eq. 11, are
random variables defined as,

$$\mathbf{X} = \begin{bmatrix} K \\ b \end{bmatrix} \qquad (4.15)$$

The parameters presented above are assumed to be jointly Gaussian random variables
with the following PDF,

$$f_X(X) = \frac{1}{\sqrt{|\Sigma|(2\pi)^2}} \exp(-\frac{1}{2}(X - \mu)^T \Sigma^{-1}(X - \mu) \qquad (4.16)$$

where μ is the mean vector and Σ is the covariance matrix.

4.5.5 FATIGUE DAMAGE FRAMEWORK

For each cantilever beam the damage index was tracked in near-real time, the remaining useful life and its uncertainty was estimated. The statically determinant structures were tested until failure while the proposed algorithm simultaneously quantified the extent of fatigue damage. At the onset of macroscopic crack formation the tests were stopped. The location and size of crack at failure is highlighted and shown in Fig. 4.11 for each cantilever. Table 1 presents the fatigue properties of the cantilever beams. For each beam the crack initiation test case and the decrease in natural frequency response was documented and its corresponding damage index at that test was determined. Note that the frequency drops at most 9% at macroscopic crack growth, with most cases being less than 3%. Experimentally the authors have shown that by the time you can quantify and locate damage based on frequency response the structures integrity is already greatly reduced. In most cases the fatigue index had already surpassed one (1).

Table 4.1: Fatigue properties of cantilever beams

Beam #	Mass Kg	1st Modal Frequency Hz	Crack Initiation	Frequency Drop $\frac{t_{cr}}{t_i}$	Estimated Damage Index
1	1.523	5.078	272	0.914	1.383
2	1.525	4.922	637	0.962	0.653
3	1.523	5.078	537	0.942	0.868
4	1.521	5.078	161	0.952	1.712
5	1.525	4.922	223	0.972	0.919
6	1.519	5.000	167	0.957	1.359
7	1.519	4.896	223	0.957	1.900
8	1.525	4.922	203	0.962	1.188
9	1.525	4.922	213	0.972	0.993
10	1.521	4.883	225	0.970	0.951

At first only the uncertainty in the state estimate is used in the proposed al-
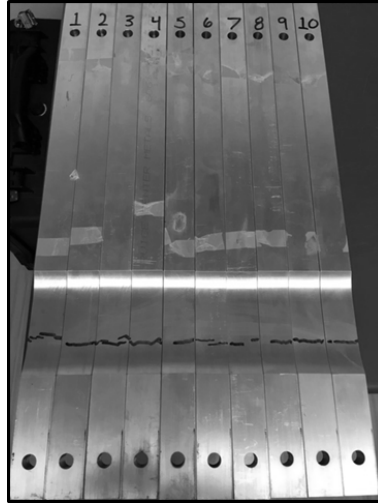
Figure 4.11: The location and size of macroscopic cracks at failure are highlighted for all ten (10) cantilevers.

gorithm. The estimated damage index is tracked in near-real time along with its uncertainty which is presented in Fig. 4.12. A deterministic S-N curve is used based on the mean value of the stress failure cycles. At the point that the upper bound of the uncertainty interval reaches one (1) the estimated index is determined. This is the point in which the experiment should be stopped to prevent failure. In two cases (2 and 3) the uncertainty bounds never reach one (1). For all other cases the experiment should be stopped at an index between 0.80 and 0.90 although this might not provide ample time before remediation.

Therefore it is essential to include both the uncertainty of the estimated stresses and the uncertainty in the S-N curve fatigue parameters to minimize the risk of material failure prior to maintenance. The associated risk is directly related to the quantification of uncertainty in both state estimation and material properties. If the uncertainty in the S-N curve parameters are not included the extent of fatigue damage is underestimated which is not representative of real-world applications as
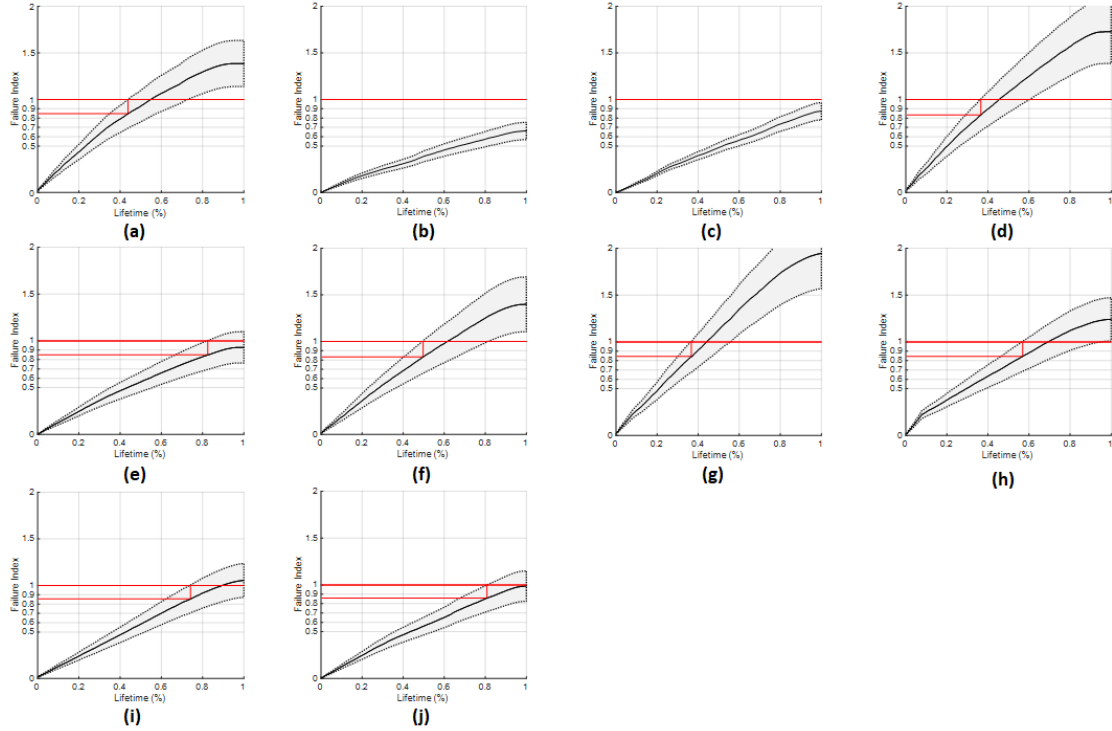
Figure 4.12: Estimated damage index and its uncertainty tracked in near-real time for each cantilever beam. Included is the probability of failure. (a-g) correspond to test cases (1-10)

seen throughout this experiment.

Two methods are proposed for this framework. Both take advantage of defining the S-N curve parameters; K,b as jointly Gaussian random variables. For method one Monte-Carlo simulations were performed by realizing 500 S-N curves for each test case which were used along with the estimated stresses to quantify an estimated index. The uncertainty bounds were then chosen based on the variance in the fatigue indices realized. The downside of this method is that it can't be performed in near-real time, therefore the authors propose an offline method that can be performed a priori.

For method two, realizations of K and b are realized as jointly Gaussian random variables, based on Eq. 16. The parameter K, was realized with a a mean of 20.68

and a variance of 0.10. The parameter b, was realized with a mean of 67.84 and a variance of 0.10 with a cross-correlation of 0.95. Empirical values were taken from the MIL-HDBK-5H: Metallic Materials and Elements for Aerospace Vehicle Structures handbook. An ellipse is then drawn around the data based on the variance in the semi-major and semi-minor axes. The percent of realizations that fall within the ellipse will define our confidence in the estimate of the material's fatigue parameters. Maxima and minima of the semi-major axis are then chosen as the parameters for the S-N curve that will determine the uncertainty bounds of the estimated damage index. This allows near-real time tracking of the damage index since the estimated stress time histories are directly used in three probabilistic S-N curves that are defined based on confidence intervals and material properties. The two methods are presented in Fig. 4.13.
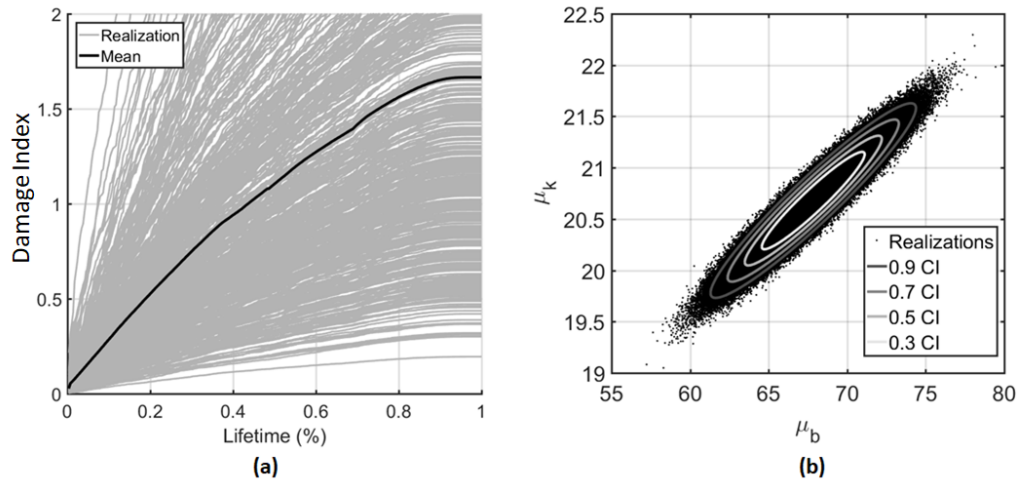
Figure 4.13: (a) Monte-Carlo like method to determine uncertainty in damage index (b) Offline method to determine confidence interval of fatigue material properties of S-N curve.

The second method was used due to its ability to track in near-real time. Four (4) different confidence intervals for the S-N curve parameters are presented which

include 0.30, 0.50, 0.70, and 0.90. The corresponding semi-major b parameters are 71.08, 72.12, 73.22, and 74.26 with semi-major K parameters of 21.15, 21.31, 21.46, and 21.62 respectively. The semi-minor b parameters are 64.6, 63.57, 62.40 and 61.36 with semi-minor K parameters 20.22, 20.06, 19.91, and 19.76 respectively. Depending on the choice of pseudo-confidence intervals a stopping criteria can be determined for all ten (10) test cases which is presented in Fig 4.14. When the estimated index reaches 0.60 the experiment should be stopped to prevent failure which allows for remediation.
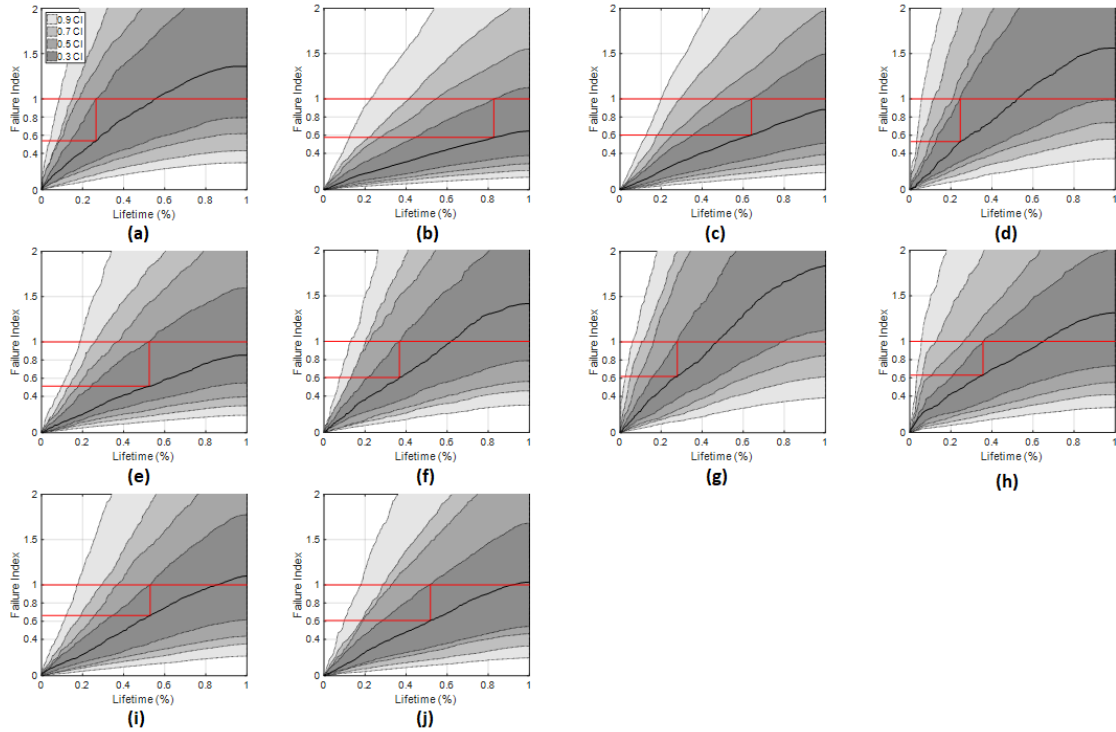
Figure 4.14: Estimated damage index and its uncertainty tracked in near-real time for each cantilever beam. Included is the probability of failure. (a-g) correspond to test cases (1-10)

The estimated indices for all the test cases are considered, Fig. 4.15(a), and at an index of 0.60 none of the specimens have failed when using the empirical S-N curve.

This is presented alongside the estimated probability of failure from 500 realizations of the S-N curve with varying fatigue damage index thresholds, Fig. 4.15(b). By choosing the damage index threshold at 0.60 the average probability of failure is 0.156. Depending on the allowable probability of failure for any system a varying failure index thresholds can be chosen by the user.
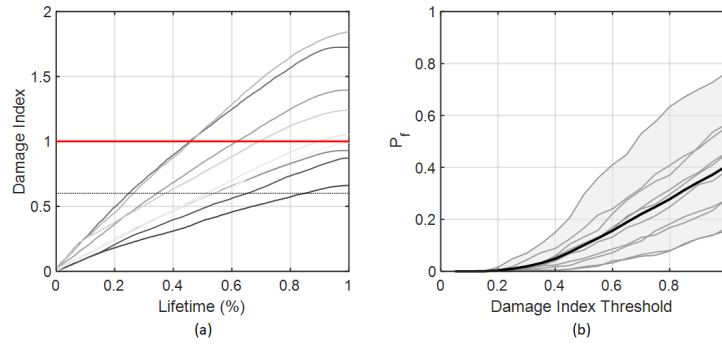
Figure 4.15: (a) Estimated damage index tracked in near-real time for all cantilever beams. (b) The probability of failure based on varying damage index thresholds for all cantilever beams.

Traditionally for vibration-based damage detection small changes in the physical properties, (mass, damping, and stiffness) can cause measurable changes in the dynamic properties of the system, for example changes in natural frequencies, modal damping, and mode shapes. The authors are presenting that for certain systems these changes aren't seen until the remaining useful life is small and often macroscopic cracks have already formed. Therefore it is desirable to monitor fatigue throughout the structures life rather than search for changes in the dynamic properties. Presented in Fig. 4.16, the average damage index is compared against the average natural response frequency which shows that at a damage index of 0.6 there isn't quantifiable changes in the system response frequency. When measurable changes are seen, the remaining fatigue lifetime is less than 10% on average.

120
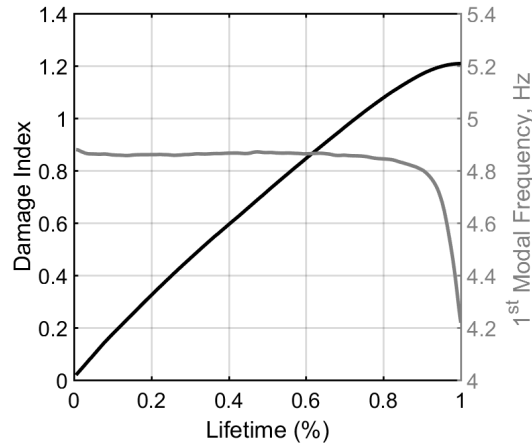
Figure 4.16: The average damage index, left axis, is compared against the average natural response frequency, right axis, throughout the lifetime of all the cantilevers. As the damage index accumulates in time the natural response frequency remains constant for 90% of the structures lifetime

4.6 CONCLUSIONS

This paper presents the results from laboratory experiments aimed at validating a probabilistic near-real time fatigue damage tracking methodology. The study was conducted using ten (10) instrumented 6061-T6 aluminum cantilever beams subject to non-periodic excitation. The methodology is composed of two steps: First, global response measurements are used to estimate stresses at fatigue critical locations of the structure, this step is carried out using a Kalman filter. Second, estimated stress cycles are counted along with an S-N curve to estimate a failure index and its uncertainty. The uncertainty quantification method used is formulated based on model error and the uncertainty in the S-N curve parameters.

Based on probabilistic numerical simulations and the results from the laboratory experiments a stopping criteria of 0.60 for the damage index is proposed. However,

the authors are not claiming that this stopping criteria is universal for other systems but rather that the proposed framework can help to determine an optimal stopping criteria based on an allowable probability of failure. This is contrast to the traditional approach to detect and quantify damage by interrogating changes in vibration characteristics such as natural frequency and mode shapes. As can be seen in Fig. 4.16 by the time vibration changes are apparent the remaining useful life has already been greatly spent even if macroscopic cracks are not visible. The proposed framework can help engineers design optimal maintenance procedures intended to prevent catastrophic fatigue failures while the system is in operation.

References

[Azam et al.; 2015] Azam, SR. Chatzi, E. Papadimitriou, C. (2015). A dual kalman filter approach for state estimation via output-only acceleration measurements. *Mechanical Systems and Signal Processing.* 60(61):866-886.

[Downing; 2012] Downing, NE. (2012). *Mechanical behavior of materials: engineering methods for deformation, fracture, and fatigue.* 4th ed. Pearson: Boston, MA.

[Erazo & Hernandez; 2014] Erazo, K. Hernandez, EM. (2014). A model-based observer for state and stress estimation in structural and mechanical systems: Experimental validation. *Mechanical Systems and Signal Processing.* 43(1):141-152.

[Gagg & Lewis; 2009] Gagg, CR. Lewis, PR. (2009). In-service fatigue failure of engineered products and structures - case study review. *Engineering Failure Analysis.* 16(6):1775-1793.

[Gelb; 1996] Gelb, A. (1996). *Applied Optimal Estimation.* 14th ed. MIT Press: Cambridge, MA.

[Giagopoulos et al.; 2019] Giagopoulos, D. Arailopoulos, A. Dertimanis, V. Papadimitriou, C. Chatzi, E. Grompanopoulos, K. (2018). Structural health monitoring and fatigue damage estimation using vibration measurements and finite element model updating. *Structural Health Monitoring* . 18(4):1189-1206.

[Gobbato et al.; 2012] Gobbato, M. Conte, JP. Kosmatka, JB. Farrar, CR. (2012). A reliability-based framework for fatigue damage prognosis of composite aircraft structures. *Probabilistic Engineering Mechanics.* 29:176-188.

[Gobbato et al.; 2014] Gobbato, M. Kosmatka, JB. Conte, JP. (2014). A recursive bayesian approach for fatigue damage prognosis: An experimental validation at the

reliability component level. *Mechanical Systems and Signal Processing.* 45(2):448-467.

[Hernandez; 2011] Hernandez, EM. (2011). A natural observer for optimal state estimation in second order linear structural systems. *Mechanical Systems and Signal Processing.* 25(8):2938-2947.

[Juvinall & Marshek; 2012] Juvinall, R.C. Marshek, KM. (2012). *Fundamentals of Machine Component Design.* 5th ed. Wiley: Hoboken, NJ.

[Kalman; 1960] Kalman, R. (1960). A new approach to linear filtering and prediction problems. *Transactions of the ASME Series D, Journal of Basic Engineering.* 82(1):35-45.

[Miner; 1945] Miner, M. (1945). Cumulative damage in fatigue *ASME Applied Mechanics Transactions.* 159-164.

[Palanisamy et al.; 2015] Palanisamy, R. Cho, S. Kim, H. Sim, SH. (2015). Experimental validation of Kalman filter-based strain estimation in structures subjected to non-zero mean input. *Smart Structures and Systems.* 15(2), 489-503.

[Papadimitriou et al.; 2011] Papadimitriou, C. Fritzen, CP. Kraemer, P. Ntotsios, E. (2011). Fatigue predictions in entire body of metallic structures from a limited number of vibration sensors using kalman filtering. *Structural Control and Health Monitoring.* 18(5):554-573.

[Schijve; 2003] Schijve, J. (2013). Fatigue of structures and materials in the 20th century and the state of the art. *International Journal of Fatigue.* 25(8):679-702.

[Schijve; 2005] Schijve, J. (2005). Statistical distribution functions and fatigue of structures. *International Journal of Fatigue.* 27:1031-1039.

[Shen et al.; 2000] Shen, H. Lin, J. Mu, E. (2000). Probabilistic model on stochastic fatigue damage. *International Journal of Fatigue.* 22:569-572.

[Simon; 2006] Simon, D. (2006). *Optimal State Estimation.* Wiley and Sons: New York, NY.

[Sobczyk & Spencer; 1991] Sobczyk, K. Spencer, BF. (1991). *Random Fatigue: From Data to Theory.* Academic Press, New York.

CHAPTER 5

ESTIMATING GROUND REACTION FORCE WITHIN A MECHANICAL FATIGUE FRAMEWORK: AN APPLICATION FOR HIGH MILEAGE RUNNERS

5.1 ABSTRACT

Estimation of ground reaction forces in runners has been limited to laboratory environments by means of instrumented treadmills and optoelectronic systems. Recent advances in estimation techniques using wearable sensors for kinematic analysis and sports performance could enable estimation outside the laboratory. This paper proposes a state-input-parameter estimation framework to estimate the vertical ground reaction force in near real time using a dual-Kalman filter to estimate

the unmeasured input in combination with an unscented Kalman filter to estimate the state and uncertain model parameters (i.e. leg stiffness). The model is a single degree of freedom spring-mass-damper with acceleration measurements at the sacrum. For validation, 14 subjects performed three one-minute running trials at three different speeds (self-selected slow, comfortable, and fast) on a pressure-sensor-instrumented treadmill. The estimated vertical ground reaction force waveform parameters; peak vertical ground reaction force (RMSE $= 6.1\% - 7.2\%$, $\rho = 0.95 - 0.97$), vertical impulse (RMSE $= 8.5\% - 13.0\%$, $\rho = 0.50 - 0.60$), loading rate (RMSE $= 24.6\% - 39.4\%$, $\rho = 0.85 - 0.93$), and cadence (RMSE $=< 1\%$, $\rho = 1.00$) were compared against the instrumented treadmill measurements. The proposed algorithm provides excellent agreement in near-real time using minimal instrumentation while having the ability to automatically personalize to the user without the need for prior training data.

5.2 INTRODUCTION

Fatigue damage is defined as the continuous degradation of a material, often due to the formation of microcracks or tears from applied cyclic stresses. Fatigue is a complex and random process that effects engineering structures, such as aircrafts, bridges, trains, etc. but also impacts biological systems. The accumulation of repetitive loading in biological tissue often leads to overuse injuries (Hreljac, 2005; Stanish, 1984), where the structural damage and biomechanical failure is consistent with the process of mechanical fatigue (Edwards, 2018). Running, a popular physical activity for maintaining health and wellness, is often associated with high risk of overuse

injury. The ground reaction forces (GRF) experienced during running place the musculoskeletal system under high biomechanical stresses that can either lead to beneficial structural adaptations such as increased bone density and leg stiffness or negative adaptations such as overuse injuries at the tissue or skeletal level (Kibler et al., 1992; Dye, 2005; Burr et al., 1985; Chamay & Tschantz, 1972). Although no exact values are available, it has been estimated that upwards of 80% of runners will obtain a running related injury (RRI) each year. Like structural fatigue damage, RRI's often come with associated economic and performance costs (Hespanhol Junior et al. 2016).

High mileage runners, defined as anyone who runs more than 40 miles per week (or $\sim$50,000+ steps), are often at an increased risk of RRI's due to the large number of stress cycles experienced. This is exacerbated by the shortened recovery period between running sessions (Macera et al., 1989). Stress cycles are often characterized by parameters derived from the vertical GRF (vGRF) waveform. Traditionally, vGRF waveforms have been monitored by force instrumented treadmills or derived from whole-body kinematics from optoelectronic systems (OS) within a laboratory environment (Bobbert et al., 1991; Winter, 2005). Although this results in high accuracy, reliability and repeatability; laboratory-based technologies do not enable continuous athlete monitoring and may not reflect running conditions prevalent outside of the laboratory setting such as running on uneven surfaces or surfaces of different stiffness (Sinclair et al., 2013; Alton et al., 1998). A preferable approach would be to monitor vGRF indirectly using a global measurement of vibration recorded by wearable technologies (Abdul Razak et al., 2012). These technologies include pressure-sensitive insoles, wearable load cells, and/or inertial measurement units (IMU). During typical

running conditions it is not practical, or cost-effective, to use an extensive network of sensors like those found in traditional biomechanics laboratory settings, and thus minimal wearable instrumentation that is still able to resolve vGRF is desired.

The vGRF waveform has been extensively studied for human runners (Cavanagh, 1987) and several models can describe it accurately (Chi & Schmitt, 2005; Clark et al., 2014; Derrick, 2004; Lieberman et al., 2010; Nigg, 2010). A mass-spring-damper (MSD) model is commonly used to model the vGRF waveform. Some of these models require the specification of 14 or more input parameters to perform the forward dynamics simulation (Chi & Schmitt, 2005; Liu & Nigg, 2000; Ly et al., 2010; Nigg & Liu, 1999; Nikooyan & Zadpoor, 2011). These parameters are typically determined within a laboratory setting and often require a constant running speed. Direct modelling requires subject-specific parameters such as masses, dimensions, and/or mechanical properties such as stiffness and damping in order to accurately estimate vGRF. Methods that employ either physical or statistical models (artificial neural networks, orthogonal forward regression, etc.) for estimating vGRF from wearable accelerometer data recorded at the thigh, shank, iliac crest, medial tibia, upper back, or sacrum have previously been validated (Ohtaki et al., 2001; Neugebauer et al., 2014; Wundersitz et al., 2013; Gurchiek et al., 2017; Raper et al., 2018). Although statistical models for estimation of vGRF have been successful they are often dependent on training data and multiple sensors (Guo et al., 2017; Wouda et al., 2017). These methods are often subject to sub-optimal performance when training data isn't representative of measured data. Rather this paper proposes an alternative data-model fusion approach that uses structural models combined with state estimation algorithms with minimal instrumentation to update model parameters in near-real time

to automatically personalize to the user.

State estimation aims to reconstruct the state of a dynamical system from noisy observations of its response and a model (Gelb 1987). The Kalman filter has been shown to be an effective tool to estimate the unmeasured response in structural/mechanical systems (Palanisamy et al., 2015; Waller & Schmitt, 1990). A fundamental assumption of the Kalman filter is that the unmeasured inputs are realizations of a Gaussian random process, this condition is often relaxed. However, a dual-Kalman filter approach can be used to estimate both the state and the unmeasured input in order to improve the accuracy (Azam et al., 2015). An unscented Kalman filter can then be implemented to estimate the state and uncertain model parameters. This is well suited for monitoring vGRF due to the uncertainty in biomechanical parameters, i.e. leg stiffness, that are influenced by fatigue, structural adaptation, running surface and shoe choice (Mizrahi et al., 2000; Morin et al., 2011; Kerdok et al., 2002).

The purpose of this study is to formulate a state-input-parameter estimation framework to estimate the vGRF of a runner in near-real time. The methodology is tested using an instrumented treadmill with acceleration measurements at the sacrum. This model-data fusion method could provide novel insight concerning the identification and effects of mechanical fatigue during high mileage running in non-laboratory running conditions.

5.3   METHODS

5.3.1   MSD MODEL

The single-body model has been used to describe the active peak of the vGRF during impact (Blickhan, 1989), while the two-body model is the simplest multi-body model that can determine the impact and active peaks at stance phase, allowing for the ability to study both fore-foot and heel strike running (Mizrahi & Susak, 1982; Nevzat Ozguiven & Berme, 1988). In order to implement the desired estimation in near-real time it is necessary to limit the required estimation parameters for a SDOF MSD model (see Fig. 5.1). Although this choice improves implementation it could restrict the ability to capture the entire vGRF waveform during heel strike.
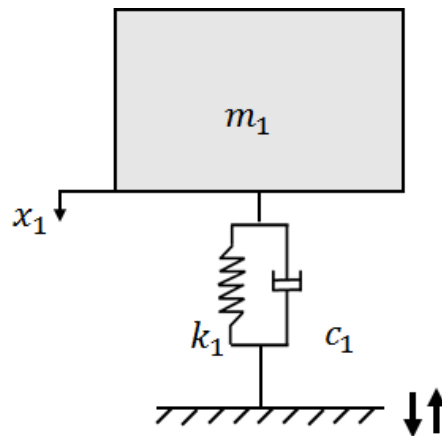
Figure 5.1: A single-body model capable of estimating vGRF during impact which was originally used to estimate vGRF during jumping.

5.3.2 Equations of motion

The equation of motion for the model introduced in Fig. 5.1 can be expressed as

$$\mathbf{M}\ddot{q}(t) + \mathbf{C_d}\dot{q}(t) + \mathbf{K}(\theta)q(t) = \mathbf{b_2}u(t) \tag{5.1}$$

where $q(t) \in \mathbb{R}^{nx1}$ is the displacement vector at time t. The matrices $\mathbf{M}$, $\mathbf{C_D}$ and $\mathbf{K}(\theta)$ are the mass, damping and stiffness matrices, which are different for each runner. This structural system is uncertain because the stiffness matrix depends on the parameter vector $\theta \in \mathbb{R}^{dx1}$, which is unknown a priori. The unknown input term is $u(t) \in \mathbb{R}^{1xn}$, and $\mathbf{b_2} \in \mathbb{R}^{nx1}$ is the input distribution matrix vector. The absolute acceleration measurements of the system's response are defined by

$$y(t) = -\mathbf{c_2}\mathbf{M}^{-1}\mathbf{K}(\theta)q(t) - \mathbf{c_2}\mathbf{M}^{-1}\mathbf{C_D}\dot{q}(t) - \mathbf{c_2}\mathbf{M}^{-1}\mathbf{b_2}u(t) + r(t) \tag{5.2}$$

where $\mathbf{c_2} \in \mathbb{R}^{mxn}$ maps the degrees of freedom to the measurements and $r(t) \in \mathbb{R}^{mx1}$ is the measurement noise. A Newtonian method is considered for comparison. The method uses a single inertial measurement unit at a location assumed to represent the motion of the COM (i.e. sacrum) thus enabling an estimate of the vGRF via Newton's second law of motion as per,

$$F(t) = \mathbf{M}\ddot{a} \tag{5.3}$$

where $\ddot{a}$ is the net sacral acceleration. A sacrum-worn accelerometer measures the specific force, $\ddot{a} + g$, which is first lowpass filtered at the approximate step frequency

before the estimate of vGRF, eq. (5.3). This method has been used for estimation of vertical loading during walking (Bocian et al., 2016).

5.3.3   STATE-INPUT-PARAMETER ESTIMATION PROCESS

An observer is a dynamical system driven by the measurements and whose state is an estimate of the system of interest. In the case of a linear second order structural system, the state vector corresponds to the displacement and velocity of all degrees of freedom, $x_k = [q \quad \dot{q}]^T$. A dual observer was proposed by Dertimanis et al., which combines the dual and unscented Kalman filter (UKF) for state-input-parameter estimation. The observer was originally used for structural systems subject to Gaussian input. The dual Kalman filter (DKF) determines the unknown structural input while the UKF solves the state and parameter estimation by means of an augmented state-space formulation. For brevity only the fundamental equations necessary for implementation are presented. For a full derivation refer to Dertimanis et al. The derivation begins by introducing two auxiliary state equations

$$uk + 1 = \mathbf{T}u_k + w_k^u \tag{5.4}$$

$$\theta_{k+1} = \theta_k + w_k^u \tag{5.5}$$

where $\mathbf{T}$ is a matrix and w_k^u, w_k^θ are zero mean Gaussian processes with covariance matrices Q_{uu} and $Q_{\theta\theta}$, respectively. The augmented state vector is defined as $z_k = [x_k, \quad \theta_k]^T \in \mathbb{R}^{\bar{n}x1}$, for $\bar{n} = 2n + d$, in which the new augmented state-space model is

formulated as

$$z_{k+1} = \begin{bmatrix} \mathbf{A} & \mathbf{0} \\ \mathbf{0} & \mathbf{I} \end{bmatrix} z_k + \begin{bmatrix} \mathbf{B} \\ \mathbf{0} \end{bmatrix} u_k + \begin{bmatrix} \mathbf{w_k^x} \\ \mathbf{w_k^\theta} \end{bmatrix} = f(z_k, u_k) + p_k \tag{5.6}$$

$$y_{k+1} = \begin{bmatrix} \mathbf{C} & \mathbf{0} \end{bmatrix} z_k + \begin{bmatrix} \mathbf{D} \end{bmatrix} u_k + r_k = g(z_k, u_k) + r_k \tag{5.7}$$

where $\mathbf{A}$ is the state transition matrix, $\mathbf{B}$ is the input matrix, $\mathbf{C}$ is the measurement matrix, $\mathbf{D}$ is the direct transmission matrix and w_k^x is uncorrelated with w_k^θ. The process noise in the augmented state equation is denoted as p_k which again has zero mean and covariance matrix $Q_{pp} = diag\{Q_{xx}, Q_{\theta\theta}\}$. The measurement error is a zero mean Gaussian measurement noise denoted as r_k with a covariance matrix R.

5.3.4 PARTICIPANTS

Data from 14 subjects (8 female, mass [mean $\pm$ SD]: 75.02 ± 12.78 kg, height: 1.74 ± 0.08 m, age: 23.50 ± 6.10 y.o.), recruited as part of a larger study, were used to validate the proposed vGRF estimation algorithm. All subjects provided written consent to participate. This study was approved by the University of Vermont Institutional Review Board.

5.3.5 EXPERIMENTAL PROCEDURE

Each subject wore an inertial sensor (Opal v2, APDM, Inc.) positioned over the sacrum and securely attached using an elastic strap around the waist and double-sided tape. As part of the larger study inertial sensors were also placed on the

sternum, thigh, tibia, and foot. Only a subset of the inertial sensors, namely at the foot, were used for time synchronization. Herein, we use only the data from the on-board accelerometer (128 Hz, range: ±16 g). Following a static standing calibration trial, subjects performed three one-minute running trials at three different speeds (self-selected slow, comfortable, and fast) on a pressure-sensor-instrumented treadmill (h/p/cosmos quasar, 100 Hz).

5.3.6 DATA ANALYSIS

Accelerometer-based estimates of vGRF were informed by data from the sensor's axis most closely aligned with the subject's cranial-caudal anatomical axis. This axis may not align directly with the vertical axis of the instrumented treadmill, and thus remains a potential source of error in the reported results. Gravity was removed from the data by subtracting the best straight-fit line from the raw accelerometer data. Accelerometer-based vGRF estimates were down sampled to 100 Hz via linear interpolation for comparison to the treadmill data. The accelerometers and treadmill were time-synchronized using cross-correlation of the foot acceleration at ground contact.

5.3.7 ALGORITHM FORMULATION

The input noise covariance matrix (Q_{uu}, eq. 5.4), the measurement noise covariance (R, eq. 5.7), the augmented process noise covariance matrix (Q_{pp}, eq. 5.6) and the auxiliary state transition matrix ($\mathbf{T}$, eq. 5.4) need to be defined in order to formulate the state-input-parameter estimation algorithm. The input noise covariance was set to $1x10^7$ N , which is the Newtonian forcing variance for all participants. The

measurement noise covariance for the sacrum accelerometer was 0.01 m/s^2. The augmented process noise covariance matrix had two formulations because the estimation error appeared to be subject-specific and thus subjects were divided into two groups based on the root-mean-square error (RMSE) of the vGRF estimation for each individual. At first the augmented process noise covariance was set to the diagonal matrix $[1x10^{-4}$ m, $1x10^{-4}$ m/s , $1x10^{-3}$ N/m] for all participants. This resulted in four subjects (group one) having large RMSE (> 0.30) for all test cases therefore the augmented process noise covariance was decreased to $[1x10^{-5}$ m, $1x10^{-5}$ m/s, $1x10^{-3}$ N/m]. The remaining ten participants (RMSE < 0.30) were placed in group two. The initial augmented state stiffness parameter was set to 20 kN and the states were set to zero. The auxiliary state transition matrix (in this case a scalar) was set to 0.96.

5.3.8   STATISTICAL ANALYSIS

The estimation accuracy of the model was assessed for all the individual footfalls acquired using the RMSE statistic, which quantifies the goodness of fit in absolute terms. This approach is common for quantifying the degree of overlap in time-series data (Clark et al., 2014; Gurchiek et al., 2017). The total number of footfalls, 100-200 per test, were sufficiently large to detect small changes in algorithm performance across speeds using RMSE statistics.

Model performance was further established by considering the Spearman rank correlation coefficient between several parameters often used to characterize the vGRF signal (peak vGRF, vertical impulse, loading rate, and cadence) as predicted by the model and as extracted from the ground-truth vGRF signal provided by the treadmill.

Peak vGRF was determined by finding the maximum value of the vGRF waveform for each step. Vertical impulse was determined by integrating the vGRF during foot contact. Loading rate was determined by finding the slope of the vGRF until 40% of stance phase or until the active peak was visible, if there was one (Matijevich et al., 2019). Cadence was determined by the average time difference between consecutive steps.

5.4 RESULTS

Estimated model parameters are presented in Table 5.1. Running speed was user defined which allowed for treadmill speed to overlap between test cases. The treadmill speed increased by at least 1 m/s throughout the testing procedure for each participant. Leg stiffness, estimated through the augmented state vector, increased through the running tasks from 11.98 ± 2.59 kN to 13.56 ± 3.81 kN with the largest increase from slow to comfortable. The damping parameter was chosen to fit the data, but the damping ratio was consistent across cases and participants, at 16 percent of critical. The estimated stiffness value was used to define the critical damping value.

Table 5.1: Treadmill speed and SDOF Model Parameters including estimated stiffness ($\mathbf{k_1}$), damping ($\mathbf{c_1}$), and corresponding damping ratio (ξ) for each test case

Test	Run Speed (m/s)	k_1 (kN/m)	c_1 (Ns/m)	ξ (damp. ratio)
Slow	1.62 ± 0.22	11.98 ± 2.59	291.43 ± 80.81	0.16 ± 0.04
Comfortable	2.13 ± 0.42	13.05 ± 3.23	300.00 ± 66.14	0.16 ± 0.04
Fast	2.74 ± 0.71	13.56 ± 3.81	318.57 ± 71.25	0.16 ± 0.03

The uncertain stiffness parameter converged within 30 seconds for the case presented in Fig. 5.2. The initial stiffness parameter began at 20 kN and converged within 60 seconds for all cases but the rate is dependent on the damping parameter.

The variance of the parameter estimation is also presented.
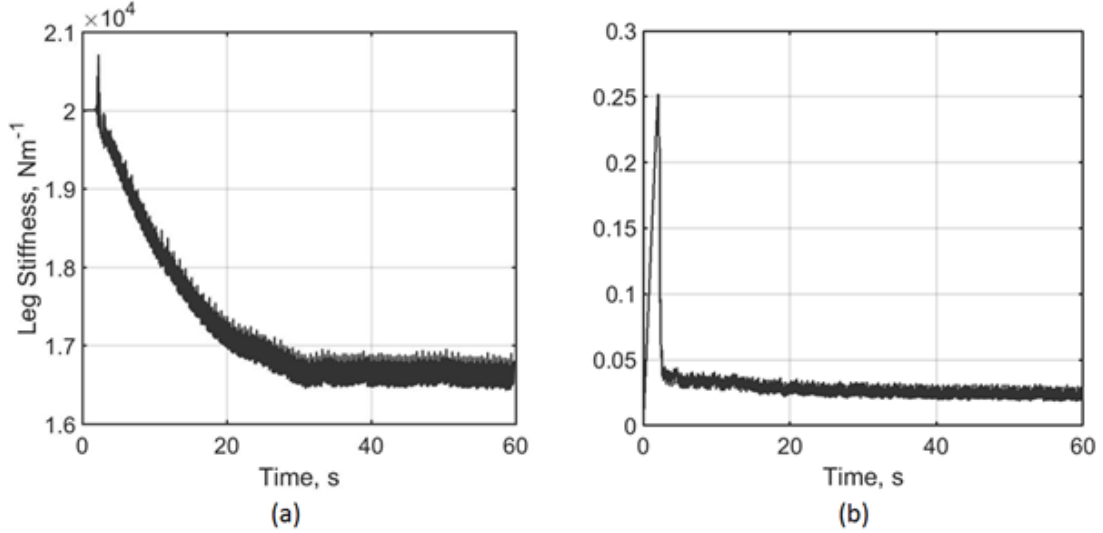
Figure 5.2: The convergence of the (a) uncertain stiffness parameter and its (b) variance estimate.

The estimated vGRF is compared against the vGRF measured from the instrumented treadmill and the Newtonian method (Eq. 5.3). The Newtonian method provides a baseline reference for the proposed algorithm. The frequency of the vGRF is matched when viewing 30 strides and the magnitude is comparable when zoomed into four steps (see Fig. 5.3). The RMSE for the Newtonian method is an order of magnitude higher than our method. For this case, the RMSE of the proposed algorithm is 0.14 BW and the Newtonian method is 2.68 BW. During the flight phase the proposed algorithm and Newtonian method estimate a negative vGRF at roughly -1 BW. For the remainder of the paper the flight phase is set to zero for clarity of comparison.

Uncertainty in the estimated vGRF is quantified by the variance of the states from the state-input-parameter estimation process. A one standard deviation confidence

Figure 5.3: The pressure-sensor-instrumented treadmill vGRF (black) compared against the estimated vGRF (blue) from the input-parameter-state estimation algorithm and a low pass Newtonian method (red). (a) Provides ten seconds of analysis, (b) zoomed in portion of the ten second analysis.

interval is plotted with the estimate, which shows that the true vGRF is within the confidence bounds for most steps, Fig. 5.4.

All the steps for each participant are overlaid with the vGRFs from the instrumented treadmill and the estimated vGRFs, Fig. 5.5. The algorithm is conservative in its estimate but consistently monitors the vGRF for all participants throughout the three running tasks.

The average and standard deviation of the peak vGRF, vertical impulse, loading rate and cadence across all participants are presented in Table 5.2. The measured and estimated peak vGRF (2.68 ± 0.36 to 3.14 ± 0.32 BW), loading rate (18.58 ± 5.90 to 30.75 ± 7.38 BW/s) and cadence (146.81 ± 7.67 to 161.39 ± 11.74 steps/min) increase with increasing speed, while the vertical impulse remains constant (0.48 ± 0.04 BWs).

Table 5.3 presents each participant's RMSE (group one in bold) for the peak
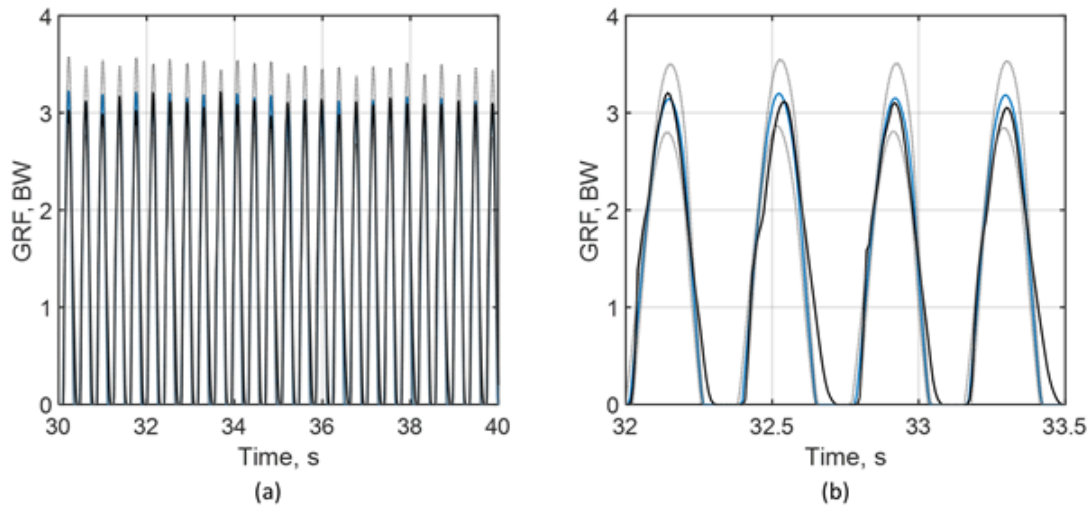
Figure 5.4: The pressure-sensor-instrumented treadmill vGRF (black) compared against the estimated vGRF (blue) from the input-parameter-state estimation algorithm and its uncertainty. (a) Provides ten seconds of analysis, (b) zoomed in portion of the ten second analysis.

Table 5.2: The mean and standard deviation of the vGRF waveform parameters from the pressure-sensor-instrumented treadmill and the proposed algorithm

Parameters	Slow	Comfortable	Fast
Peak vGRF (BW)	2.63 ± 0.34	2.96 ± 0.32	3.10 ± 0.34
Estimated Peak vGRF	2.68 ± 0.36	2.97 ± 0.32	3.14 ± 0.32
Vertical Impulse (BWs)	0.54 ± 0.06	0.51 ± 0.05	0.47 ± 0.04
Estimated Vertical Impulse	0.48 ± 0.048	0.48 ± 0.04	0.47 ± 0.04
Loading Rate (BW/s)	22.85 ± 7.17	33.80 ± 11.48	45.95 ± 17.05
Estimated Loading Rate	18.58 ± 5.90	24.72 ± 5.18	30.75 ± 7.38
Cadence (steps/min)	146.83 ± 7.64	154.96 ± 8.85	161.24 ± 11.59
Estimated Cadence	146.81 ± 7.67	154.93 ± 8.88	161.39 ± 11.74

vGRF, vertical impulse, loading rate and cadence as well as the correlation between these parameters as derived from the model-predicted, and treadmill-measured, vGRF during comfortable running. The correlation for peak vGRF, loading rate, and cadence are close to one; while vertical impulse has a low correlation factor. RMSE was calculated by re-running the simulation with the mean estimated stiffness after convergence from the original estimation process. Estimation errors are quantified by
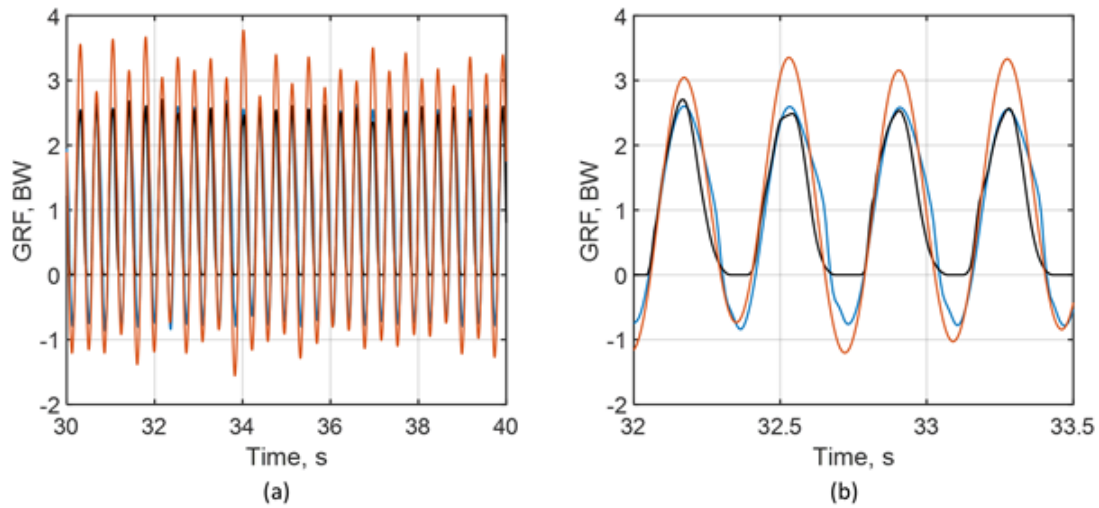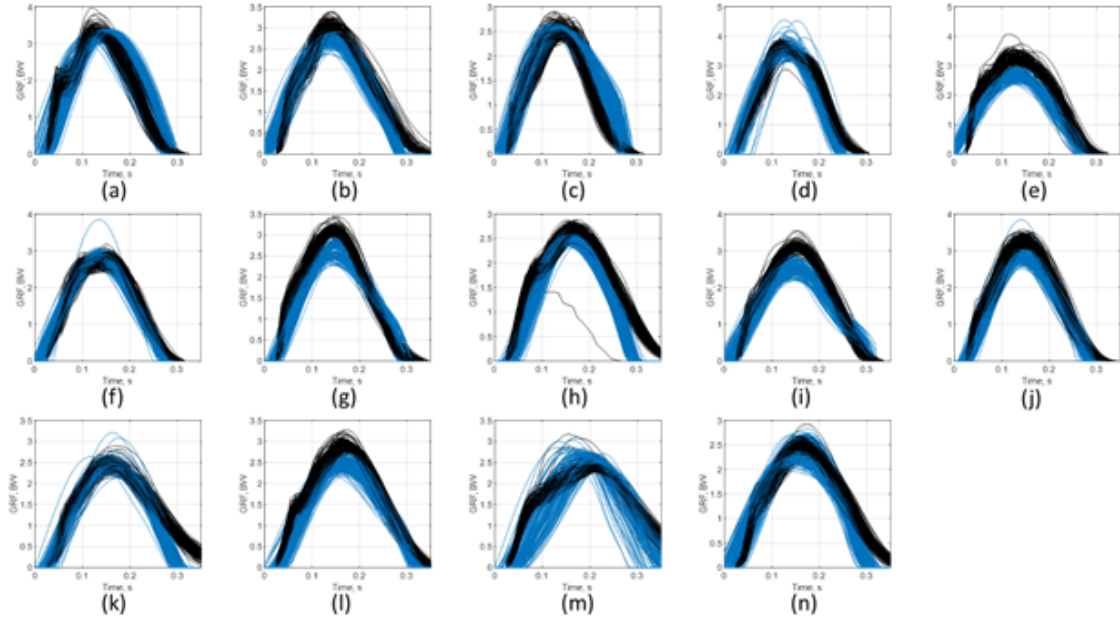
Figure 5.5: The pressure-sensor-instrumented treadmill vGRF (black) compared against the estimated vGRF (blue) from the input-parameter-state estimation algorithm overlaid. (a-n) Each participant running comfortable.

average RMSE in Table 5.4. The peak vGRF RMSE was similar across tests with a value of 0.19 ± 0.04 BW at slow speed to 0.19 ± 0.05 BW at fast speed. The vertical impulse had the largest RMSE for the slow case at a value of 0.07 ± 0.04 BWs, while the loading rate had high error across all test cases due to the model's inability to determine the impact peak. The error values ranged from 5.62 ± 2.69 to 18.12 ± 12.31 BW/s. The algorithm successfully estimated the correct cadence.

5.5   DISCUSSION

The state-input-parameter estimation filter derived by Dertimanis et al. had only been tested in simulation. The algorithm was originally used for structural/mechan-

Table 5.3: *RMSE for vGRF parameters during comfortable running for each participant. The corresponding Spearman rank correlation is presented across participants. Bolded numbers indicate members of group one.*

Participant	Peak vGRF (BW)	Vertical Impulse (BWs)	Loading rate (BW/s)	Cadence (steps/min)
1	0.16	0.04	34.00	0.00
2	0.14	0.02	8.64	0.06
3	**0.11**	**0.05**	**7.44**	**0.05**
4	0.17	0.07	17.33	0.02
5	0.21	0.06	19.07	0.02
6	**0.18**	**0.02**	**19.68**	**0.07**
7	0.14	0.03	7.00	0.07
8	**0.23**	**0.11**	**5.21**	**0.14**
9	0.19	0.03	14.19	0.02
10	0.21	0.02	6.82	0.16
11	**0.12**	**0.06**	**5.28**	**0.04**
12	0.20	0.03	5.20	0.26
13	0.20	0.10	3.48	0.08
14	0.28	0.04	4.99	0.13
Correlation	**0.95**	**0.50**	**0.85**	**1.00**

Table 5.4: *Average RMSE and standard deviation for vGRF parameters for each test case.*

Participant	Peak vGRF (BW)	Vertical Impulse (BWs)	Loading rate (BW/s)	Cadence (steps/min)
Slow	0.19 ± 0.04	0.07 ± 0.04	5.62 ± 2.69	0.18 ± 0.21
Comfortable	0.18 ± 0.04	0.05 ± 0.03	10.67 ± 7.96	0.08 ± 0.07
Fast	0.19 ± 0.05	0.04 ± 0.02	18.12 ± 12.31	0.26 ± 0.35

ical systems subject to Gaussian input. The results from this work show that the algorithm successfully estimates the unknown input, the uncertain stiffness parameter, and the states for all three running tasks using a single acceleration measurement when the system is subject to non-Gaussian input. By modeling runners as a mechanical system (i.e., MSD), a state space representation is possible, thus allowing application of the proposed estimation algorithm. The sacrum measurement provides a good estimate of the motion of the center of mass, allowing for a SDOF model to track vGRF in near real time.

The estimated input is not the vGRF but rather the force input into the equations of motion for the model to match the measurements at the sacrum. The estimated stiffness parameter is a combination of the total stiffness of the system which in-

corporates shoe choice, running technique, treadmill stiffness, and damping. This stiffness value could provide a better estimate of the parameter than a value based on measured vGRF and COM displacement.

The estimation algorithm provides a good estimate of the general waveform of the vGRF that is represented in the RMSE of the peak vGRF ($6.1\% - 7.2\%, \rho = 0.95 - 0.97$), the vertical impulse ($8.5\% - 13.0\%, \rho = 0.50 - 0.60$), the loading rate ($24.6\% - 39.4\%, \rho = 0.85 - 0.93$), and the cadence ($< 1\%, \rho = 1.00$). Shahabpoor & Pavic found a 5.6% RMSE for vGRF waveform estimation using a scaled amplitude method for walking (Shahabpoor & Pavic, 2016). Charry et al. estimated peak vGRF with a RMSE of 6.0% using only tibial accelerations within a machine learning algorithm based on individual training data (Charry et al., 2013). Shippen & May estimated vGRF using full-body optical motion capture resulting in very accurate estimations ($< 3.0\%$). Wouda et al. estimated peak vGRF with an accuracy of 3.5% and found similar loading rates using artificial neural networks (Wouda et al., 2017). Pavei et al. used a Newtonian method with double differentiation to get similar results for vertical impulse and loading rate but used a single subject. Lastly Nedergaard et al. estimated vGRF from a single accelerometer at the trunk and a machine learning algorithm resulting in higher errors than the proposed method. Therefore, the proposed algorithm simplifies the vGRF estimation problem (i.e one sensor, real-time, and no need for training data) without sacrificing performance.

The proposed method provides comparable RMSE for peak vGRF, vertical impulse, and cadence to other methods; however, the loading rate is underestimated in cases where the participant heel strikes. The proposed method estimates the loading rate as if all the participants vGRF has a single peak. The algorithm has decreased

performance as participant speed increased, which is a combination of the model not being able to capture the true dynamics and several participants changing from mid foot to heel striking. This could be corrected by adding degrees of freedom to the model (i.e. additional masses connected in series through springs and dampers) or in the choice of covariance matrices.

An important feature of the algorithm is that the process can be completed in near-real time. It is not necessary to postprocess the data since the algorithm doesn't require integration of measurements, measurement coupling, and/or measured vGRF for parameter quantification. By updating the stiffness in near real time, the ability to determine vGRF in varying terrain is possible. This could include pavement, concrete, and trail running with variable slope which isn't feasible in the laboratory setting.

However, several limitations still persist. The range of running speeds is small, the model is a SDOF, and four matrices need to be defined. The running tasks were performed at slower (< 3 m/s) and thus it is unknown how well the algorithm will perform at faster running speeds in which case estimation error may be more sensitive to body type, running technique, and soft tissue artefacts.

The four matrices outlined in section 2.7 are freely chosen based on estimator performance and/or sensor properties. The process noise covariance was increased for group two, due to increased variation in their running form. Therefore, the algorithm relied on the sensor measurements more than the system model (ratio of the noise to process covariance). Due to running being frequency dependent (non-Gaussian), the DKF-UKF algorithm provides a sub-optimal estimate of the states and uncertain parameter but is still comparable to direct measurements of vGRF.

In conclusion, the proposed state-input-parameter estimation process for measuring vGRF during running tasks in near-real time with the application for high mileage runners is experimentally validated. Minimal instrumentation and near-real time estimation point toward future use of this approach for running performance and fatigue monitoring outside the laboratory setting.

References

[Abdul Razak et al.; 2012] Abdul Razak, AH. Zayegh, A. Begg, RK. Wahab, Y. (2012). Foot plantar pressure measurement system: a review. *Sensors*. 12, 9884-9912.

[Alton et al.; 1998] Alton, F. Baldey, L. Caplan, S. Morrissey, MC. (1998). A kinematic comparison of overground treadmill walking. *Clinical Biomechanics*. 13(6), 434-440.

[Azam et al.; 2015] Azam, SE. Chatzi, EN. Papadimitriou, C. (2015). A dual kalman filter approach for state estimation via output-only acceleration measurements. *Mechanical Systems and Signal Processing*. 60(61), 866-886.

[Blickhan; 1989] Blickhan, R. (1989). The spring-mass model for running and hopping. *Journal of Biomechanics*. 22(11/12), 1217-1227.

[Bobbert et al.; 1991] Bobbert, MF. Schamhardt, HC. Nigg, BM. (1991). Calculation of vertical ground reaction force estimates during running from positional data. *Journal of Biomechanics*. 24, 1095-1105.

[Bocian et al.; 2006] Bocian, M. Brownjohn, JMW. Racic, V. Hester, D. Quattrone, A. Monnickendam, R. (2006). A framework for experimental determination of localized vertical pedestrian forces on full-scale structures using wireless attitude and heading reference systems. *Journal of Sound and Vibration*. 376, 217-243.

[Burr et al.; 1985] Burr, DB. Martin, RB. Schaffler, MB. Radin, EL. (1985). Bone remodeling in response to in-vivo fatigue microdamage. *Journal of Biomechanics*. 18(3), 189-200.

[Cavanagh; 1987] Cavanagh, PR. (1987). The biomechanics of lower extremity action in distance running. *Foot & Ankle.* 7, 197-217.

[Chamay & Tschantz; 1972] Chamay, A. Tschantz, P. (1972). Mechanical influences in bone remodeling: experimental research on Wolff's law. *Journal of Biomechanics.* 5(2), 173-180.

[Charry et al.; 2013] Charry, E. Hu, W. Umer, M. Ronchi, A. Taylor, S. (2013). Study on estimation of peak ground reaction forces using tibial accelerations in running. *IEEE Eighth International Conference on Intelligent Sensors, Sensor Networks and Information Processing.* (Melbourne, VIC), 288-293.

[Chi & Schmitt; 2005] Chi, KJ. Schmitt, D. (2005). Mechanical energy and effective foot mass during impact loading of walking and running. *Journal of Biomechanics.* 38, 1387-1395.

[Clark et al.; 2014] Clark, KP. Ryan, LJ. Weyand, PJ. (2014). Foot speed, foot-strike and footwear: linking gate mechanics and running ground reaction forces. *Journal of Experimental Biology.* 217, 2037-2040.

[Clark et al.; 2017] Clark, KP. Ryan, LJ. Weyand, PG. (2017). A general relationship links gait mechanics and running ground reaction forces. *Journal of Experimental Biology.* 220, 247-258.

[Derrick et al.; 2000] Derrick, TR. Caldwell, GE. Hamill, J. (2000). Modeling the stiffness characteristics of the human body while running with various stride lengths. *Journal of Applied Biomechanics.* 16(1), 36-51.

[Derrick; 2004] Derrick, TR. (2004). The effects of knee contact angle on impact forces and accelerations. *Medical & Science in Sports & Exercise.* 36, 832-837.

[Dertimanis et al.; 2019] Dertimanis, VK. Chatzi, EN. Azam, SE. Papadimitriou, C. (2019). Input-state-parameter estimation of structural systems from limited output information. *Mechanical Systems and Signal Processing.* 126, 711-746.

[Dye; 2005] Dye, SF. (2005). The pathophysiology of patellofemoral pain: a tissue homeostasis perspective. *Clinical Orthopaedics and Related Research.* 436, 100-110.

[Edwards; 2018] Edwards, WB. (2018). Modeling overuse injuries in sport as a mechanical fatigue phenomenon. *Exercise and Sport Sciences Reviews.* 46(4), 224-231.

[Gelb; 1987] Gelb, A. (1987). *Applied Optimal Estimation.* MIT Press, Cambridge, MA.

[Guo et al.; 2017] Guo, Y. Storm, F. Zhao, Y. Billings, S. Pavic, A. Mazza, C. Guo, LZ. (2017). A new proxy measurement algorithm with application to the estimation of vertical ground reaction forces using wearable sensors. *Sensors.* 17, e2181

[Gurchiek et al.; 2017] Gurchiek, RD. McGinnis, RS. Needle, AR. McBride, JM. van Werkhoven, H. (2017). The use of a single inertial sensor to estimate 3-dimensional ground reaction force during accelerative running tasks. *Journal of Biomechanics.* 61, 263-268.

[Hespanhol Junior et al.; 2016] Hespanhol Junior, LC. van Mechelen, W. Postuma, E. Verhagen, E. (2016). Health and economic burden of running-related injuries in runners training for an event: a prospective cohort study. *Scandinavian Journal of Medicine & Science in Sports.* 26, 1091-1099.

[Hreljac; 2005] Hreljac, A. (2005). Etiology, prevention, and early intervention of overuse injuries in runners: a biomechanical perspective. *Physical Medicine and Rehabilitation Clinics.* 16(3), 651-667.

[Kalman; 1960] Kalman, RE. (1960). A new approach to linear filtering and prediction problems. *Transactions of the ASME. Series D, Journal of Basic Engineering.* 82(1), 35-45.

[Kerdok et al.; 2002] Kerdok, AE. Biewner, AA. McMahon, TA. Weyand, PG. Herr, HM. (2002). Energetics and mechanics of human running on surfaces of different stiffnesses. *Journal of Applied Physiology.* 92, 469-478.

[Kibler & Chandler; 1992] Kibler, WB. Chandler, TJ. Stracener, ES. (1992). Musculoskeletal adaptations and injuries due to overtraining. *Exercise and Sport Sciences Reviews.* 20, 99-126.

[Lieberman et al.; 2010] Lieberman, DE. Venkadesan, M. Werbal, WA. Daoud, AI. D'Andrea, S. Davis, IS. Mang'Eni, RO. Pitsiladis, Y. (2010). Foot strike patterns and collision forces in habitually barefoot versus shod runners. *Nature.* 463, 531-535.

[Liu & Nigg; 2000] Liu, W. Nigg, BM. (2000). A mechanical model to determine the influence of masses and mass distribution on the impact force during running. *Journal of Biomechanics.* 33, 219-224.

[Ly et al.; 2010] Ly, QH. Alaoui, A. Erlicher, S. Baly, L. (2010). Towards a footwear design tool: influence of shoe midsole properties and ground stiffness on the impact force during running. *Journal of Biomechanics.* 43, 310-317.

[Macera et al.; 1989] Macera, CA. Pate, RR. Powell, KE. Jackson, KL. Kendrick, JS. Craven, TE. (1989). Predicting lower-extremity injuries among habitual runners. *Archives of Internal Medicine.* 149(11): 2565-2568.

[Matijevich et al.; 2019] Matijevich, ES. Branscombe, LM. Scott, LR. Zelik, KE. (2019). Ground reaction force metrics are not strongly correlated with tibial bone load when running across speeds and slopes: implications for science, sport and wearable tech. *PLoS ONE.* 14(1): p.e.0210000.

[Mizrahi & Susak; 1982] Mizrahi, J. Susak, Z. (1982). In-vivo elastic and damping response of the human leg to impact forces. *Journal of Biomechanical Engineering.* 104(1), 63-66.

[Mizrahi et al.; 2000] Mizrahi, J. Verbitsky, O. Isakov, E. Daily, D. (2000). Effect of fatigue on leg kinematics and impact acceleration in long distance running. *Human Movement Science.* 19, 139-151.

[Morin et al.; 2011] Morin, JB. Samozino, P. Millet, G. (2011). Changes in running kinematics, kinetics, and spring-mass behavior over a 24-h run. *Medicine & Science in Sports & Exercise.* 43(5), 829-836.

[Neugebauer et al.; 2014] Neugebauer, JM. Collins, KH. Hawkins, DA. (2014). Ground reaction force estimates from actigraph GT3X+ hip accelerations. *PLoS ONE.* 9, e99023.

[Nevzat Ozguven & Berme; 1988] Nevzat Ozguven, H. Berme, N. (1988). An experimental and analytical study of impact forces during human jumping. *Journal of Biomechanics.* 21(12), 1061-1066.

[Nigg & Liu; 1999] Nigg, BM. Liu, W. (1999). The effect of muscle stiffness and damping on simulated impact force peaks during running. *Journal of Biomechanics.* 32, 849-856.

[Nigg; 2010] Nigg, BM. (2010). *Biomechanics of Sport Shoes.* Topline Printing Inc., Calgary, AB.

[Nikooyan & Zadpoor; 2011] Nikooyan, AA. Zadpoor, AA. (2011). Mass-spring-damper modelling of the human body to study running and hopping - an overview. *Proceedings of the Institution of Mechanical Engineers Part H Journal of Engineering in Medicine.* 225(12), 1121-1135.

[Ohtaki et al.; 2001] Ohtaki, Y. Sagawa, K. Inooka, H. (2001). A method for gait analysis in a daily living environment by body-mounted instruments. *JSME International Journal Series C.* 44, 1125-1132.

[Palanisamy et al.; 2015] Palanisamy, R. Cho, S. Kim, H. Sim, SH. (2015). Experimental validation of Kalman filter-based strain estimation in structures subjected to non-zero mean input. *Smart Structures and Systems.* 15(2), 489-503.

[Raper et al.; 2018] Raper, DP. Witchalls, J. Philips, EJ. Knight, E. Drew, MK. Waddington, G. (2018). Use of a tibial accelerometer to measure ground reaction force in running: a reliability and validity comparison with force plates. *Journal of Science and Medicine in Sport.* 21(1), 84-88.

[Shahabpoor & Pavic; 2018] Shahabpoor, E. Pavic, A. (2018). Estimation of vertical walking ground reaction force in real-life environments using single IMU sensor. *Journal of Biomechanics.* 79, 181-190.

[Shippen & May; 2012] Shippen, J. May, B. (2012). A kinematic approach to calculating ground reaction forces in dance. *Journal of Dance Medicine Science.* 16, 39-43.

[Simon; 2006] Simon, D. (2006). *Optimal State Estimation.* John Wiley and Sons, New York, NY.

[Sinclair et al.; 2013] Sinclair, J. Richards, J. Taylor, PJ. Edmundson, CJ. Brooks, D. Hobbs, SJ. (2013). Three-dimensional kinematic comparison of treadmill and overground running. *Sports Biomechanics.* 12(3), 272-282.

[Stanish; 1984] Stanish, WD. (1984). Overuse injuries in athletes: a perspective. *Medicine & Science in Sports & Exercise.* 16(1), 1-7.

[Troiano et al.; 2014] Troiano, RP. McClain, JJ. Brychta, RJ. Chen, KY. (2014). Evolution of accelerometer methods for physical activity research. *British Journal of Sports Medicine.* 48(13), 1019-1023.

[Waller & Schmidt; 1990] Waller ,H. Schmidt, R. (1990). The application of state observers in structural dynamics. *Mechanical Systems and Signal Processing.* 4(3), 195-213.

[Winter; 2005] Winter, DA. (2005). *Biomechanics and motor control of human movement.* John Wiley & Sons, Hoboken, NJ.

[Wouda et al.; 2017] Wouda, FJ. Giuberti, M. Bellusci, G. Maartens, E. Reenalda, J. van Beijnum, BJF. Veltink, PH. (2017). Estimation of vertical ground reaction forces and sagittal knee kinematics during running using three inertial sensors. *Frontiers in Physiology.* 9, 1-14

[Wundersitz et al.; 2013] Wundersitz, DWT. Netto, KJ. Aisbett, B. Gastin, PB. (2013). Validity of an upper-body-mounted accelerometer to measure peak vertical and resultant force during running and change-of-direction tasks. *Sports Biomechanics.* 12, 403-412.

Chapter 6

Conclusions and future work

In this dissertation the application and development of a fatigue monitoring framework for structural and biomechanical systems was presented. Simulated and experimental results were used to validate the proposed framework to assess the state of fatigue damage in near-real time for various engineered systems.

The main contributions and conclusions of this work are:

1. Uncertainty quantification and propagation for fatigue monitoring indices derived from state estimates of structural systems were presented in chapters 3 and 4. The uncertainty formulae are presented in section 2.2.3 which are derived from the estimated stresses determined by the state estimation process and the empirical fatigue material properties, i.e. model error and uncertainty in the S-N curve parameters. The results were used to monitor the remaining useful life of structural systems subject to non-Gaussian excitation for near-real time fatigue damage estimation. It was shown that for some systems, like those studied in this dissertation, the proposed framework can help to determine an optimal stopping criteria based on an allowable probability of failure. Results

were presented for both simulation and real-world applications.

2. For certain systems a fatigue monitoring framework is desirable over the traditional vibration-based damage detection methods. Often for statically determinant structures small changes in the physical properties (mass, damping, and stiffness) won't cause measurable changes in the dynamic properties of the system until the remaining useful life is small and could potentially have macroscopic crack growth. A desirable approach is to use state estimation via the Kalman filter, Unscented Kalman filter, or Model-Based Observer to monitor the accumulation of stress cycles experienced by the structure in order to estimate fatigue life. This dissertation provides the first experimental validation that fatigue monitoring could provide higher levels of reliability, larger lead times and reduced risk of catastrophic failure compared to the traditional methods when monitoring a structure throughout it's entire lifetime.

3. The framework is then applied to biomechanical systems where model parameters are uncertain/stochastic and input excitation is highly frequency dependent/unknown. The human body is very complex with many masses interacting yet MSD models have been shown to provide a good estimate of vGRF. However, traditionally parameters were tuned using forward dynamics simulation for each individual and across testing procedures. Chapter 5 proposed a state-input-parameter estimation algorithm to be applied to the vGRF estimation problem that had previously been used for structural systems in simulation. The model-data fusion approach automatically personalized to the user in order to estimate the effects of mechanical fatigue for running in non-laboratory running conditions with minimal instrumentation. It was shown that the SDOF

MSD model provided a good estimate of several vGRF waveform metrics yet had poor performance estimating the loading rate.

4. The fatigue monitoring framework can be applied to systems that can be modelled as a MSD system with representative equations of motion, minimal instrumentation to measure system response, and an empirical S-N curves with known mean and variance.

Some aspects that require further investigation are:

- *Fatigue damage can cause measurable changes in dynamic properties throughout the structures serviceable life.* In chapter 4 fatigue damage was monitored in near-real time using a Kalman filter to estimate the state with a constant MSD model. This resulted in increased model error after crack coalescence due to reduced stiffness at fatigue critical locations for a statically determinant structure. Therefore an unscented Kalman filter or extended Kalman filter could be applied to estimate uncertain model parameters and the state in order to determine if the increased computational cost is worth the increased fatigue damage accuracy. For more complex structures the extended Kalman filter or unscented Kalman filter could reduce error due to non-linearity.

- *Apply catastrophe theory to vibration-based damage detection methods.* Catastrophe theory states that sudden changes in behavior or bifurcations arise from small changes in the systems state. In chapter 4 fatigue accumulation experimentally followed a linear rule (Palmgren-Miner) where a stopping criteria was derived based on an allowable probability of failure that provided ample time before macroscopic failure occurred. However, when interrogating changes in

153

vibration characteristics such as natural frequency or mode shapes the remaining useful life had already been significantly reduced. The fatigue monitoring process seems to follow a stable manifold while damage detection methods follow an unstable manifold. Catastrophe theory could provide novel insight into the structural health monitoring framework.

- *Implement a high fidelity running model for running and walking.* In chapter 5 the simplest MSD model (SDOF) was used to determine the feasibility of estimating vGRF while running using a sacrum accelerometer. Research had previously shown that SDOF MSD models are not able to capture the impact peak while running which was experimentally validated in chapter 5; however, a two mass model can capture the dynamics. A multi-body model could provide a better estimate of important vGRF waveform properties and the ability to estimate various unknown model parameters in near-real time. This could provide a novel wearable technology to mitigate risk of injury while maximizing performance. Statistical modeling or optimization algorithms could provide insight into how to determine the input parameters necessary for state estimation processes.

- *Combine structural models with the proposed running model to provide a better fatigue monitoring framework for estimating remaining life of pedestrian bridges.* By monitoring pedestrians walking/running across the bridge and measuring the response of the bridge there is increased knowledge of the input excitation on the structure. This could provide a novel method to update bridge structural models in near-real time to determine the structural health at any time. This combined model could help with design decisions.

REFERENCES

[Abdul Razak et al.; 2012] Abdul Razak, AH. Zayegh, A. Begg, RK. Wahab, Y. (2012). Foot plantar pressure measurement system: a review. *Sensors.* 12, 9884-9912.

[Albert; 1837] Albert, WAJ. (1837). Uber Treibseile am Harz. Archiv fur Mineralogie, Georgnosie *Bergbau und Huttenkunde.* 10:215-234.

[Alton et al.; 1998] Alton, F. Baldey, L. Caplan, S. Morrissey, MC. (1998). A kinematic comparison of overground treadmill walking. *Clinical Biomechanics.* 13(6), 434-440.

[Azam et al.; 2015] Azam, SE. Chatzi, EN. Papadimitriou, C. (2015). A dual kalman filter approach for state estimation via output-only acceleration measurements. *Mechanical Systems and Signal Processing.* 60(61), 866-886.

[Azim; 2013] Azim, R. (2013). An analytical investigation on bolt tension of a flanged steel pipe joint subjected to bending moments. *International Journal of Engineering and Applied Sciences.* 2(3):71-81.

[Basquin; 1910] Basquin, OH. (1910). The exponential law of endurance tests. *Proc. Annual Meeting, American Society for Testing Materials.* 10:625-630.

[Baqersad et al.; 2015] Baqersad, J. Niezrecki, C. Avitabile, P. (2015). Extracting full-field dynamic strain on a wind turbine rotor subjected to arbitrary excitations using 3d point tracking and a modal expansion technique. *Sound and Vibration.* 352:16-29.

[Benedetti et al.; 2013] Benedetti, M. Fontanari, V. Battisti, L. (2013). Structural health monitoring of wind towers: residual fatigue life estimation. *Smart Materials and Structures.* 22(4): 045017

[Bently & Hatch; 2002] Bently, DE. Hatch, CT. (2002). *Fundamentals of rotating machinery diagnostics.* ASME Press: New York,NY.

[Blanco; 2009] Blanco, MI. (2009). The economics of wind energy. *Renewable and Sustainable Energy Reviews.* 13(6):1372-1382.

[Blickhan; 1989] Blickhan, R. (1989). The spring-mass model for running and hopping. *Journal of Biomechanics.* 22(11/12), 1217-1227.

[Bobbert et al.; 1991] Bobbert, MF. Schamhardt, HC. Nigg, BM. (1991). Calculation of vertical ground reaction force estimates during running from positional data. *Journal of Biomechanics.* 24, 1095-1105.

[Bocian et al.; 2006] Bocian, M. Brownjohn, JMW. Racic, V. Hester, D. Quattrone, A. Monnickendam, R. (2006). A framework for experimental determination of localized vertical pedestrian forces on full-scale structures using wireless attitude and heading reference systems. *Journal of Sound and Vibration.* 376, 217-243.

[Braithwaite; 1854] Braithwaite, F. (1854). On the fatigue and consequent fractures of metals. *Institution of Civil Engineers, Minutes of Proceedings.* Vol. XIII:463-474.

[Burr et al.; 1985] Burr, DB. Martin, RB. Schaffler, MB. Radin, EL. (1985). Bone remodeling in response to in-vivo fatigue microdamage. *Journal of Biomechanics.* 18(3), 189-200.

[Cavanagh; 1987] Cavanagh, PR. (1987). The biomechanics of lower extremity action in distance running. *Foot & Ankle.* 7, 197-217.

[Ciang et al.; 2008] Ciang, CC. Lee, JR. Bang, HJ. (2008). Structural health monitoring for a wind turbine system: a review of damage detection methods. *Measurement Science and Technology.* 19(12): 122001.

[Chamay & Tschantz; 1972] Chamay, A. Tschantz, P. (1972). Mechanical influences in bone remodeling: experimental research on Wolff's law. *Journal of Biomechanics.* 5(2), 173-180.

[Charry et al.; 2013] Charry, E. Hu, W. Umer, M. Ronchi, A. Taylor, S. (2013). Study on estimation of peak ground reaction forces using tibial accelerations in running. *IEEE Eighth International Conference on Intelligent Sensors, Sensor Networks and Information Processing.* (Melbourne, VIC), 288-293.

[Chen & Xu; 2016] Chen, X. Xu, JZ. (2016). Structural failure analysis of wind turbines impacted by super typhoon Usagi. *Engineering Failure Analysis*. 60:391-404.

[Chi & Schmitt; 2005] Chi, KJ. Schmitt, D. (2005). Mechanical energy and effective foot mass during impact loading of walking and running. *Journal of Biomechanics*. 38, 1387-1395.

[Chou & Tu; 2011] Chou, JS. Tu, W. (2011). Failure analysis and risk management of a collapsed large wind turbine tower. *Engineering Failure Analysis*. 18(1):295-313

[Clark et al.; 2014] Clark, KP. Ryan, LJ. Weyand, PJ. (2014). Foot speed, foot-strike and footwear: linking gate mechanics and running ground reaction forces. *Journal of Experimental Biology*. 217, 2037-2040.

[Clark et al.; 2017] Clark, KP. Ryan, LJ. Weyand, PG. (2017). A general relationship links gait mechanics and running ground reaction forces. *Journal of Experimental Biology*. 220, 247-258.

[Coffin; 1954] Coffin, LF. (1954). A study of the effects of cyclic thermal stresses on a ductile metal. *Transactions of the American Society of Mechanical Engineers*. 76:931-950.

[Craig & Bampton; 1968] Craig, RR. Bampton, MCC. (1968). Coupling of Substructures for Dynamic Analyses. *AIAA Journal*. 6(7):1313-1319.

[Cui; 2002] Cui, W. (2002). A state-of-the-art review on fatigue life prediction methods for metal structures *Journal of Marine Science and Technology*. 7(1):43-56.

[CWIF; 2016] CWIF. (2016). Accident statistics. URL http://www.caithnesswindfarms.co.uk/

[Derrick et al.; 2000] Derrick, TR. Caldwell, GE. Hamill, J. (2000). Modeling the stiffness characteristics of the human body while running with various stride lengths. *Journal of Applied Biomechanics*. 16(1), 36-51.

[Derrick; 2004] Derrick, TR. (2004). The effects of knee contact angle on impact forces and accelerations. *Medical & Science in Sports & Exercise*. 36, 832-837.

[Dertimanis et al.; 2019] Dertimanis, VK. Chatzi, EN. Azam, SE. Papadimitriou, C. (2019). Input-state-parameter estimation of structural systems from limited output information. *Mechanical Systems and Signal Processing*. 126, 711-746.

[Doebling et al.; 1996] Doebling, SW. Farrar, CR. Prime, MB. Shevitz, DW. (1996).*Damage identification and health monitoring of structural and mechanical systems from changes in their vibration characteristics: a literature review.* Los Alamos National Laboratory Report LA-13070-MS.

[Doebling et al.; 1998] Doebling, S. Farrar, C. Prime, MB. (1998). A summary review of vibration-based damage identification methods. *Shock and Vibration Digest.* 30(2):91-105.

[Downing; 2012] Downing, NE. (2012). *Mechanical behavior of materials: engineering methods for deformation, fracture, and fatigue.* 4th ed. Pearson: Boston, MA.

[Dye; 2005] Dye, SF. (2005). The pathophysiology of patellofemoral pain: a tissue homeostasis perspective. *Clinical Orthopaedics and Related Research.* 436, 100-110.

[Edwards; 2018] Edwards, WB. (2018). Modeling overuse injuries in sport as a mechanical fatigue phenomenon. *Exercise and Sport Sciences Reviews.* 46(4), 224-231.

[Erazo & Hernandez; 2014] Erazo, K. Hernandez, EM. (2014). A model-based observer for state and stress estimation in structural and mechanical systems: Experimental validation. *Mechanical Systems and Signal Processing.* 43(1):141-152.

[Farrar et al.; 2001] Farrar, C. Doebling, S. Nix, D. (2001). Vibration-based structural damage identification. *Philosophical Transaction of the Royal Society.* 359:131-149.

[Farrar & Lieven; 2002] Farrar, CR. Lieven, NAJ. (2002). Damage prognosis: the future of structural health monitoring. *Phil. Trans. R. Soc. A.* 365:623-632.

[Farrar & Worden; 2007] Farrar, CR. Worden, K. (2007). An introduction to structural health monitoring. *Philos Trans A Math Phys Eng Sci.* 365(1851):303-315.

[Fujiyam et al.; 2014] Fujiyama, C. Yonetsu, K. Maeshima, T. Koda, Y. (2014). Identifiable stress state of wind turbine tower-foundation system based on field measurement and fe analysis. *Procedia Engineering.* 95:279-289.

[Gagg & Lewis; 2009] Gagg, CR. Lewis, PR. (2009). In-service fatigue failure of engineered products and structures - case study review. *Engineering Failure Analysis.* 16(6):1775-1793.

[Gelb; 1987] Gelb, A. (1987). *Applied Optimal Estimation.* MIT Press, Cambridge, MA.

[Gelb; 1996] Gelb, A. (1996). *Applied Optimal Estimation..* 14 MIT Press: Cambridge, MA.

[Giagopoulos et al.; 2019] Giagopoulos, D. Arailopoulos, A. Dertimanis, V. Papadimitriou, C. Chatzi, E. Grompanopoulos K. (2019). Structural health monitoring and fatigue damage estimation using vibration measurements and finite element model updating. *Structural Health Monitoring* . 18(4):1189-1206.

[Gobbato et al.; 2012] Gobbato, M. Conte, JP. Kosmatka, JB. Farrar CR.(2012). A reliability-based framework for fatigue damage prognosis of composite aircraft structures. *Probabilistic Engineering Mechanics.* 29:176-188.

[Gobbato et al.; 2014] Gobbato, M. Kosmatka, JB. Conte JP. (2014). A recursive bayesian approach for fatigue damage prognosis: An experimental validation at the reliability component level. *Mechanical Systems and Signal Processing.* 45(2):448-467.

[Guo et al.; 2017] Guo, Y. Storm, F. Zhao, Y. Billings, S. Pavic, A. Mazza, C. Guo, LZ. (2017). A new proxy measurement algorithm with application to the estimation of vertical ground reaction forces using wearable sensors. *Sensors.* 17, e2181

[Gurchiek et al.; 2017] Gurchiek, RD. McGinnis, RS. Needle, AR. McBride, JM. van Werkhoven, H. (2017). The use of a single inertial sensor to estimate 3-dimensional ground reaction force during accelerative running tasks. *Journal of Biomechanics.* 61, 263-268.

[Guyan; 1965] Guyan, R. (1965). Reduction of stiffness and mass matrices. *AIAA Journal.* 3:380

[Hammerum et al.; 2007] Hammerum, K. Brath, P. Poulsen, NK. (2007). A fatigue approach to wind turbine control. *Journal of Physics:Conference Series.* 75(1): 012081.

[Hao; 2010] Hao, S. (2010). I-35W bridge collapse. *Journal of Bridge Engineering.* 15(5):608-614.

[Hernandez; 2011] Hernandez, EM. (2011). A natural observer for optimal state estimation in second order linear structural systems. *Mechanical Systems and Signal Processing.* 25(8):2938-2947.

[Hernandez; 2013] Hernandez, EM. (2013). Optimal model-based state estimation in mechanical and structural systems. *Structural Control and Health Monitoring.* 20(4):532-543.

[Hernandez et al.; 2013] Hernandez, EM. Bernal, D. Caracoglia, L. (2013). On-line monitoring of wind-induced stresses and fatigue damage in instrumented structures. *Structural Control and Health Monitoring.* 20(10);1291-1302.

[Hespanhol Junior et al.; 2016] Hespanhol Junior, LC. van Mechelen, W. Postuma, E. Verhagen, E. (2016). Health and economic burden of running-related injuries in runners training for an event: a prospective cohort study. *Scandinavian Journal of Medicine & Science in Sports.* 26, 1091-1099.

[Hreljac; 2005] Hreljac, A. (2005). Etiology, prevention, and early intervention of overuse injuries in runners: a biomechanical perspective. *Physical Medicine and Rehabilitation Clinics.* 16(3), 651-667.

[Iliopoulos et al.; 2014] Ilopoulos, A. Devriendt, C. Guillaume, P. Van Hemelrijck, D. (2014). Continuous Fatigue Assessment of an Offshore Wind Turbine Using a Limited Number of Vibration Sensors. *EWSHM - 7th European Workshop on Structural Health Monitoring.*

[Iliopoulos et al.; 2015] Iliopoulos, AN. Weijtjens, W. Hemelrijck, DV. Devriendt, C. (2015). Prediction of dynamic strains on a monopile offshore wind turbine using virtual sensors. *Journal of Physics: Conference Series.* 628(1):012108.

[Iliopoulos et al.; 2016] Iliopoulos, A. Shirzadeh, R. Weijtjens, W. Guillaume, P. Hemelrijck, DV. Devriendt, C. (2016). A modal decompositionand expansion approach for prediction of dynamic responses on a monopile offshore wind turbine using a limited number of vibration sensors. *Mechanical Systems and Signal Processing.* 68-69:84-104.

[Inaudi & Deblois; 2009] Inaudi, D. Deblois, R. (2009). Overview of 40 bridge structural health monitoring projects. *26th International Bridge Conference.* Pennsylvania, PA.

[Inglis; 1927] Inglis, NP. (1927). Hysteresis and fatigue of Wohler rotating cantilever specimen. *The Metallurgist.* 23-27.

[Inman et al.; 2005] Inman, D. Farrar, C. Lopes, V. (2005). *Damage Prognosis: For Aerospace, Civil and Mechanical Systems.* New York: Wiley.

[Jazwinski; 1970] Jazwinski, AH. (1970). *Stochastic Processes and Filtering Theory.* Academic Press: New York, NY.

[Jonkman & Buhl; 2005] Jonkman, B. Buhl, M. (2005). Turbsim user's guide. http://wind.nrel.gov/designcodes/preprocessors/turbsim/turbsim.pdf. National Renewable Energy Laboratory. Golden, CO, USA.

[Jonkman & Buhl; 2005b] Jonkman, J. Buhl, M. (2005). Fast user's guide. NREL/EL-500-38230 (previously NREL/EL-500-29798). National Renewable Energy Laboratory. Golden, CO, USA.

[Jonkman et al.; 2009] Jonkman, J. Butterfield, S. Musial, W. Scott, G. (2009). Definition of a 5-mw reference wind turbine for offshore system development. NREL/TP-500-38060. National Renewable Energy Laboratory. Golden, CO, USA

[Julier & Uhlmann; 1997] Julier, SJ. Uhlmann, JK. (1997). A new extension of the kalman filter to nonlinear systems. *Proc. of AeroSense: The 11th Int. Symp. on Aerospace/Defense Sensing, Simulation and Controls.*

[Juvinall & Marshek; 2012] Juvinall, R.C. Marshek, KM. (2012). *Fundamentals of Machine Component Design.* 5th ed. Wiley: Hoboken, NJ.

[Kachanov; 1958] Kachanov, LM. (1958). In time to rupture in creep conditions. *Izviestia Akademii Nauk SSSR, Otdelenie Tekhnicheskikh Nauk* . 8:26-31.

[Kachanov; 1986] Kachanov, LM. (1986). *Introduction to continuum damage mechanics. Mechanics of Elastic Stability.* Netherlands: Springer.

[Kalman; 1960] Kalman, RE. (1960). A new approach to linear filtering and prediction problems. *Transactions of the ASME. Series D, Journal of Basic Engineering.* 82(1), 35-45.

[Kerdok et al.; 2002] Kerdok, AE. Biewner, AA. McMahon, TA. Weyand, PG. Herr, HM. (2002). Energetics and mechanics of human running on surfaces of different stiffnesses. *Journal of Applied Physiology.* 92, 469-478.

[Kibler & Chandler; 1992] Kibler, WB. Chandler, TJ. Stracener, ES. (1992). Musculoskeletal adaptations and injuries due to overtraining. *Exercise and Sport Sciences Reviews.* 20, 99-126.

[Lieberman et al.; 2010] Lieberman, DE. Venkadesan, M. Werbal, WA. Daoud, AI. D'Andrea, S. Davis, IS. Mang'Eni, RO. Pitsiladis, Y. (2010). Foot strike patterns and collision forces in habitually barefoot versus shod runners. *Nature.* 463, 531-535.

[Liu & Nigg; 2000] Liu, W. Nigg, BM. (2000). A mechanical model to determine the influence of masses and mass distribution on the impact force during running. *Journal of Biomechanics.* 33, 219-224.

[Ly et al.; 2010] Ly, QH. Alaoui, A. Erlicher, S. Baly, L. (2010). Towards a footwear design tool: influence of shoe midsole properties and ground stiffness on the impact force during running. *Journal of Biomechanics.* 43, 310-317.

[Macera et al.; 1989] Macera, CA. Pate, RR. Powell, KE. Jackson, KL. Kendrick, JS. Craven, TE. (1989). Predicting lower-extremity injuries among habitual runners. *Archives of Internal Medicine.* 149(11): 2565-2568.

[Manson; 1954] Manson, SS. (1954). Behavior of materials under conditions of thermal stress. *Technical Report, National Advisory Commission on Aeronautics: report 1170.* Cleveland: Lewis Flight Propulsion Laboratory.

[Matijevich et al.; 2019] Matijevich, ES. Branscombe, LM. Scott, LR. Zelik, KE. (2019). Ground reaction force metrics are not strongly correlated with tibial bone load when running across speeds and slopes: implications for science, sport and wearable tech. *PLoS ONE.* 14(1): p.e.0210000.

[Matsuishi; 1968] Matsuishi, M. Endo, T. (1968). Fatigue of metals subjected to varying stress. *Journal of Basic Engineering.*

[Miner; 1945] Miner, MA. (1945). Cumulative damage in fatigue. *Trans. ASME J. appl. Mech,.* 59:A160-A162.

[Mizrahi & Susak; 1982] Mizrahi, J. Susak, Z. (1982). In-vivo elastic and damping response of the human leg to impact forces. *Journal of Biomechanical Engineering.* 104(1), 63-66.

[Mizrahi et al.; 2000] Mizrahi, J. Verbitsky, O. Isakov, E. Daily, D. (2000). Effect of fatigue on leg kinematics and impact acceleration in long distance running. *Human Movement Science.* 19, 139-151.

[Montgomery; 1997] Montgomery, DC. (1997). *Introduction to statistical quality control.* John Wiley & Sons Inc: New York, NY.

[Morin; 1853] Morin, A. (1853). Lecons de mecanique practique-resistance des materiaux. *Paris, Librairie de L. Hachette et Cie.* p.456.

[Morin et al.; 2011] Morin, JB. Samozino, P. Millet, G. (2011). Changes in running kinematics, kinetics, and spring-mass behavior over a 24-h run. *Medicine & Science in Sports & Exercise.* 43(5), 829-836.

[Neugebauer et al.; 2014] Neugebauer, JM. Collins, KH. Hawkins, DA. (2014). Ground reaction force estimates from actigraph GT3X+ hip accelerations. *PLoS ONE.* 9, e99023.

[Nevzat Ozguven & Berme; 1988] Nevzat Ozguven, H. Berme, N. (1988). An experimental and analytical study of impact forces during human jumping. *Journal of Biomechanics.* 21(12), 1061-1066.

[Nigg & Liu; 1999] Nigg, BM. Liu, W. (1999). The effect of muscle stiffness and damping on simulated impact force peaks during running. *Journal of Biomechanics.* 32, 849-856.

[Nigg; 2010] Nigg, BM. (2010). *Biomechanics of Sport Shoes.* Topline Printing Inc., Calgary, AB.

[Nikooyan & Zadpoor; 2011] Nikooyan, AA. Zadpoor, AA. (2011). Mass-spring-damper modelling of the human body to study running and hopping - an overview. *Proceedings of the Institution of Mechanical Engineers Part H Journal of Engineering in Medicine.* 225(12), 1121-1135.

[Noppe et al.; 2016] Noppe, N. Iliopoulos, A. Weijtjens, W. Devriendt, C. (2016). Full load estimation of an offshore wind turbine based on scada and accelerometer data. *J. Phys.: Conf. Ser.* 753:072025.

[NTSB; 2007] National Transportation Safety Board. (2007). Collapse of I-35W Highway Bridge Minneapolis, Minnesota. *Accident Report.* NTSB/HAR-08/03:PB2008-916203.

[Ohtaki et al.; 2001] Ohtaki, Y. Sagawa, K. Inooka, H. (2001). A method for gait analysis in a daily living environment by body-mounted instruments. *JSME International Journal Series C.* 44, 1125-1132.

[Ottosen et al.; 2008] Ottosen, NS. Stenstrom, R. Ristinmaa, M. (2008). Continuum approach to high-cycle fatigue modeling. *International Journal of Fatigue.* 30(6):996-1006.

[Pacheco et al.; 2017] Pacheco, J. Oliveira, G. Magalhaes, F. Cunha, A. Caetano, E. (2017). Wind turbine vibration based shm system: influence of the sensors layout and noise. *Procedia Engineering.* 2017;199:2160-2165. x International Conference on Structural Dynamics, EURODYN.

[Palanisamy et al.; 2015] Palanisamy, R. Cho, S. Kim, H. Sim, SH. (2015). Experimental validation of Kalman filter-based strain estimation in structures subjected to non-zero mean input. *Smart Structures and Systems.* 15(2), 489-503.

[Palmgren; 1924] Palmgren, A. (1924). Die Lebensdauer von Kugellagern. *VDI-Zeitschrift.* 68:339-341.

[Papadimitriou et al.; 2011] Papadimitriou, C. Fritzen, CP. Kraemer, P. Ntotsios, E. (2011). Fatigue predictions in entire body of metallic structures from a limited number of vibration sensors using kalman filtering. *Structural Control and Health Monitoring.* 18(5):554-573.

[Pook; 2007] Pook, LP. (2007). *Metal Fatigue: What It Is, Why It Matters. Solid Mechanics and Its Applications.* Netherlands: Springer.

[Rankine; 1842] Rankine, WJM. (1842). On the causes of the unexpected breakage of the journals of railway axles, and on the means of preventing such accidents by observing the law of continuity in their construction. *Institution of Civil Engineers, Minutes of Proceedings.* 2:105-108.

[Raper et al.; 2018] Raper, DP. Witchalls, J. Philips, EJ. Knight, E. Drew, MK. Waddington, G. (2018). Use of a tibial accelerometer to measure ground reaction force in running: a reliability and validity comparison with force plates. *Journal of Science and Medicine in Sport.* 21(1), 84-88.

[Ribeiro; 2004] Ribeiro, MI. (2004) Kalman and extended Kalman filters: concept, derivation and properties. *Technical report.* Institute for Systems and Robotics.

[Schaumann & Eichstadt; 2015] Schaumann, P. Eichstadt, R. (2015). Fatigue assessment of high-strength bolts with very large diameters in substructures for offshore wind turbines. *Proceedings of the twenty-fifth International Ocean and Polar Engineering Conference,ISOPE.*

[Schijve; 2003] Schijve, J. (2003). Fatigue of structures and materials in the 20th century and the state of the art. *International Journal of Fatigue.* 25(8):679-702.

[Schijve; 2005] Schijve, J. (2005). Statistical distribution functions and fatigue of structures. *International Journal of Fatigue.* 27:1031-1039.

[Schijve; 2008] Schijve, J. (2008). *Fatigue of Structures and Materials.* Netherlands: Springer.

[Schijve; 2009] Schijve, J. (2009). Fatigue under variable-amplitude loading. *Fatigue of Structures and Materials.* 295-328. Netherlands: Springer.

[Schull; 2002] Shull, P. (2002). *Nondestructive evaluation theory, techniques, and applications.* Marcel Dekker, Inc: New York, NY.

[Schutz; 1996] Schutz, W. (1996). A history of fatigue. *Engineering Fracture Mechanics.* 54(2):263-300.

[Shahabpoor & Pavic; 2018] Shahabpoor, E. Pavic, A. (2018). Estimation of vertical walking ground reaction force in real-life environments using single IMU sensor. *Journal of Biomechanics.* 79, 181-190.

[Shen et al.; 2000] Shen, HJ. Lin, J. Mu, E. (2000). Probabilistic model on stochastic fatigue damage. *International Journal of Fatigue.* 22:569-572.

[Shippen & May; 2012] Shippen, J. May, B. (2012). A kinematic approach to calculating ground reaction forces in dance. *Journal of Dance Medicine Science.* 16, 39-43.

[Shirzadeh et al.; 2015] Shirzadeh, R. Weijtjens, W. Guillaume, P. Devriendt, C. (2015). The dynamics of an offshore wind turbine in parked conditions: a comparison between simulations and measurements. *Wind Energy.* 18(10):1685-1702.

[Simon; 2006] Simon, D. (2006). *Optimal State Estimation.* John Wiley and Sons, New York, NY.

[Sinclair et al.; 2013] Sinclair, J. Richards, J. Taylor, PJ. Edmundson, CJ. Brooks, D. Hobbs, SJ. (2013). Three-dimensional kinematic comparison of treadmill and overground running. *Sports Biomechanics.* 12(3), 272-282.

[Sobczyk & Spencer; 1991] Sobczyk, K. Spencer, BF. (1991). *Random Fatigue: From Data to Theory.* Academic Press, New York.

[Sobczyk; 1992] Sobczyk, K. Spencer, BF. (1992). *Random Fatigue: From Data to Theory.* Academic Press.

[Sohn et al.; 2003] Sohn, H. Farrar, CR. Hemez, FM. Czarnecki, JJ. Shunk, DD. Stinemates, DW. Nadler, BR. (2003). *A review of structural health monitoring literature: 1996-2001.* Los Alamos National Laboratory Report LA-13976-MS.

[Soman et al.; 2016] Soman, R. Malinowski, P. Ostachowicz, W. (2016). Bi-axial neutral axis tracking for damage detection in wind-turbine towers. *Wind Energy.* 19:639-650.

[Stanish; 1984] Stanish, WD. (1984). Overuse injuries in athletes: a perspective. *Medicine & Science in Sports & Exercise.* 16(1), 1-7.

[Stephens et al.; 2000] Stephens, RI. Fatemi, A. Stephens, RR. Fuchs, HO. (2000). *Metal Fatigue in Engineering.* New York: Wiley, 2.

[Suresh; 2001] Suresh, S. (2001). *Fatigue of materials.* Cambridge: Cambridge University Press.

[Tafheem & Amanat; 2015] Tafheem, Z. Amanat, K. (2015). Finite element investigation on the behavior of bolted flanged steel pipe joint subject to bending. *Journal of Civil Engineering.* 43(1): 79-91.

[Tatsis et al.; 2017] Tatsis, K. Dertimanis, V. Abdallah, I. Chatzi, E. (2017). A substructure approach for fatigue assessment on wind turbine support structures using output-only measurements. *Procedia Engineering.* x International Conference on Structural Dynamics, EURODYN. 199:1044-1049.

[Tewolde et al.; 2017] Tewolde, S. Hoffer, R. Haardt, H. (2017). Validated model based development of damage index for structural health monitoring of offshore wind turbine support structures. *Procedia Engineering.* x International Conference on Structural Dynamics, EURODYN. 199:3242-3247.

[Tibaldi et al.; 2016] Tibaldi, C. Henriksen, L. Hansen, M. Bak, C. (2016). Wind turbine fatigue damage evaluation based on a linear model and a spectral method. *Wind Energy.* 19: 1289-1306.

[Troiano et al.; 2014] Troiano, RP. McClain, JJ. Brychta, RJ. Chen, KY. (2014). Evolution of accelerometer methods for physical activity research. *British Journal of Sports Medicine.* 48(13), 1019-1023.

[USDOH; 2010] U.S. Department of Homeland Security, S. and Technology. (2010). Aging infrastructure: Issues, research, and technology. *Building and Infrastructure Protection Series.*

[van der Valk & Voormeeren; 2012] van der Valk, P. Voormeeren, S. (2012). An overview of modeling approaches for complex offshore wind turbine support structures. *Proceedings of ISMA*. 4437-4452.

[van Gent et al.; 2007] van Gent, RN. Siem, D. van Middelkoop, M. (2007). Incidence and determinants of lower extremity running injuries in long distance runners: a systematic review. *British Journal of Sports Medicine*. 41:469-480.

[Veers et al.; 2003] Veers, PS. Ashwill, TD. Sutherland, HJ. Laird, DL. Lobitz, DW. Griffin, DA. Mandell, JF. Musial, WD. Jackson, K. Zuteck, M. Miravete, A. Tsai, SW. Richmond, JL. (2003). Trends in the Design, Manufacture and Evaluation of Wind Turbine Blades. *Wind Energy*. 6(3):245-259

[Waller & Schmidt; 1990] Waller ,H. Schmidt, R. (1990). The application of state observers in structural dynamics. *Mechanical Systems and Signal Processing*. 4(3), 195-213.

[Wan & Van Der Merwe; 2000] Wan, EA. Van Der Merwe, R. (2000). The unscented kalman filter for nonlinear estimation. *Proc. of IEEE Symposium 2000*. Lake Louise, Oct 2000.

[Weijtjens et al.; 2016] Weijtjens, W. Verbelen, T. Sitter, GD. Devriendt, C. (2016). Foundation structural health monitoring of an offshore wind turbine a full-scale case study. *Structural Health Monitoring*. 15(4):389-402.

[Weijtjens et al.; 2017] Weijtjens, W. Verbelen, T. Capello, E. Devriendt, C. (2017). Vibration based structural health monitoring of the sub-structures of five offshore wind turbines. *Procedia Engineering*. x International Conference on Structural Dynamics, EURODYN. 199:2294-2299.

[Winter; 2005] Winter, DA. (2005). *Biomechanics and motor control of human movement*. John Wiley & Sons, Hoboken, NJ.

[Wohler; 1867] Wohler's experiments on the strength of metals. (1867). *Engineering*. 4:160-161.

[Wouda et al.; 2017] Wouda, FJ. Giuberti, M. Bellusci, G. Maartens, E. Reenalda, J. van Beijnum, BJF. Veltink, PH. (2017). Estimation of vertical ground reaction forces and sagittal knee kinematics during running using three inertial sensors. *Frontiers in Physiology*. 9, 1-14

[Wundersitz et al.; 2013] Wundersitz, DWT. Netto, KJ. Aisbett, B. Gastin, PB. (2013). Validity of an upper-body-mounted accelerometer to measure peak

vertical and resultant force during running and change-of-direction tasks. *Sports Biomechanics.* 12, 403-412.

[Wymore et al.; 2015] Wymore, M. Dam, JV. Ceylan, H. Qiao, D. (2015). A survey of health monitoring systems for wind turbines. *Renewable and Sustainable Energy Reviews.* 52: 976-990.